SOI Through-Wafer Monolithic Knudsen Pumps for Microscale Gas Chromatography Applications

by

Tsenguun Byambadorj

A dissertation submitted in partial fulfillment
of the requirements for the degree of
Doctor of Philosophy
(Electrical and Computer Engineering)
in the University of Michigan
2022

Doctoral Committee:

Professor Yogesh B. Gianchandani, Co-Chair
Dr. Yutao Qin, Co-Chair
Professor Katsuo Kurabayashi
Professor Khalil Najafi

Tsenguun Byambadorj

tsenguun@umich.edu

ORCID iD: 0000-0001-7019-9148

Acknowledgements

First of all, I would like to acknowledge my research advisor, Professor Yogesh Gianchandani, for leading me through this journey of becoming a PhD. I am grateful for the opportunity to have joined his research group, learned from him, and worked on these projects with many talented individuals. His vast experience, knowledge, words of wisdom, thoughtfulness, and bright ideas guided me through this path. Many thanks to my co-chair Dr. Yutao Qin who mentored and collaborated with me on my research projects. His knowledge, support, and intellect helped me overcome many obstacles and complete my mission.

Next, I would like to thank my past and present committee members, Prof. Khalil Najafi, Prof. Katsuo Kurabayashi, and late Prof. Luis Bernal, for providing valuable feedback to my research. Their work on gas micropumps, plasma etching, and microscale gas chromatography have been important resource for my thesis.

I would like to thank all the members of our research group. Alex Benken mentored me at the Lurie Nanofabrication Facility when I first started my work here. Our brainstorming sessions have been very valuable to the success of my work. Qisen Cheng and I collaborated on the Gen S1 pumps. His design and modeling work have been a tremendous help for me. Xiangyu (Daniel) Zhao worked tirelessly on the monolithic gas analysis systems with me. The IARPA team, including Hsueh-Tsung (Leo) Lu, Weilin Liao, Declan Winship, Qu Xu, and Robert Gordenker, collaborated with me through the progress of my research. Yemin (Stacey) Tang helped me figure out the DRIE process. Trasa Burkhardt organized all the wonderful gatherings. I also thank all past

and present members of our office #2001 for their friendship and camaraderie during my time here at UM including Jiqing, Tal, Ali, Yi, Amin, Farzad, Andy, Ramprasad, Neeharika, Sajal, Partha, Behnoush, Ester, Irene, Tao, and Adrienne.

I also thank all the LNF engineers and staff including Sandrine Martin and Pilar Herrera-Fierro for the administration, Shawn Wright and Kevin Owen for the etch tools, Tony Sebastian and Matt Oonk for the deposition tools, and Brian Armstrong and Katharine Beach for the general tools. Their collaboration helped the progress of my microfabrication tremendously.

My MCO family in Michigan has provided me with much needed friendship, support, and teamwork. I thank them for making me feel at home in Ann Arbor.

Finally, I would like to thank my parents Byambadorj and Batkhishig, brother Bilguun, nephew Bilegt, and my partner Aza for their love, support, and comfort that made it possible for me to pursue my passion and achieve goals that I did not think were possible. I am grateful to have you in my life. Thank you.

Table of Contents

List of Figures

List of Tables

Abstract

Gas micropumps are essential components to generate gas flow and apply pressure in various microanalytical applications such as microscale gas chromatography (μGC). Knudsen pumps (KPs) are attractive for such applications because of the thermally driven, motionless operation that provides high reliability and long lifetime. In particular, silicon-on-insulator (SOI) through-wafer KP architectures are the most attractive type of KP for their high performance with the implementation of a number of well-controlled and lithographically defined pumping channels. This thesis explores two threads of SOI through-wafer KPs suitable for μGC applications. The first thread is KPs with suspended (S) membrane structures and the second thread is KPs with unsuspended (U) structure.

The Gen S1 KP, the first generation KP of this thesis with suspended membrane structures, consists of four monolithically integrated stages that are fabricated by a five-mask lithographic process. Each pumping stage is fluidically connected to adjacent stages by lateral channels etched into glass dies that are bonded above and below the SOI die. The pumping channels are densely arrayed, vertically oriented, 1.2 μm wide rectangular channels with 10 nm thick Al_2O_3 sidewalls. A suspended membrane above the pumping channels houses the metal heater and provides thermal isolation to the substrate. While operating at ambient atmospheric pressure, the Gen S1 4-stage KP provides a blocking pressure of ≈3.3 kPa and maximum air flow rate of ≈0.75 sccm with 1.2 W input power. Such performance is suitable for providing separation gas flow in μGCs.

The Gen S2 KP, the second generation KP of this thesis with suspended membrane structures, provides a major enhancement of blocking pressure performance by implementing the longest (25

μm) vertical pumping channels in through-wafer KPs to date. The pumping channel length provides extremely high thermal isolation whereas the 1.2 μm width provides flow rates suitable for μGCs. At 0.5 W applied power, the Gen S2 5-stage KP provides a maximum flow rate of 0.36 sccm and blocking pressure of 2 kPa. This performance, *i.e.,* 4 kPa/W, is 45% higher than prior record of comparable KPs.

The Gen U1 is the mechanically robust KP with an unsuspended structure. With no suspended membrane, this structure significantly improves the mechanical robustness and simplifies the microfabrication process compared to the previously reported KPs that rely on suspended membranes. The unsuspended KP fabrication process eliminates the complicated trench refill, polish, and sacrificial etch steps that were required for micromachined KPs with suspended membranes. The reported KPs incorporate multiple parallel pumping channels to scale the gas flow. At atmospheric pressure, the 4-channel KP provides a blocking pressure of 620 Pa and maximum flow rate of 0.041 sccm through 0.001 mm^2 channel area with 2 W applied power. Such a maximum flow rate per channel area is superior to that of the KPs with suspended membranes and complicated fabrication processes. The fabrication simplicity and reliability of this mechanically robust KP can enable monolithic integration onto lab-on-a-chip systems.

Owing to their suspended membrane structures that provide high thermal isolation and a large number of parallel pumping channels, the Gen S1 and S2 KPs achieve high flow rate and power efficiency. In contrast, the Gen U1 KPs provide superior mechanical robustness and simple fabrication process. Both KP architectures provide similar level of blocking pressure, achieved by the similar temperature gradient along the pumping channels.

Chapter 1:

Introduction

1.1. Knudsen Pump and Its Applications

Gas micropumps can be used to control and manipulate the media in various applications such as micro fuel cells, lab-on-a-chip, and gas phase fluidic systems [Las04, Ngu02, San02, Wil02]. One application that can greatly benefit from gas micropumps is microscale gas chromatography (μGC), in which complex analytes are typically sampled into a preconcentrator, subsequently separated by a separation column, and detected individually by a detector [Bla20, Car72, Ter79, San02, Zel04]. The working principle of the gas chromatography is illustrated in Fig. 1.1. Whereas most reported μGC systems have used conventionally machined miniature gas pumps to provide gas flow for sampling and separation [Gar15, Lia21, Zho16], some have used microfabricated gas pumps [Kim07a, Kim11, Liu11, Qin14a, Qin14b, Qin16]. In these μGC systems, the pumps are required to provide ~1 sccm flow rate at a pressure head of 1-10 kPa to drive the vapors through the system.

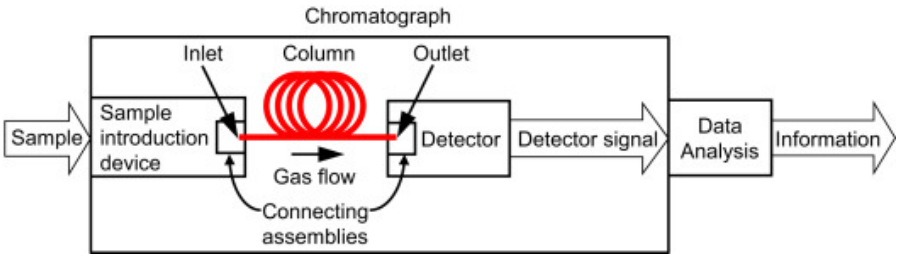

Fig. 1.1: Block diagram of a chromatographic system [Blu21].

Gas micropumps can be classified into two categories: mechanical and nonmechanical [Bes12, Ngu02, Woi05]. Mechanical micropumps typically require a mechanical actuation of a flexible diaphragm to convert electrical energy into mechanical energy [Ast07, Kim07a, Kim07b, Ste93, Xu05]. Although power efficient, mechanical gas micropumps may suffer from friction loss, stiction, and reliability issues [Au11]. Nonmechanical micropumps avoid these issues by applying electrostatic, electrokinetic, or magnetic forces on non-moving parts [Las04, Ngu02].

One popular type of micropump that has been demonstrated for μGC application is the nonmechanical Knudsen pump [Liu11, Qin14a, Qin14b, Qin16]. First demonstrated in 1909, Knudsen pumps (KPs) induce gas flow by a temperature gradient along a channel [Knu09, Knu10, Knu35]. The conditions of the gas flow depend on the mean free path of the gas molecules and the Knudsen number associated with it. The mean free path λ of gas molecules can be expressed as [Sha96]:

$$\lambda = \frac{\mu}{P}\sqrt{\frac{\pi k_B T}{2m}} \tag{1.1}$$

where μ is the shear viscosity of gas; P is the average pressure; k_B is the Boltzmann constant; T is the average temperature, and m is the molecular mass. The Knudsen number K_n can be calculated as [Fuk90]:

$$K_n = \frac{\lambda}{d} \tag{1.2}$$

where d is the hydraulic diameter of the channel. When d of a channel between two chambers is comparable to λ of the molecules, the gas flow is restricted into a free molecular (Kn>10) or transitional (10>Kn>1) regimes. With a longitudinal temperature gradient, gas molecules tend to move from the cold end to the hot end, as illustrated in (Fig. 1.2). With no moving parts, KPs offer high reliability, long lifetime, soundless operation, and precise control of gas flow [An13, An15].

In addition, KPs are powered by low DC voltage, eliminating the necessity for complex control electronics.

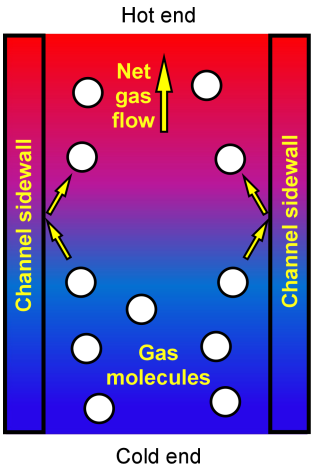

Fig. 1.2: An illustration of thermal transpiration in a narrow channel.

1.2. Motivation of This Work

Based on their pumping channels, KPs can be categorized into two groups; porous media based and lithographically microfabricated. Some KPs utilized porous media such as ceramic, mineral and polymer membrane to generate gas flow (Fig. 1.3) [Che17, Fai14, Gup08, Gup11a, Gup11b, Nak16, Pha10, You03], and have been implemented in certain μGC systems [Liu11, Qin16]. However, the porous media based KPs lack monolithic integrability due to their laborious assembly, *e.g.,* the requirement to hermetically seal the perimeter of the porous media, which is often a manual process. Their performance has been generally limited due to the defects (Fig. 1.3c) or the temperature gradient limits of the porous media.

In contrast, lithographically microfabricated KPs offer more uniform pumping channels with better controlled dimensions, and could potentially facilitate scaling for different pumping require-

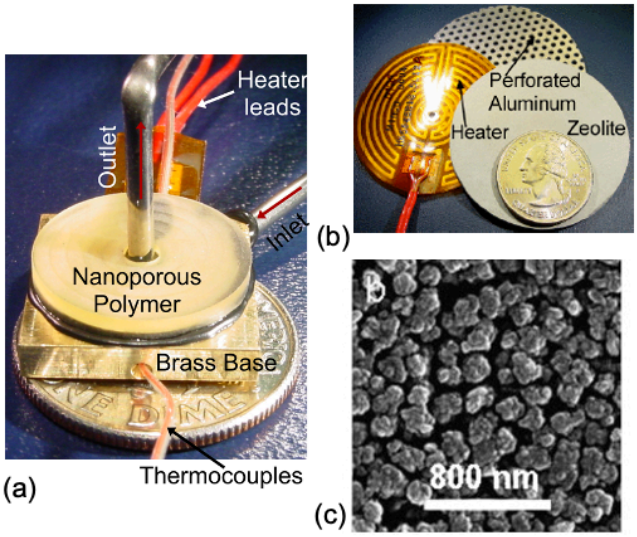

Fig. 1.3: Examples of porous media based KPs. (a) Nanoporous polymer based KP [Gup11], (b) Naturally occurring zeolite based KP [Gup08], (c) SEM image of the porous zeolite [Hua10].

ments. The previously reported lithographically microfabricated KPs have provided superior performance compared to the porous media based KPs. Cascading single-channel KPs (as narrow as 100 nm) serially have achieved relatively high blocking pressures up to 101.2 kPa and compression ratio values >800 for vacuum generation (Fig. 1.4a) [An13, Ino19, McN05, Toa18]. Silicon-on-insulator (SOI) through-wafer KPs incorporated a large number of vertically-oriented parallel pumping channels in the device layer and vertical perforations in the handle layer to pass the gas flow through the wafer. The pumping channels of the SOI through-wafer KPs occupied significantly smaller footprint per channel compared to the KPs that achieved high blocking pressure via lateral channels. Such KPs with 2 µm wide vertically-oriented parallel pumping channels have achieved high flow rates up to 200 sccm (Fig. 1.4b) [An14, An15, Gup12]. However, concurrently achieving high blocking pressure and flow rate necessary for µGCs, which require moderate flow with a moderate pressure head, has been a persistent challenge (Fig. 1.5).

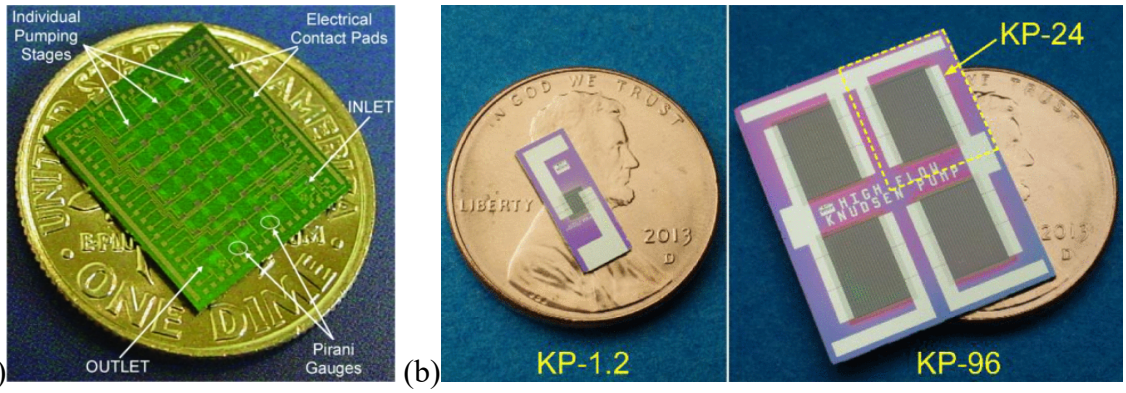

Fig. 1.4: Lithographically microfabricated KPs. (a) Single-channel 162-stage KP with high blocking pressure [Gup12]. (b) Single-stage high-flow KP with densely arrayed parallel pumping channels [An15].

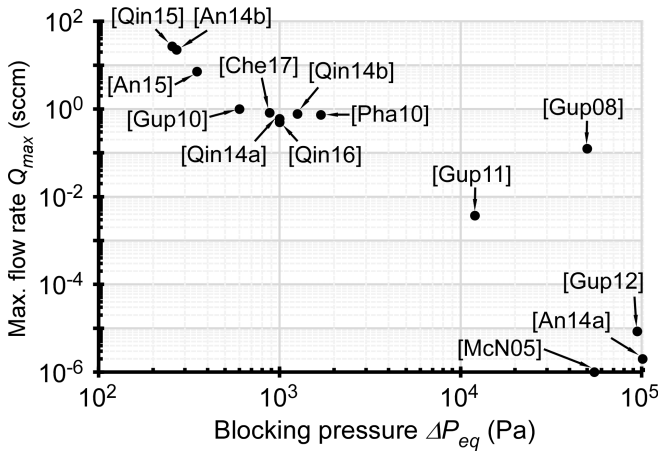

Fig. 1.5: Maximum flow rate and blocking pressure of KPs in literature.

To increase the blocking pressure of the high-flow KPs, the cascading of multiple stages with external tubing, and stacking of stages have been reported [Qin15]. However, in the former approach with external tubing, the external fluidic connections increase the overall internal volume, parasitic flow resistance, dead volume, and response time (Fig. 1.6a). In the latter approach with stacking, the thermal crosstalk between stages limits the scalability and performance (Fig. 1.6b). Both approaches require substantial assembly effort, which increases the manufacturing cost and risk.

(a) 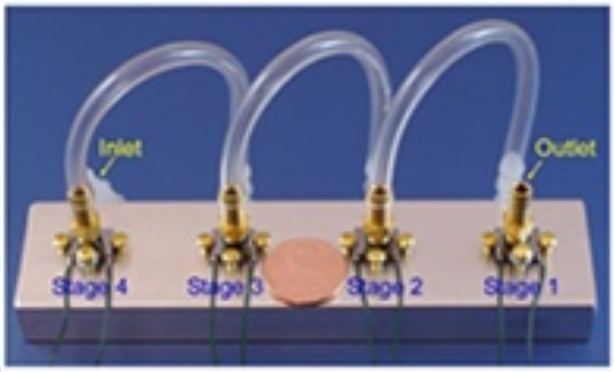

(b) 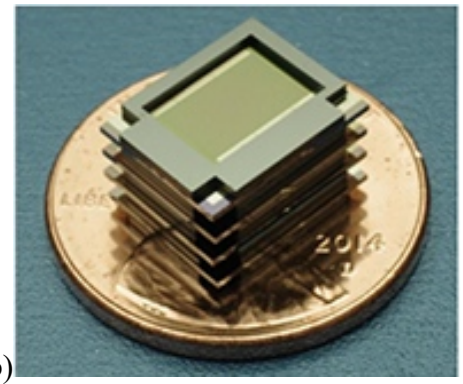

Fig. 1.6: 4-stage KPs (a) planar arrayed with external tubes, and (b) vertically stacked with external frames. [Qin15].

1.3. Thesis Goals

This thesis is focused on developing reliable KPs that can generate operational performance, *i.e.,* flow rate and pressure head, for state-of-the-art μGC systems. The first objective of this thesis is to develop and evaluate KPs with suspended membranes for their ability to achieve both high flow rate and pressure head in a well-balanced manner through a large number of thermally isolated pumping channels. The second objective is to develop and evaluate mechanical robust KPs with high process yield and reliability, which are amenable to monolithic integration of the KPs onto lab-on-a-chip gas analysis systems. For this objective, an unsuspended KP structure is envisioned.

As the number of gas species for chromatography increases, adequate separation and resolution between the species require the longer separation column [McN19], which increases the fluidic resistance and thus requires a higher performance pump. An optimal separation flow rate of the comprehensive, state-of-the-art μGC system described in [Lia21] is 0.4-0.5 sccm. The required performance can be provided by a KP with a blocking pressure of at least 2-3 kPa and a maximum flow rate of 0.8-1.2 sccm. The combination of such performance generates a separation flow rate

of 0.4-0.5 sccm at a pressure head of ≈1 kPa when implemented in the described μGC system. Figure 1.7a illustrates the determination of the operating point of a KP, *i.e.*, operating pressure and flow rate, when connected to a μGC system. Such pumping performance requirement is at least ≈25% higher in maximum flow rate and ≈3× higher in blocking pressure than previously reported efforts on μGC-compatible KP [Che17, Gup10, Pha10, Qin14a, Qin14b, Qin16].

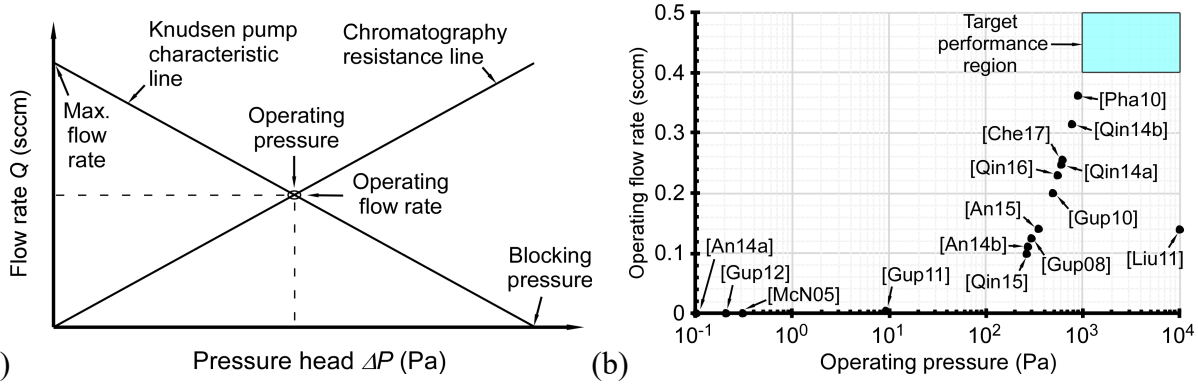

Fig. 1.7: (a) Determination of KP operating point (operating pressure and flow rate) connected to a μGC system. (b) Calculated operating points of KPs in literature, connected to a μGC system with ≈2.5 kPa/sccm fluidic resistance.

Achieving high performance in KPs has been challenging due to several factors. As described in Section 1.2, the pumping channel width determines the balance between flow rate and blocking pressure. For example, a large number of 2 μm wide, through-wafer parallel pumping channels achieved high flow rate whereas a series of single pumping channels as narrow as 100 nm achieved high blocking pressure. For both high flow rate and high blocking pressure, a large number of through-wafer parallel pumping channels with a small channel width (≈1 μm) is necessary. Some of the methods to improve the performance and functionality of the KPs are as follows.

First, a popular method of increasing the pressure head of KP is to serially connect multiple pumping stages to build up the pressure head stage-to-stage [An13, Gup12, Liu11, McN05, Qin15].

However, prior efforts lacked monolithic microfabrication methods and ease of assembly that can provide high yield [Liu11, Qin15]. One of the objectives of this thesis is to design a monolithic multi-stage KP with on-chip stage-to-stage fluidic connection to scale the blocking pressure and provide simpler assembly.

Second, to improve the blocking pressure within the individual pumping stage, the width of the pumping channels can be reduced [An13]. Narrower channel width significantly increases the pressure head while minimally reducing the gas flow rate minimally as a tradeoff. Figure 1.8 illustrates the effect of pumping channel width on the performance, given the same active pumping region and applied power. The KP used for this calculation is described in Chapter 2. The number of parallel pumping channels doubles in the same area when the pumping channel width is halved, which results in similar maximum flow rate while the blocking pressure scales inversely proportional with the channel width. However, reducing the pumping channel width is limited by the fabrication capabilities.

Third, in addition to the width, the pumping channel length can be adjusted to achieve the target performance. The thermal conductance C between the heated active pumping region and cooled heat sink region can be expressed as [Bej03],

$$C = k\frac{A}{l} \tag{1.3}$$

where k is the thermal conductivity, A is the area, and l is the length. Longer pumping channels can decrease the thermal conductance, hence the heat loss between the heated and cooled region and increase the temperature difference along the channels at a given power level. This method of increasing the temperature difference can increase the blocking pressure of the KP whereas the flow rate may deteriorate due to the increased flow resistance of the channels. Furthermore, the fabrication of long pumping channels is challenging due to the process and tool limitations.

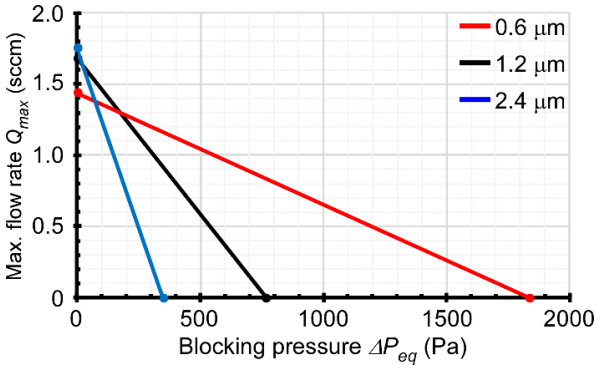

Fig. 1.8: KP performance variation with respect to the pumping channel width.

Fourth, the flow rate of the KP is proportional to the number of heated parallel pumping channels. Methods of increasing the number of parallel pumping channels have been explored in prior work [An15]. First, a KP-96 chip with 96 mm^2 active pumping area was diced into four KP-24 chips, each with 4×6 mm^2 active pumping area and ~10^5 parallel pumping channels (Fig. 1.3b). The individual KP-24 chip provided a maximum flow rate of ≈100 sccm and a blocking pressure of ≈400 Pa. Second, without dicing, the KP-96 chip provided a maximum flow rate of ≈290 sccm and a blocking pressure of ≈400 Pa. This method of scaling the flow rate through the number of parallel pumping channels is further explored in both the suspended and unsuspended KP designs.

Fifth, the process yield and mechanical robustness of the suspended membrane based KPs are studied. The mechanical stress of the suspended membrane is crucial for reliable operation. The total stress of silicon nitride and oxide composite film is typically tuned at mild tensile level such that it provides safe operation [Gup12, An15]. Whereas featureless thin dielectric membranes can be mechanically robust [Bya17], the membranes with perforations for the through-wafer gas flow can have high stress concentration that could exceed the fracture stress of the film and fracture [Ben19]. This upper boundary of stress depends on various parameters such as the composite stress, perforation size, and location. At an elevated temperature during operation, thermal tensile stress is partially or fully relieved. In combination with the metal heater's mismatched expansion,

the suspended membrane stress could become compressive and buckle if the compressive stress exceeds the Euler's load of the membrane. This lower boundary of stress depends on variables such as composite stress level, operation temperature, and membrane size. In this thesis, the design and stress levels of KP are studied for process yield and operation reliability.

Lastly, the unsuspended design of KP is explored in this thesis. By eliminating the suspended membrane, the fabrication process yield and operation reliability are anticipated to improve drastically. The performance of the unsuspended KP is tailored for the monolithic lab-on-a-chip gas analysis system with compact components compared to the comprehensive μGCs. However, achieving high temperature difference along the pumping channels for sufficient performance can be challenging for the unsuspended structure. The forementioned lithographically microfabricated KPs, both high-pressure and high-flow [An13, An14, An15, McN05, Gup12], employed a suspended dielectric membrane as the heated region, and as a thermal isolation between the heated region and cooled region in order to generate high temperature difference along the pumping channels (Fig. 1.9). Furthermore, the high-flow KPs have implemented 10 nm thick dielectric pumping channel sidewalls to achieve a large number of densely arrayed pumping channels with low thermal conductance [An15]. The fabrication of such architectures can be challenging due to their complexity. Some of the challenging steps include the deep reactive ion etching (DRIE) for the pumping channel trenches [Ish99, Zhu05], low-pressure chemical vapor deposition (LPCVD) to refill the trenches, deposition of the membrane [An14, Che20, Qia10, Shi14] and membrane stress control to avoid fracture and buckling [Ben19, Che20, Elb97]. Figure 1.9 shows the footing and bowing effects of DRIE, which generate pockets of unfilled region at the bottom (Fig. 1.10a) and near the top (Fig. 1.10b), respectively. The LPCVD of the DRIE trenches with such defects could generate an unrefilled space or a keyhole (Fig. 1.10c), which could result in defective

membrane and overhanging beams (Fig. 1.10d). As an alternative to this fabrication process sequence, the unsuspended KP design with superior mechanical robustness is explored in this thesis.

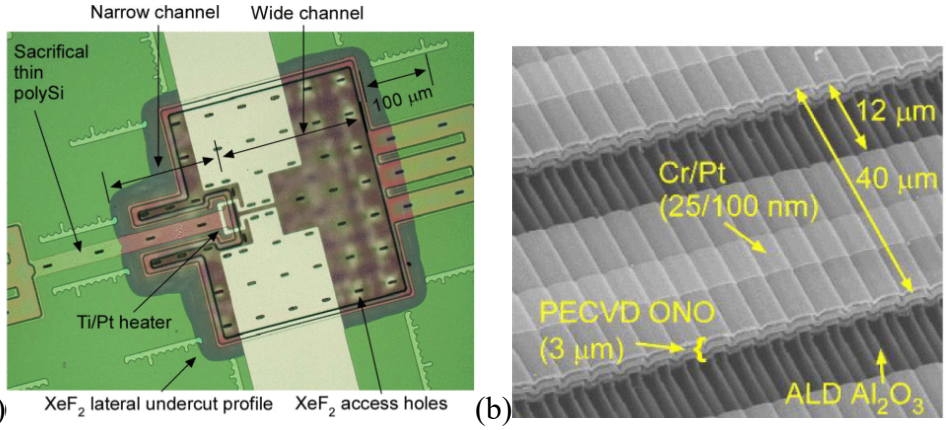

Fig. 1.9: Lithographically microfabricated KPs with suspended membranes. (a) A single-channel pumping stage of a 162-stage KP with high blocking pressure [An13]. (b) High flow KP with densely arrayed pumping channels [An15].

1.4. Organization of Thesis

This thesis comprises of the following five chapters. All KPs presented in this thesis are lithographically microfabricated through an SOI wafer.

Chapter 2 introduces the Generation (Gen) 1 KP of this thesis. The Gen S1 KP comprises of four monolithic pumping stages with suspended membranes. The stage-to-stage gas flow is routed through monolithic through-holes. The Gen S1 4-stage KP provides high flow rate and high blocking pressure suitable for μGC applications. The high flow rate is achieved with the densely arrayed parallel pumping channels whereas the high blocking pressure is achieved with 1.2 μm wide pumping channels and series arrangement of the pumping stages. The suspended membrane provides high temperature different along the pumping channels.

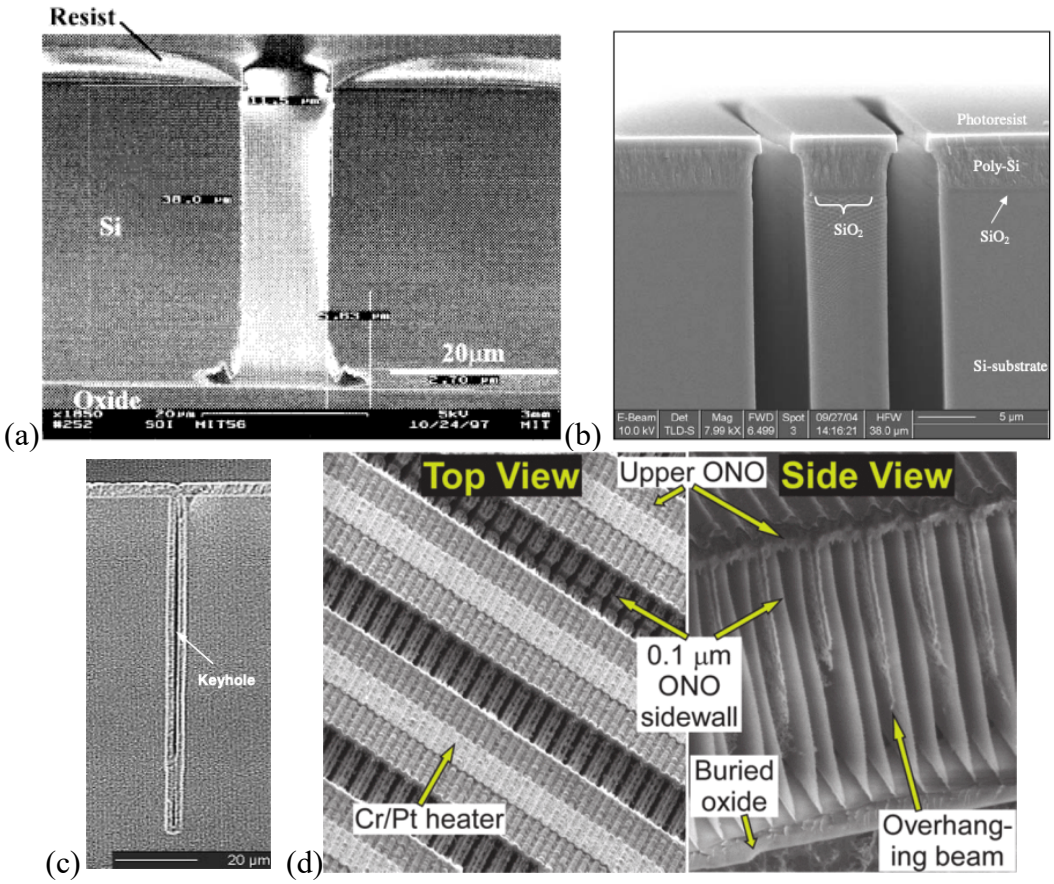

Fig. 1.10: (a) Footing and (b) bowing effects of DRIE [Ish99, Zhu05]. (c) Keyhole generated by LPCVD due to the footing and bowing effects [Zhu05]. (d) Defective overhanging beam due to the keyholes [An14].

Chapter 3 describes the mechanical and thermal refinement of the Gen S2 KPs via modeling. Several groups of KP designs are investigated to refine the mechanical stress of the suspended membrane to avoid fracture and buckling. A relatively uniform temperature distribution across the active pumping region is achieved by refining the metal heater layout. A scalable multi-stage KP design is presented.

Chapter 4 describes the Gen S2 KPs with the refined suspended membranes. The Gen S2 KPs comprises of five monolithic pumping stages and through-holes for gas flow routing. The longest pumping channels in SOI through-wafer KPs to date are employed to achieve higher temperature difference along the channels and thus a higher blocking pressure compared to Gen S1 KP.

Chapter 5 introduces the Gen U1 KP without any suspended membrane. The unsuspended Gen U1 KPs provide mechanical robustness and facile fabrication process compared to the KPs with suspended membranes. The performance of the Gen U1 KP is suitable for providing chemical vapor sampling and separation for certain μGCs.

Chapter 6 concludes this thesis and discusses about the future work.

Chapter 2:

Gen S1: Suspended Monolithic 4-Stage Knudsen Pump for Microscale Gas Chromatography Applications

2.1. Introduction

Previously reported KPs have demonstrated either high flow rate (without the ability to drive a pressure head) or high blocking pressure (without the ability to drive continuous flow); achieving both concurrently, as is necessary for gas chromatographs (which require moderate flow with a moderate pressure head), has been a persistent challenge [An14, An15, Ino19, McN05, Qin15, Toa18]. Cascaded single-channel KPs have demonstrated relatively high blocking pressures up to 101.2 kPa and compression ratio values >800 for vacuum generation [An14, Ino19, McN05, Toa18]. KPs with densely arrayed parallel channels have achieved high flow rates up to 200 sccm [An14, An15]. To increase the blocking pressure of high-flow KPs, the cascading of multiple stages with external tubing, and stacking of stages have been reported [Qin15]. However, in the former approach, the external fluidic connections increase the overall internal volume, parasitic flow resistance, dead volume, and response time. In the latter approach, the thermal crosstalk between stages limits the scalability and performance. Both approaches require substantial assembly effort, which increases the manufacturing cost and risk.

This chapter presents a monolithic 4-stage Gen S1 KP with suspended membrane. The KP provides a modest flow rate ≈0.75 sccm and high blocking pressure ≈3.3 kPa, which is suitable for μGC applications. With on-chip gas flow connections between the stages, the entire KP in this work is implemented in a single planar chip, eliminating the fluidic, thermal, and assembly

challenges encountered in the previously reported devices. The pumping stages comprise vertical channels for thermal transpiration that are micromachined into a silicon-on-insulator (SOI) wafer; the stages are connected to each other through horizontal lateral channels micromachined into glass wafers that are bonded above and below the SOI wafer.

2.2. Design and Modeling*

The 4-stage Knudsen pump essentially comprises an SOI die sandwiched between two glass dies. The SOI die incorporates pumping stages and through-holes, whereas the two glass dies incorporate lateral channels (Fig. 2.1). The lateral channels and through-holes are arranged to connect the four pumping stages in series. Each pumping stage creates an upward gas flow through vertical channels in the SOI die, and this flow is routed by the corresponding lateral channels and through-hole to the next stage.

Each pumping stage is composed of three regions: an active pumping region, a substrate frame region, and a thermal isolation region between the other two regions. The active pumping region incorporates dense arrays of rectangular vertical pumping channels within an area of 0.4×0.5 mm^2. Each pumping channel has width a =1.2 μm, depth b =18 μm, and length l =12 μm in x, y, and z directions, respectively. In such a geometry, the channel width limits the effective hydraulic diameter to be ≈1.2 μm. The pumping channel sidewalls are comprised of a 10 nm-thick Al_2O_3 dielectric layer. The 10 nm thickness is intended to reduce thermal conductance along the flow path, while maintaining adequate mechanical robustness. With thermal conductivity of 1.8-3.3 W/mK [An15], the 10 nm-thick wall Al_2O_3 provides thermal conductance along the flow path

**The design and modeling have been performed by Dr. Qisen Cheng.*

that is comparable to the 1.2 μm-wide channel of air. Within the SOI die, the pumping channels are supported by a suspended upper dielectric membrane from above and a Si heat sink from below. The suspended upper dielectric membrane is a composite of silicon oxide-nitride-oxide-nitride-oxide (ONONO) layers. Both the suspended membrane and the Si heat sink incorporate periodic rectangular openings (18×160 μm^2 for the former and 29×270 μm^2 for the latter) to allow gas flow. A thin-film metal (Cr/Pt) heater is patterned on top of the membrane.

The substrate frame region is used for overall device support. The thermal isolation region separates the active pumping region from the substrate frame by 180 μm to confine the heat within the active pumping region. The thermal isolation region is formed by arrays of vertical channels that are fully covered by the upper dielectric membrane and have no contribution to the pumping.

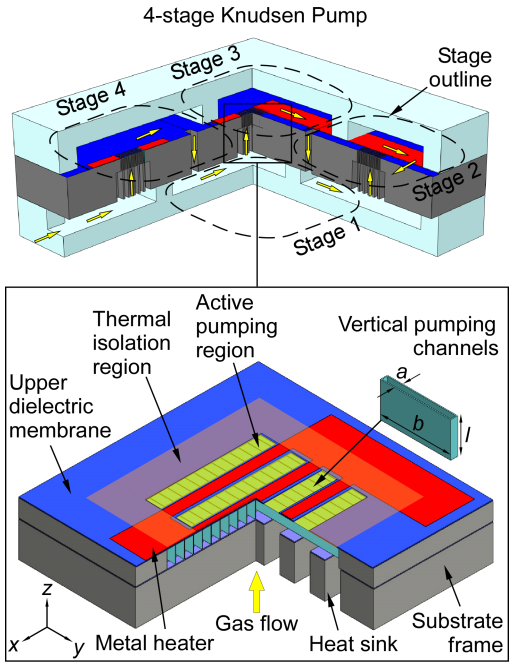

Fig. 2.1: A 4-stage Knudsen pump structure showing the arrangement of pumping stages and various features within each stage.

The gas molecules pumped upwards by each pumping stage are routed through a lateral channel in the front side glass die, an array of through-holes in the SOI die, another lateral channel in the back side glass die, and into the next stage. The lateral channels are 2.2 mm long, 1.3 mm wide, and 0.4 mm deep. The array of through-holes includes 6 parallel through-holes, each with an opening area of 29×270 μm^2.

Compared to prior work [An15, Qin15], the Gen S1 KP incorporates three main design improvements. First, by using a 3-wafer structure, this KP monolithically integrates four pumping stages within a compact footprint (5×7.5 mm^2). Second, the active pumping region of each pumping stage in this KP is 6× smaller than those in the previous KPs, which provides more concentrated heating and superior performance at a given power. Third, the vertical pumping channels in this KP are 40% narrower than those in the previous KPs, which substantially increases the blocking pressure, particularly when operated at atmospheric pressure.

The final design resulted from extensive modeling of the temperature distribution using finite element analysis (FEA) and fluidic analysis using semi-analytical calculations. The temperature distribution modeling included two steps. The first step simulated the temperature distribution over the entire device (Fig. 2.2a), whereas the second step simulated the localized temperature distribution along a single pumping channel (Fig. 2.2b). The fluidic analysis included two parts: the estimation of flow and pressure at atmospheric pressure (Fig. 2.3a) and dimensional scaling of the pumping channels and fluidic connections (Fig. 2.3b).

Because of the geometrical symmetry, the temperature distribution of the device was represented by the half structure of two neighboring pumping stages. The thermal conductivities of the unpatterned dielectric membrane and the metal heater were calculated from the thermal conductivity of each layer within the membrane and heater, respectively, weighted by layer

thickness. Following that, the effective thermal conductivities of the patterned structures, which include the pumping channels, heat sink, upper dielectric membrane, and metal heater, were calculated as an areal average over the perforated and non-perforated regions of the structures. Table 2.1 summarizes the calculated effective thermal conductivity of each patterned structure.

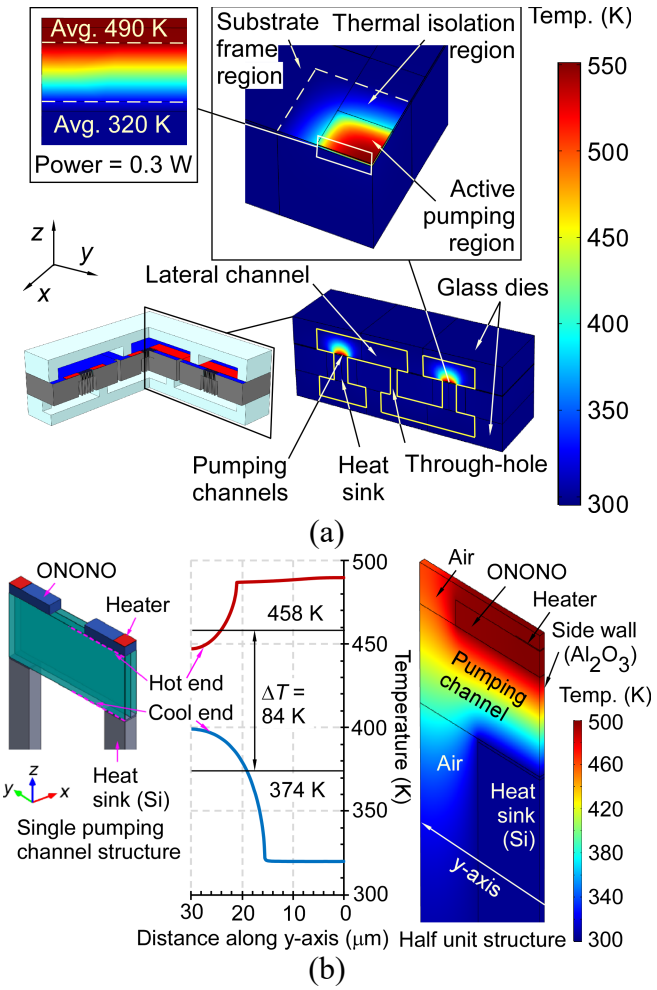

Fig. 2.2: FEA simulations of KP. (a) FEA of temperature distribution over single and multiple pumping stages. The gas flow path is indicated by the light-yellow lines. (b) FEA of temperature distribution of single pumping channel structure.

Table 2.1: Material properties assumed in the FEA

Structure	Material composition	Effective thermal conductivity (W/mK)
Pumping channels	Al_2O_3/air	0.3-0.4 (temperature dependent)
Heat sink	Si/air	56
Suspended upper dielectric membrane	ONONO/air	11
Metal heater	Cr/Pt/air	15

In the simulations, the bottom of the back side glass die was assumed to be at room temperature (295 K), which is maintained during testing. With 0.3 W power applied to the active pumping region (Fig. 2.2a), the hot-side temperature ranged from a minimum of 395 K to a maximum of 551 K, with an *average* hot-side regional temperature, $T_{h.p}$, of 490 K. This average was calculated over the entire region; it does not necessary represent the hot side temperature in the single pumping channel, which is addressed separately below. Meanwhile, the cold-side temperature of the active pumping region ranged from a minimum of 302 K to a maximum of 330 K, with an average cold-side regional temperature, $T_{c.p}$, of 320 K. From the simulation results, the $T_{h.p}$ was noticeably affected by the width of the thermal isolation region. Reducing the thermal isolation region width in half to 90 μm reduced the $T_{h.p}$ to 445 K. In contrast, doubling the thermal isolation region width to 360 μm increased the $T_{h.p}$ to 495 K. Considering the compromise between the device area and the $T_{h.p}$, the thermal isolation region width was designed to be 180 μm.

Within a single pumping channel (Fig. 2.2b inset), the dimensions of the perforation in upper dielectric membrane and the lower opening between adjacent fins of the silicon heat sink can have significant impact on the temperature gradient available for driving the thermal transpiration flow. In this simulation, the $T_{h.p}$ was applied to the heater, whereas the $T_{c.p}$ was applied to the top surface of the heat sink fin (proximal to the pumping channel). At the hot end of the open region of the pumping channels, the temperature reached a minimum of 448 K at the center of open region, a maximum of 487 K at the edge, and an average hot-side open channel temperature, $T_{h.p.open}$ of 458

K. At the cold end of the open region of the pumping channels, the temperature reached a maximum of 402 K at the center of open region, a minimum of 487 K at the edge, and an average cold-side open channel temperature, $T_{c.p.open}$, of 374 K. From the simulations of overall and localized temperature distribution (Table 2.2), with 0.3 W input power, the temperature difference that is effective for pumping (ΔT) is about 84 K.

Table 2.2: Simulation results of temperatures in the FEA

Temperature	Simulated Results (K)
$T_{h.p}$	490
$T_{c.p}$	320
$T_{h.p.open}$	458
$T_{c.p.open}$	374
ΔT	84

As described above, there are substantial variations in the temperature bias between the hot and cold sides – across the pumping region and between pumping channels: up to 156 K variation over the active region, up to 40 K in the hot-side open channel temperature, and 75 K in the cold-side open channel temperature. While accurate prediction of the pumping performance is extremely complicated by these temperature variations, a coarse estimation of the temperature bias available for pumping can be provided by the average temperature values $T_{h.p.open}$ and $T_{c.p.open}$.

The flow rate generated by a single rectangular pumping channel can be estimated using Sharipov's equation [Sha99]:

$$M = \left(\frac{q_T \Delta T}{T_{avg}} - \frac{q_P \Delta P}{P_{avg}} \right) \frac{a^2 b P_{avg}}{l} \left(\frac{m}{2 k_B T_{avg}} \right)^{0.5} \tag{2.1}$$

where M is the mass flow rate through the single pumping channel; ΔT is the temperature difference between the hot and cold ends, which is equal to ($T_{h.p.open} - T_{c.p.open}$); T_{avg} is the average

temperature; ΔP is the pressure difference applied between the hot (outlet) and cold (inlet) ends (*i.e.,* applied pressure head); P_{avg} is the average pressure; a, b, and l are the pumping channel width, depth, and length, respectively ($a \leq b$); m is the mass of the gas molecule; k_B is the Boltzmann constant; and q_T and q_P are the thermal creep and viscous flow coefficients, respectively, which have been reported in literature [Sha99].

The output flow rate, Q, through the KP can be estimated by multiplying M from Eq. (2.1) by the number of channels and dividing by the mass density of the gas at T_{avg} and P_{avg}. The output flow rate reaches a maximum, Q_{max}, when ΔP is zero. The blocking pressure, ΔP_{eq}, can be calculated from Eq. (2.1) by forcing M to zero. The calculated flow rate decreases linearly with the pressure head (Fig. 2.3a). The pumping channels in a single pumping stage with 0.3 W power is expected to provide a maximum flow rate of 0.87 sccm, and a blocking pressure of 0.62 kPa. They present an internal flow resistance of 0.68 kPa/sccm.

Whereas the heat sinks, through-holes, and lateral channels do not affect the blocking pressure, they can potentially decrease the maximum flow rate. Their flow resistance (R_h) can be calculated by the following equation [Pri16]:

$$R_h = \frac{12\mu L}{wh^3\left(1-0.63h/w\right)} \tag{2.2}$$

where μ is dynamic viscosity of air; L, w, and h are the length, width, and height of the channel, respectively. As summarized in Table 2.3, the calculated flow resistances of the heat sinks, through-holes, and lateral channels are at least an order of magnitude smaller than that of pumping channels. Considering the additional flow resistance, a single-stage KP is expected to provide a maximum flow rate of ≈0.77 sccm and a blocking pressure of ≈0.62 kPa, whereas a 4-stage KP is expected to provide ≈0.79 sccm and ≈2.47 kPa.

As evident from Fig. 2.2a, the temperature gradient within the heat sinks and through-holes is very modest. However, there is a significant temperature gradient along the lateral channel. The average temperatures at the hot and cool end of the lateral channels, *i.e.,* $T_{h.l}$ and $T_{c.l}$, are 400 K and 295 K, respectively. For a hypothetical lateral channel with a hydraulic diameter (D_h) < 30 μm, unwanted thermal transpiration would create reverse flow against pumping, as computed from Eq. 2.1 with the temperature gradient established in Fig. 2.2a. From the calculations (Fig. 2.3), the reverse maximum flow rate ($Q_{r.max}$) would reach 13×10^{-3} sccm for D_h ≈14 μm, and almost completely disappear for D_h >20 μm. The reverse blocking pressure ($\Delta P_{r.eq}$) decreases rapidly with D_h. Therefore, to prevent reverse pumping in the lateral channels, the D_h must be >20 μm. In the current design, the lateral channels have D_h ≈678 μm, hence reverse pumping thermal transpiration can be ignored.

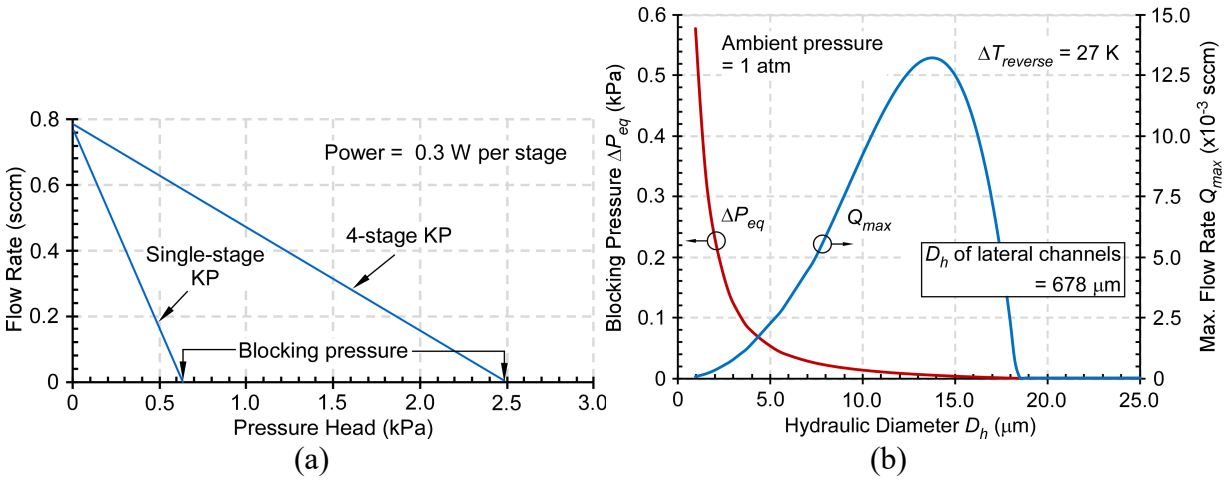

Fig. 2.3: Semi-analytical modeling of KP. (a) Estimation of output flow rate as a function of applied pressure head. (b) Scaling analysis showing the blocking pressure (ΔP_{eq}) and the maximum flow rate (Q_{max}) that result from the 27 K temperature difference across the length of lateral channels of varying hydraulic diameter D_h. For the 4-stage KP, because the D_h is 678 μm in the lateral channels, there is negligible flow due to thermal transpiration.

Table 2.3: Flow resistance of a single stage KP units

Structure	Dimensions - *a/b/l* (μm^3)	Num. of channels	Flow Resistance (kPa/sccm)
Pumping channels	1.2/18/12	1800	0.684
Heat sink	29/270/520	16	0.023
Through-hole	29/270/520	6	0.061
Lateral channel	400/1400/2200	1	0.0001

2.3. Fabrication of Suspended Knudsen Pump

The SOI wafer from which the pumping stages were fabricated had a 12 μm-thick device layer and a 525 μm-thick handle layer, separated by a 0.38 μm-thick buried oxide layer. The fabrication used four masks. The first mask was used to define arrays of rectangular trenches with 1.2×58.8 μm^2 opening and 1.2 μm separation between adjacent trenches along both axes. The trenches were etched through the device layer using the Bosch process of deep reactive ion etching (DRIE) that was performed on an inductively coupled plasma tool (Fig. 2.4a). Next, a 10 nm-thick conformal coating of Al_2O_3 was deposited using atomic layer deposition (ALD) to form the pumping channel sidewalls. The trenches were then refilled with 1.5 μm of sacrificial polysilicon using low-pressure chemical vapor deposition (LPCVD); the deposited polysilicon layer was dry-polished with a selective recipe for plasma etching to expose the Al_2O_3 in the top surface (Fig. 2.4b). The suspended upper dielectric membrane was formed by ONONO composite membrane of 3.1 μm thickness, which was deposited by plasma-enhanced chemical vapor deposition (PECVD) and patterned by reactive ion etching (RIE) using the second mask. The upper dielectric membrane was thick enough to reduce the topological variations resulting from the polysilicon dry-polishing, whereas each dielectric layer in the membrane was tuned to provide a composite tensile stress of approximately 80 MPa (Table 2.4). The resistive metal heater was formed by a Cr/Pt (25/100 nm) film, which is deposited by sputtering and patterned by the lift-off process using the third mask (Fig. 2.4c).

Table 2.4: Measured thickness and residual stress

Structure	Thickness (μm)	Residual stress (MPa)
SOI device layer/buried oxide/handle layer	12, 0.38, 525	NA
Poly silicon	1.5	NA
Suspended membrane (O/N/O/N/O)	0.6/0.6/0.7/0.6/0.6	78
Metal heater (Cr/Pt)	0.025/0.1	-503

The heat sinks and through-holes were fabricated by DRIE through the SOI handle layer using the fourth mask. High aspect ratio DRIE was achieved by a custom recipe tuned for through-wafer features [Tan18]. The challenges and short loop tests associated with the back side DRIE process are described in the following Section 4 of this chapter. Prior to this DRIE step, the back side Al_2O_3 and polysilicon that were deposited in preceding steps were removed by dry-etching. After this DRIE step, the exposed buried oxide was removed by dry-etching. The openings in the heat sinks and through-holes have same dimensions. A second 10 nm-thick ALD Al_2O_3 layer was then deposited to protect the heat sinks and through-holes (Fig. 2.4d) from the subsequent XeF_2 etch. Because of the depth of heat sink and through-hole features, the deposited Al_2O_3 layer near the bottom of the openings on the device silicon layer was expected to be slightly thinner than 10 nm, although its exact thickness was not directly measurable. An anisotropic RIE recipe was used to remove the Al_2O_3 on the bottom of the openings while leaving the Al_2O_3 on the sidewalls of the heat sinks and through-holes. The etch duration was tuned such that the RIE did not remove Al_2O_3 on the heat sink fins and through-hole sidewalls. Next, the sacrificial silicon and polysilicon in the SOI device layer were dry-etched by XeF_2, releasing the pumping channels and through-holes (Fig. 2.4e). The silicon structures within the SOI device layer not intended to be removed remained protected by Al_2O_3 sidewalls that were formed in the preceding steps.

The lateral channels for gas flow routing were patterned by the fifth mask on glass dies and created by sandblasting (available as a service from IKONICS Corp., Duluth, MI, USA). The

glass dies were bonded to the front and back surfaces of the SOI die using a low-viscosity epoxy suitable for die bonding applications (Epotek-377, Epoxy Technology Inc., MA, USA). Finally, silica capillary tubes (with inner diameter ≈250 μm and length ≈4 cm) were attached to the inlet and outlet ports using a high-viscosity epoxy suitable for encapsulation applications (Stycast2850FT, Henkel, Germany) for fluidic connections to the test setup.

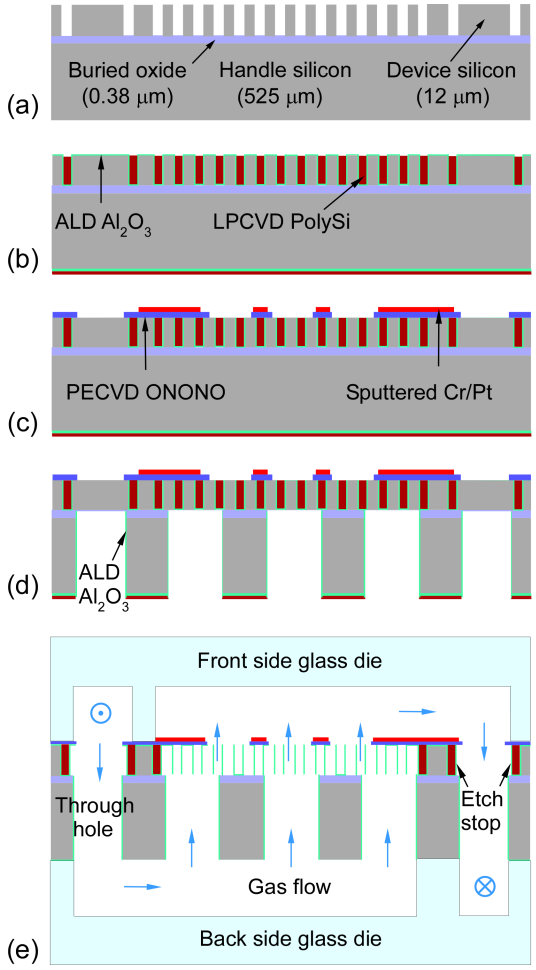

Fig. 2.4: Fabrication process of the multi-stage Knudsen pump. (a) Front side DRIE of the device silicon. (b) ALD of 10 nm thick Al_2O_3 layer for channels and LPCVD of sacrificial poly silicon. (c) PECVD of ONONO membrane and Cr/Pt metallization. (d) Back side DRIE of heat sink. (e) XeF_2 release etch, and bonding of glass dies for gas flow routing and multi-stage operation.

Scanning electron microscopy (SEM) images of the fabricated structures are shown in Fig. 2.5. A cross-sectional view of the Cr/Pt resistive metal heater, suspended upper dielectric membrane, Al_2O_3 pumping channels, and silicon heat sink is shown in Fig. 2.5a. A top view of the active pumping region is shown in Fig. 2.5b. A pumping stage, a lateral channel, and a set of through-hole are shown in Fig. 2.5c. An optical image of a micromachined, fully assembled 4-stage KP is shown in Fig. 2.6.

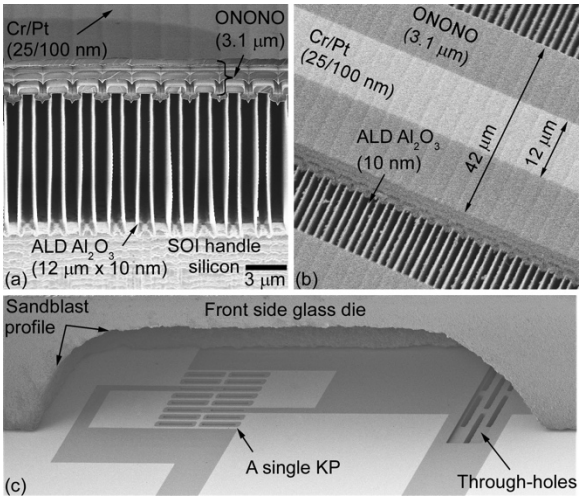

Fig. 2.5: SEM images of the Knudsen pump. (a) Cross sectional view of the ALD channels. (b) Top view of the channels, suspended ONONO membrane, and metal heater. (c) Multi-stage assembly with the front side glass die.

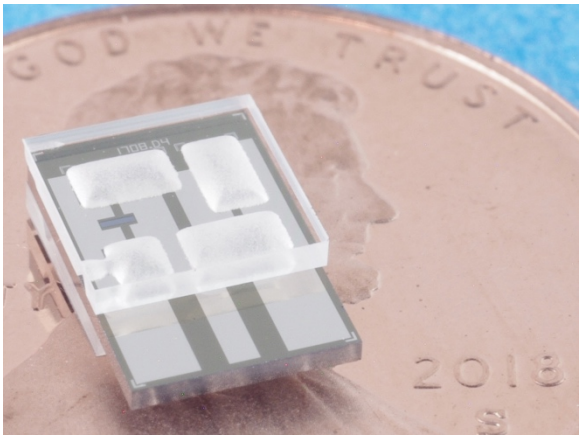

Fig. 2.6: Photograph of a silicon micromachined, fully assembled 4-stage KP chip.

2.4. Through-Wafer DRIE Recipe Modification

The through-wafer DRIE of the SOI handle layer was one of the main challenges of the 4-stage Gen S1 KP microfabrication. As mentioned, the Bosch process was used for its ability to produce high aspect ratio (HAR) anisotropic profile [Wu10, Tan16, Tan17, Tan18]. Table 2.5 contains the parameters of standard DRIE recipes used at Lurie Nanofabrication Facility at the University of Michigan. Recipes *LNF 2* and *3* were designed for deep, through-wafer etch whereas *LNF 1* and *4* were designed for shallow, small-feature etches. According to the internal documents, the undercut of the recipes was measured in etch profiles with depth up to 100 µm. For the deeper etching in this work, the undercut of the standard recipes increased significantly and etched away the features when the undercut exceeded half width of the feature from either side (Fig. 2.7).

Table 2.5: DRIE recipe summary

Recipe	LNF 1		LNF 2		LNF 3		LNF 4		UDRIE		DRIE2	
	Dep.	Etch	Dep.	Etch	Dep.	Etch	Dep.	Etch	Dep.	Etch	Dep.	Etch
ICP Power (W)	2000	2800	2000	2800	2000	4000	2000	2500	2000	2800	2000	2800
Bias Power (W)	0	60	0	40	0	50	0	30	0	60+0.67*T (ramped)	0	140
Pressure (mTorr)	24	30	25	100	25	100	25	30	24+0.067*T (ramped)	30-0.1*T (ramped)	34	15
C_4F_8 flow (sccm)	250	30-0 (ramped)	200	0	200	0	90-140	0	250	30-0 (ramped)	250	30-0 (ramped)
SF_6 flow (sccm)	0	390	0	450	0	600	0	110	0	390	0	390
O_2 flow (sccm)	0	39	0	45	0	60	0	10	0	39	0	39
Time (s)	2.0	2.6	4.0	8.5	4.0	8.5	2.5	7.0	2+0.01*T (ramped)	2.6+0.02*T (ramped)	3.5	5.6
Cooling temp. (°C)	20		20		10		10		20		20	
Average etch rate (µm/s)	4.5		10.4		10.5		3.4		≈4		**3	
*Undercut (µm)	0.2		0.9		1.1		0.2		-		-	

T = etch duration
*Undercut is measured from shallow etch (<100 µm)
**Etch starts at ≈450 µm deep of the trench

In prior work with similar fabrication processes [An15], the standardized etch recipe *LNF 3* was used to etch 22 μm wide trenches in the 380 μm deep handle layer (aspect ratio ≈17.3). According to LNF, the *LNF 3* recipe was designed for a large exposed area (>20%) compared to *LNF 2* recipe for low exposed area (<20%). An's work had large pumping area, hence etch area, designed for high flow rate. The trench width post-DRIE was 26 μm, accounting for 2 μm undercut on each side.

The initial Gen S1 KP design (*Design P1D0*) in this work had 10 μm wide DRIE etch opening and 20 μm pitch. The DRIE aspect ratio was 52.5 to etch through the 525 μm thick handle layer of the SOI wafer with 12/0.4/525 μm thick device/buried oxide/handle layer thicknesses. This work contains a series of short loop tests to determine a recipe suitable for this HAR through-wafer etch. Table 2.6 contains the summary of DRIE tests. SEM images of the test results are shown in Fig. 2.7. Compared to the high flow rate targeted KPs of An [An15], this work has smaller pumping area, targeted for μGC applications. Tests #1 and #2 used *LNF 2* and *3* recipes for 30 min each to distinguish the difference between the two recipes on small etch area samples. Although the KP design layout has <20% exposed area, *LNF 2* recipe resulted in significant undercut and height loss (Fig. 2.7a-b) whereas *LNF 3* etched without any feature loss and with only 1.2 μm undercut (Fig. 2.7c-d). However, in Test #3 for through-wafer etch, a significant undercut and ≈68 μm height loss, *i.e.,* vertical feature reduction with respect to the wafer thickness, were observed (Fig. 2.7e-f) due to lateral etching caused by collisions between etchant ions and etched waste product. Therefore, in *Design P1D1*, the DRIE opening width was increased to 30 μm and the aspect ratio to 17.5 to mitigate the challenge posed by the HAR etch. In Test #4, although through-wafer etch was achieved with 30 μm wide openings, significant undercut and

height loss were observed, indicating that a HAR through-wafer etch is very difficult to achieve with the standard DRIE recipes.

To achieve HAR features for other applications at the University of Michigan, *LNF 1* recipe was customized into an Ultra Deep Reactive Ion Etching (*UDRIE)* recipe for through-wafer etching [Tan16, Tan17, Tan18]. The bias power, pressure, and cycle time were ramped at particular rates, detailed in Table 2.5, such that more bias power, higher deposition pressure, lower etch pressure, and longer time were applied as the process continued. For a 100 min long etch, the final deposition pressure, ramping at 0.067 mTorr/min, would become 30.7 mTorr at T=100 compared to 24 mTorr at the beginning of the etch (T=0). The ramping of the etch parameters provided thicker passivation layer during deposition cycle to improve the protection of the sidewalls, and more effective etching at the bottom of the deep trench during the etch cycle. It took up to 150 min to etch 500 μm deep for ≈10 μm wide features [Tan18].

In this effort to tune the etch recipes, masking has been a challenge for extended DRIE. The SPR 220 7.0 photoresist used in this work yields ≈10 μm thick film at 2 kRMP spin rate, which is the recommended thickness for this photoresist at LNF. However, the 10 μm thick photoresist did not survive the entire through-wafer DRIE process of 120 min etching. In contrast, thicker photoresists (>10 μm) had issues such as cracking and bubbling. The cracking was due to the thermal shock of the thick photoresist post bake or wafer mounting, which can be mitigated through gradual cooling, *e.g.,* moving the wafer from the initial hotplate set at 115ºC to lower temperature hotplates set at 90ºC, 60ºC, etc. with ≈1 min increment. The bubbles formed due to the short wait time between exposure and post exposure bake. At least an hour of wait time has outgassed the exposure byproducts sufficiently and eliminated the bubbles.

In the *UDRIE* recipe development work, a combination of 10 μm thick SPR 220 7.0 photoresist and 5-6 μm thick silicon oxide was used as a mask for 150 min DRIE. In this work, a two-step DRIE that incorporates a modified *UDRIE* recipe was used to achieve a through-wafer etch while avoiding potential issues related with extra thick (>10 μm) photoresist or oxide masking. The first step was a 50 min *LNF 3* recipe with fast etch rate (≈9 μm/min) and more mask selectivity, which etched up to ≈465 μm deep silicon with 30 μm opening at ≈9 μm/min etch rate with reasonable undercut. The second step was a 20 min *DRIE2* recipe, which etched the remaining ≈60 μm gently at ≈3 μm/min without contributing significant undercut due to the thicker passivation layers. The slow etch rate provided more controllability and low footing. The *DRIE2* recipe was equivalent to *UDRIE* recipe at the bottom of the trench, *i.e.,* the recipe parameters were fixed and calculated at *T*=150 min of the *UDRIE* recipe parameter ramps (Table 2.5). The two-step DRIE test (Test #5) results are shown in Fig. 2.7i-j. Through-wafer DRIE was achieved with ≈8 μm undercut and ≈2 μm leftover photoresist. Table 2.6 summarizes the short loop test results. The 4-stage Gen S1 KP in this chapter and 5-stage Gen S2 KP in Chapter 4 were fabricated using this two-step DRIE recipe.

Table 2.6. DRIE short loop test summary

Mask design		[An15]	*P1D0*			*P1D1*		
Test #		-	1	2	3	4	5	
Device/BOX/handle layers of wafer (μm)		20/0.5/380	12/0.4/525					
Opening width (μm)	Designed	22	10	10	10	30	30	
	Fabricated	26	-	12.4	-	-	46	
Pitch (μm)		40	20			60	60	
Designed aspect ratio		17.3	52.5			17.5	17.5	
Etch depth (μm)		380	241	222	337	525	465	60
Height loss (μm)		0	17	0	68	85	0	
Etch duration (min)		-	30	30	55	70	50	20
Recipe		*LNF 3*	*LNF 2*	*LNF 3*	*LNF 3*	*LNF 3*	*LNF 3*	*DRIE2*
Undercut (μm)		2	>5	1.2	>5	>15	8	

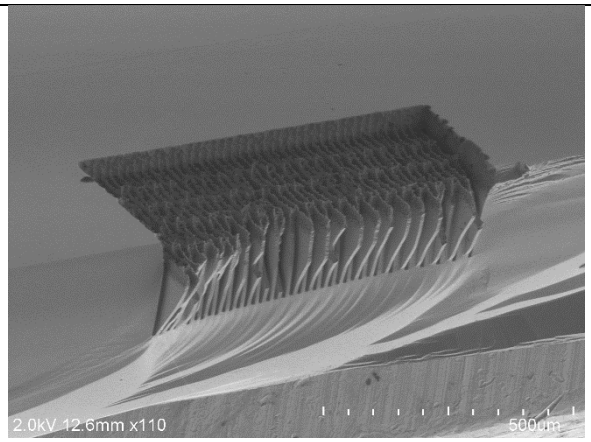

a) Test #1 using *LNF 2* recipe for 30 min

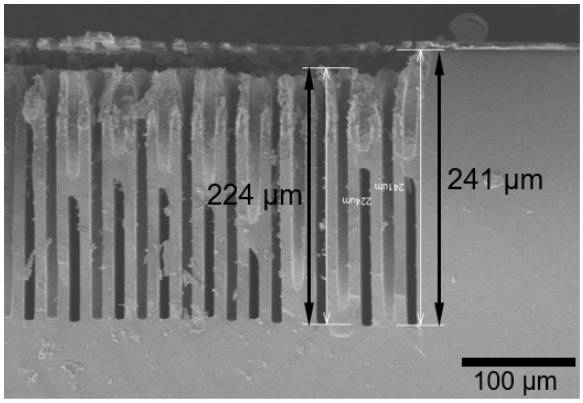

b) Depth measurement of Test #1 (with PR)

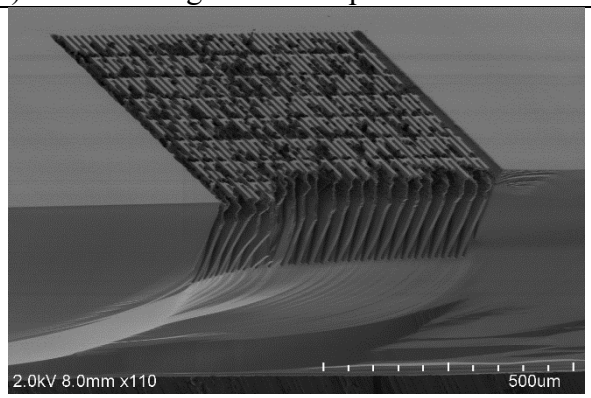

c) Test #2 using *LNF 3* recipe for 30 min

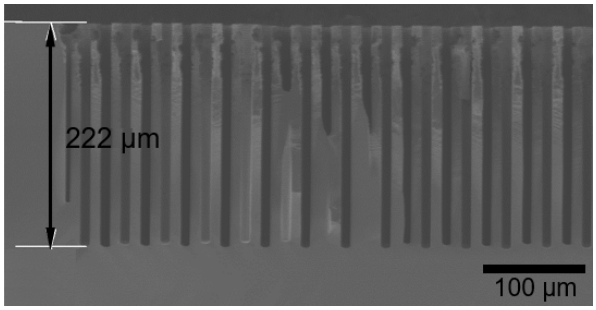

d) Depth measurement of Test #2

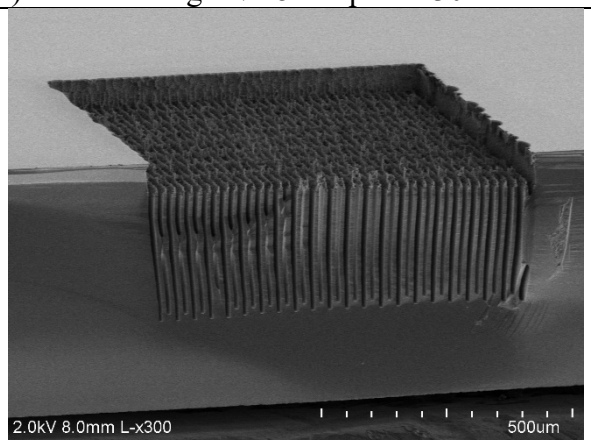

e) Test #3 using *LNF 3* recipe for 55 min

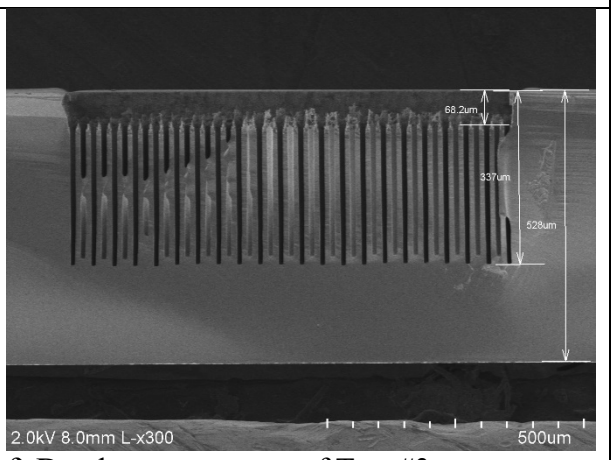

f) Depth measurement of Test #3

Fig. 2.7: SEM images of the DRIE profile and depth measurements on features etched by (a-b) *LNF 2* recipe for 30 min in Test #1, (c-d) *LNF 3* recipe for 30 min in Test #2, (e-f) *LNF 3* recipe for 55 min in Test #3.

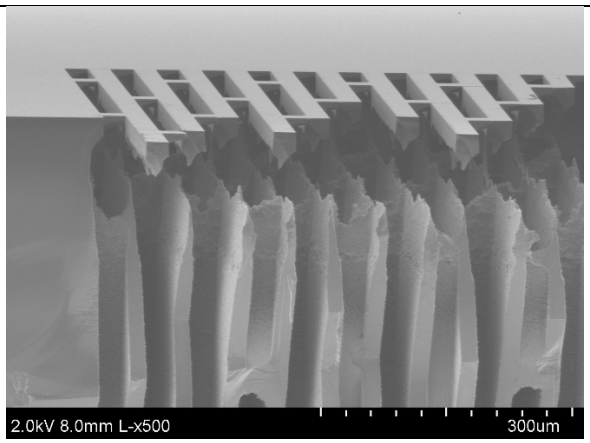

g) Test #4 using LNF 3 recipe for 70 min

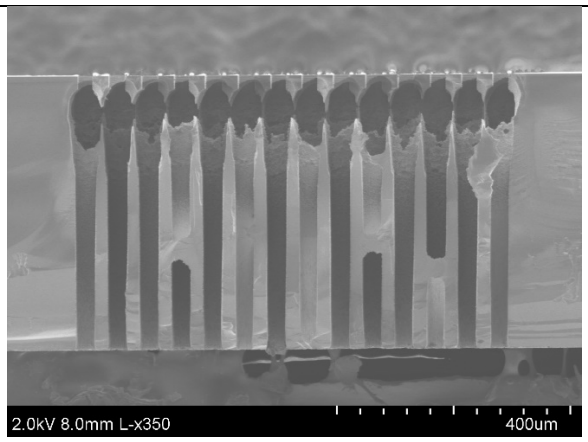

h) Depth measurement of Test #4

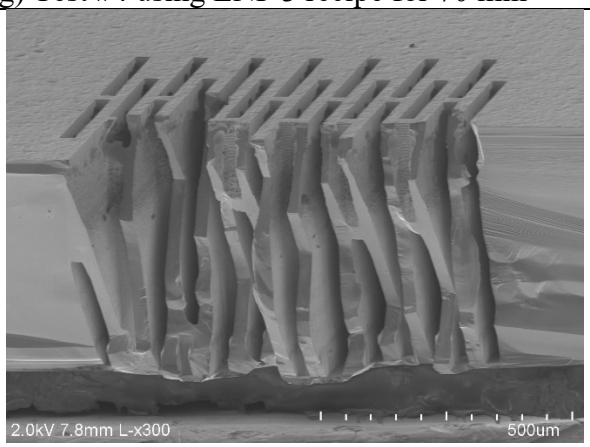

i) Test #5 using *LNF 3* recipe for 50 min and *UDRIE* recipe for 20 min

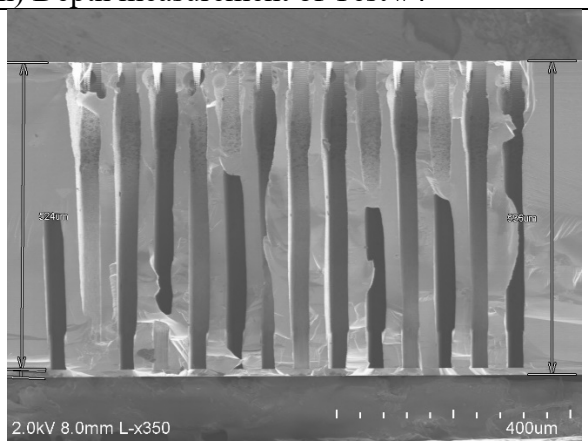

j) Depth measurement of Test #5

Fig. 2.7: (g-h) *LNF 3* recipe for 70 min in Test #4, and (i-j) *LNF 3* recipe for 50 min and *DRIE 2* for 20 min in Test #5.

2.5. Experimental Results

The performance of the Gen S1 KP was evaluated using the setup shown in Fig. 2.8. The KP chip was positioned on the chuck of a probe station where DC power was supplied through two probes. The inlet of the KP was connected to a commercial flow meter (Model # MW-20SCCM-D, Alicat Scientific, Inc., Tuscon, AZ, USA), which presented negligible flow resistance for flow rate measurement. A differential pressure sensor (MPX5010DP, Freescale Semiconductor Inc., Austin, TX, USA) was connected in parallel to the flow path to measure the applied pressure head between outlet and inlet ports of KP.

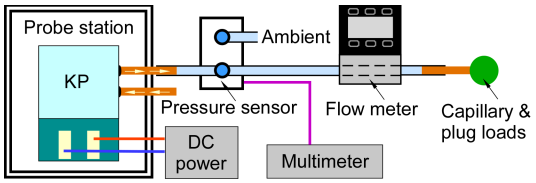

Fig. 2.8: Measurement setup for experimental characterization of Knudsen pump at atmospheric pressure.

The flow rate was measured at various pressure head values with the KP operated at five different power levels from ≈0.2 W to 1.2 W. The applied power was capped at 0.3 W per pumping stage to limit the temperature ≤600 K, which was the estimated damage threshold as determined by FEA. At each power level, the Q and ΔP values were recorded under five different loading conditions – the gas flow path being fully open (with only the flow meter in-line); at three intermediate different pressure heads; and fully blocked. The pressure loading was provided by extra capillary tubes connected to the outlet of the KP.

Three 4-stage Gen S1 KPs (KP1, KP2 and KP3) were experimentally evaluated at steady state conditions (Fig. 2.9). With 1.2 W power, KP1 provided a maximum flow rate of ≈0.76 sccm and a blocking pressure of ≈3.18 kPa; KP2 provided a maximum flow rate of ≈0.74 sccm and a blocking pressure of ≈3.21 kPa; whereas KP3 provided a maximum flow rate of ≈0.75 sccm and a blocking pressure of ≈3.3 kPa. Over the three tested KPs, the standard deviation of the maximum flow rate was 0.007 sccm and <1% of the mean value, whereas that of the blocking pressure was 58.4 Pa and <2% of the mean value.

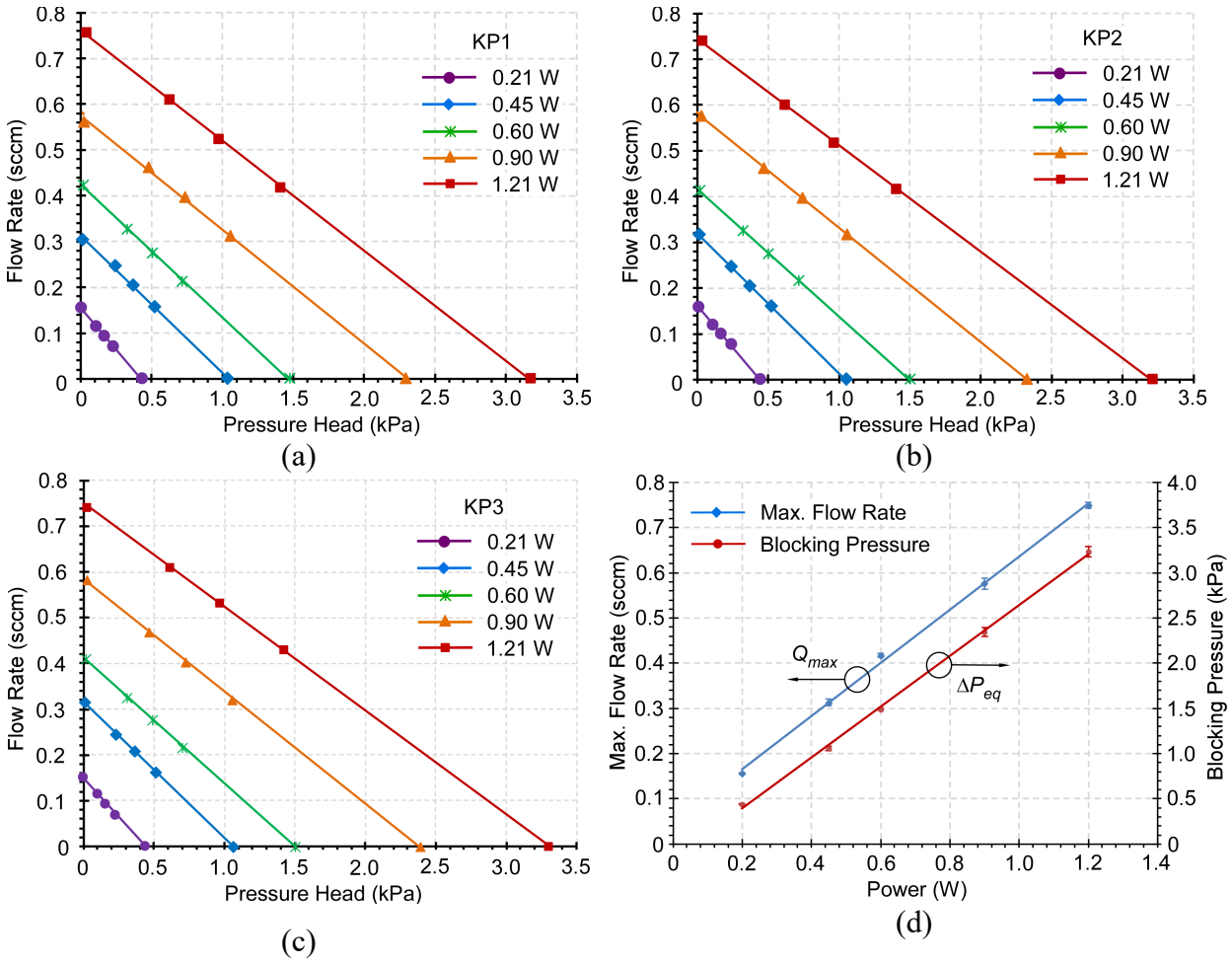

Fig. 2.9: Steady-state experimental results of three Gen S1 Knudsen pumps. (a) Results of KP1. (b) Results of KP2. (c) Results of KP3. (d) The deviation and average values of the maximum flow rate and blocking pressure across the three tested Knudsen pumps. Both the maximum flow rate and blocking pressure increase linearly with power.

For all the three tested KPs, both the blocking pressure and the maximum flow rate increased almost linearly with the applied power, with coefficients of determination of 0.998 and 0.999, respectively (Fig. 2.9d). This performance linearity can provide predictable blocking pressure and flow rate at specific power levels that meet a system requirement.

In our prior work, the blocking pressure of lithographically microfabricated high-flow KP achieved 0.35 kPa for a single-stage KP at 0.6 W applied power [An15]. Similar KPs were arrayed, forming 4-stage architecture with blocking pressure of 0.255 kPa at 8 W applied power [Qin15].

The blocking pressure achieved in the current work is an order of magnitude higher at 1.2 W applied power.

2.6. Discussion and Conclusion

To assess the KP performance for μGC applications, a pumping efficiency (η) has been defined as follows:

$$\eta = \frac{Q_{op} \cdot \Delta P_{op}}{W_p^2} \tag{2.3}$$

where Q_{op} is the flow rate at operation point, ΔP_{op} is the pressure head at operating point, and W_p is the applied power. The operating point is the intersection of the KP performance line with a typical μGC system load line [Qin16]. In the denominator of Eq. 2.3, the W_p is squared because for a given KP and a given load line, both Q_{op} and ΔP_{op} are approximately proportional to W_p. Figure 9 shows the benchmarking of the KPs that have been reported for μGC applications. The η of the 4-stage KP in this effort is at least 2.7× higher than previously reported KPs.

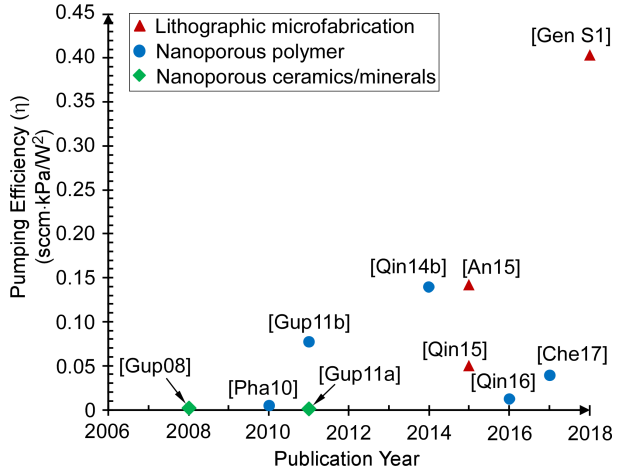

Fig. 2.10: Benchmarking of the KP pumping efficiency for μGC applications. The pumping efficiency of the 4-stage KP in this chapter is at least 2.7× higher than previously reported KPs.

As noted in Section 2.1, μGC systems in literature typically require 0.1-1 sccm flow rate at a pressure head of 1-10 kPa. If the total flow resistance in the analysis path of a μGC system is 3.8 kPa/sccm or smaller, the 4-stage KP in this work can provide a flow rate of at least 0.4 sccm. For example, for the μGC system reported in [Qin16], the Gen S1 4-stage KP, using 1.2 W power, can provide a flow rate of 0.5 sccm at a pressure head of 1.2 kPa, which exceed the requirement of that type of μGC system.

Compared to the modeling results, the experimental results showed up to 5% lower maximum flow rate and up to 30% higher blocking pressure. The discrepancies between the modeling and experimental results are potentially caused by three factors. First, the modeling estimates the pumping performance based on average temperature, but the temperature variations over the pumping structures are relatively large. Second, the material properties assumed in the modeling may have inaccuracies because of the approximations applied to the composite membranes. Third, these discrepancies may be caused by non-idealities associated with fabrication conditions. For example, DRIE could potentially create tapering depending on the tool conditions, which could result in non-vertical sidewalls pumping channels and heat sink fins. While the tapering does not impact the thickness of Al_2O_3 pumping channel sidewalls, the incline and profile of the sidewalls are determined by the taper angle and scalloping of the front side DRIE of the device layer, which were 89.35º and 0.2 μm, respectively.

The compactness of the 4-stage KP design can be further improved by reducing the lateral distance between the pumping stages and the through-holes. The temperature distribution model (Fig. 2.2a) shows that the through-hole temperature is unaffected by heating of the pumping stage. The distance between each pumping stage and its neighboring through-hole can be reduced by up

to 500 μm without affecting the pumping performance, effectively reducing the size by 1 mm in each planar direction.

The fabrication process used in this work allows monolithic co-fabrication of temperature sensors. Implemented near or far away from the metal heaters, temperature sensors can be used to avoid operating the device in an overheated condition that can cause structural damage or monitor the substrate temperature. The difference between the two, heater and substrate temperature, can be used to estimate the temperature difference along the pumping channels.

In summary, this chapter presents a monolithic Gen S1 4-stage KP suitable for microscale gas chromatography applications. The 4-stage KP achieved a total blocking pressure of ≈3.3 kPa and a maximum flow rate of ≈0.75 sccm at 1.2 W applied power. The modeling and experimental results verified the blocking pressure scalability of the on-chip multi-stage configuration. The demonstrated performance is suitable for certain μGC systems. Future work includes further refinement of each pumping stage and cascading more stages monolithically, which will enable applications to other μGCs that require higher blocking pressure or even as a roughing pump in GC-MS systems.

Chapter 3:

Design Refinement and Performance Scaling of the Suspended Multi-Stage Knudsen Pumps

This chapter describes the design refinement of the lithographically microfabricated SOI through-wafer KPs based on extensive FEA. Section 3.1 covers the mechanical refinement of the suspended dielectric membrane. Based on the experimental work in Chapter 2 and more precise modeling of the Gen S1 KP in this chapter, the upper and lower stress boundaries of the suspended membrane are identified. The upper stress boundary is the stress level that can fracture the membrane and break the electrical connection. The lower stress boundary is the stress level that can buckle the membrane at an elevated temperature during operation. The Gen S2 KP designs are refined through investigating various designs to reduce the maximum stress that can cause fractures while maintaining the minimum stress above buckling. Some of the design variations include reduced membrane width for increased buckling load, increased radius of curvature of the membrane perforation for reduced stress concentration, and additional perforations in the thermal isolation region for reduced tension. The Gen S2A KP design has one elongated suspended membrane of 0.45×1.24 mm^2 with a maximum feature stress of 292 MPa whereas the Gen S2B KP design has two smaller suspended membranes of 0.4×0.45 mm^2 with a maximum feature stress of 189 MPa.

Section 3.2 covers the thermal refinement for more uniform heating of the active pumping region. As described in Chapter 1, the KP's performance is directly associated with the heating of

the hot side, *i.e.,* the active pumping region in the suspended membrane. The underheated pumping channels can cause inadequate performance whereas the overheated suspended membrane and pumping channels can break. In this section, a thermally and electrically coupled model is developed to investigate the Joule heating of the metal heater on the suspended membrane more closely to reality. Consequently, the metal layout of each design is refined such that the temperature distribution across the active pumping region is relatively uniform. While this approach consumes more power, especially to heat up the pumping channels near the thermal isolation region, a higher performance is anticipated as a tradeoff.

Section 3.3 covers the performance scalability of the Gen S2 KPs. A 17.3×20.3 mm^2 die consists of six 5-stage KPs and can be diced into 5-, 10-, 15-, 20-, or 30-stage KPs. The blocking pressure of the 30-stage KP can scale up to 23 kPa while maintaining a maximum flow rate of 1.5 sccm by connecting the pumping stages in series whereas its maximum flow rate can reach 45 sccm with a parallel connection while maintaining a blocking pressure of 0.77 kPa. Such scaling could provide the target performance for specific applications.

Table 3.1: Summary of various KP designs and parameters under analysis for mechanical refinement.

Design /Group	Upper dielectric membrane (mm^2)	Active pumping area (mm^2)	Pumping perf. shape	Pumping perf. corner	Stress-relieving perf. shape	Stress-relieving perf. corner	Changes compared to previous model	Objective
S1A	0.8×0.9	0.4×0.5	Straight 18×170 μm^2	90° sharp	N/A		Electrically coupled model	Enable Joule heating
S1B	0.8×0.9	0.4×0.5		9 µm RoC			Rounded perf. corners	Reduce stress in perf. corners
S2A0	0.4×1.24	0.2×0.94		9 µm RoC			Reduced membrane width	Increase buckling load of the membrane
S2A1	0.4×1.24	0.2×0.94		9 µm RoC			Refined heater	Provide uniform heating to the active pumping region
S2A2	0.4×0.45	0.2×0.25		9 µm RoC			Reduced membrane length	Improve process yield
S2A3	0.3×0.45	0.1×0.25		9 µm RoC			Reduced membrane width	Increase buckling load of the membrane; investigate the effect of membrane width on maximum feature stress
S2A4	0.25×0.45	0.1×0.25		9 µm RoC			Reduced membrane width	
S2A5	0.2×0.45	0.1×0.25		9 µm RoC			Reduced membrane width	
S2B	0.4×0.45	0.2×0.25		9 µm RoC	C-shaped	36 µm RoC	Stress-relieving perf.	Reduce stress in perf. corners
S2C	0.4×0.45	0.2×0.25		9 µm RoC	V,W-shaped	9 µm RoC	Stress-relieving perf. in TIZ	Reduce stress in pumping perf. with stress-relieving perf.
S2D	0.4×0.45	0.2×0.25		9 µm RoC	C-shaped	18 µm RoC	Wider RoC in stress-relieving perf. In TIZ	Reduce stress by combining S2B and S2C
S2E	0.4×0.45	0.3×0.35	Dimer	18 µm RoC	N/A		Dimer pumping perf.	Reduce stress with large perf.
S2F	0.4×0.45	0.2×0.25	Straight	9 µm RoC			Beleved membrane	Study effects of different membrane shapes on stress
S2G	0.4×0.45	0.2×0.25	V-shaped	9 µm RoC			Bent pumping perf.	Study effects of bent perf. on stress

Perf. = Perforation
R.T. = Room Temperature
RoC = Radius of Curvature

3.1. Mechanical Refinement for Fabrication Yield

3.1.1. Modeling Improvements

FEA of the Gen S1 4-stage KP discussed in Chapter 2 was conducted by applying the power (0.3 W/stage) into the equivalent model's active pumping region. The equivalent model assumed individual layers (ONONO, metal, etc.) that were composed of air and said material based on the fill factor. For example, the fill factor of handle silicon layer was 50% (30 µm air gap and 30 µm silicon), and thus the thermal properties of the heat sink were equivalent to ≈50% of silicon. While

this approach of modeling provides the overall temperature distribution at a given power level, it neglects the intricate details and temperature nonuniformity across the active pumping region.

In this chapter, the KP components were modeled with accurate feature dimensions and material properties to identify and solve potential issues, and to evaluate the performance more accurately. The heat sink perforations, ONONO perforations, and metal heater traces were modeled after the design layout dimensions. However, the pumping channels, ONONO composite film, and metal heater compositions were modeled based on their equivalent compositions. Due to the complexity, the 10 nm thick Al_2O_3 pumping channels with 1.2 μm wide air gap were modeled as an equivalent medium composted of Al_2O_3 and air. Meanwhile the 5-layer suspended ONONO membrane was modeled as a single layer composite film in order to quantify and compare the feature stress easier. The Cr/Pt metal heater layer was modeled with equivalent mechanical and electrical properties. The structure and material properties assumed in modeling work are shown in Table 3.1. The buried oxide and metal heater layers had specific applied initial stress values such that the results match the measurements. An initial stress of -370 MPa was applied to the buried oxide layer such that the bow of modeled SOI wafer matched the bow measured from the actual SOI wafer. In contrast, the metal heater stress was measured at -517 MPa based on the pre- and post-deposition bow measurements, and thus applied to the metal layer in the model. Negative sign indicates compressive stress whereas positive indicates tensile stress in this work.

3.1.2. Design S1A of the Gen S1 4-stage KP

Composite stress of the suspended membrane is critical for fabrication process yield and operation reliability. The suspended ONONO membrane features, *i.e.,* the perforations that pass vertical gas flow, have high stress accumulation, which could fracture the membrane if it exceeds the fracture strength of the film, which depends on the film quality and fabrication conditions.

Such fractures break the metal connection, effectively breaking the device. This stress value is defined as the maximum feature stress at R.T. (room temperature), which determines the process yield. To avoid such fracture, mild tensile stress of 40-80 MPa is generally used in other work [An15, Ben19].

Table 3.2: Structure Properties assumed in FEA

Structure	Material	Thickness (μm)	Thermal conductivity (W/m*K)	Applied initial stress (MPa)	CTE (ppm/K)
1. Heat sink	Handle silicon	525	130	0	2.6
2. Buried oxide	Buried oxide	0.4	1.4	-370	0.5
3. Device silicon	Device silicon	12	130	0	2.6
4. Pumping channels	Al_2O_3/air	12	0.3-0.4	0	0
5. Dielectric membrane	ONONO	3	20	0	3.95-5
6. Thin film metal heater	Metal	0.125	7.6	-517	8.02

In Design S1A of the 4-stage KP, the ONONO perforations were designed with 90º sharp corners (Fig. 3.1a), where the maximum feature stress at R.T. presumably exceeded the fracture strength. Such high stress concentration cracked the membrane in multiple locations upon release and resulted in a process yield of 0%. To evaluate the ONONO perforation feature stress that can cause such fractures, Design S1A KP with 90º perforation corners were modeled as shown in Fig. 3.1b. The composite ONONO film stress was 186 MPa tensile at room temperature. The result showed a maximum feature stress of 1300 MPa at the primary (outmost) perforation and 790 MPa at the secondary perforation, both of which fractured during/after XeF_2 release. Therefore, the 790 MPa stress concentration of the secondary perforation was identified as the upper boundary of feature stress.

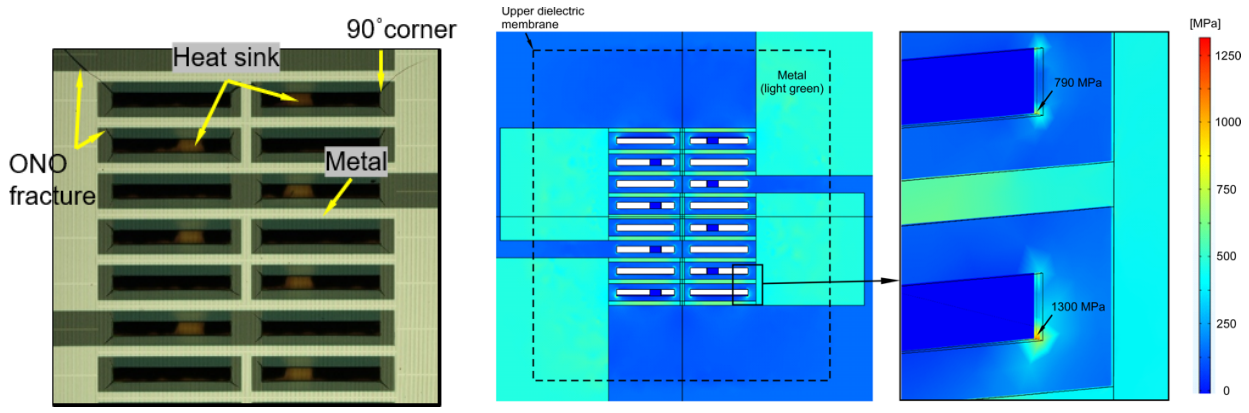

(a) (b)

Fig. 3.1: (a) Design S1A KP with 90º sharp corners and 186 MPa composite stress that resulted in fracture when released. (b) FEA of Design S1A KP at room temperature. The von Mises stress map shows 1300 MPa on the primary and 790 MPa on the secondary perforation corners. Composite film stress is 186 MPa.

3.1.3. Design S1B of the Gen S1 4-stage KP

In Design S1B, the ONONO perforation corners were rounded with a corner radius of 9 µm, such that the corner stress accumulation was lowered. The composite film stress was reduced to 78 MPa by adjusting the coefficient of thermal expansion (CTE) of the ONONO composite film. Other sharp corner features such as metal traces and heat sink perforations were also rounded to avoid potential high stress points. The combination of rounded corner and stress reduction resulted in a successful release of the suspended membrane (Fig. 3.2a) and a process yield of 100% among the released KPs. The Design S1B KP modeling results show a maximum feature stress of 380 MPa (Fig. 3.2b).

Another aspect that determines the reliability of the KP is the minimum feature stress at elevated temperature. If the composite tensile film stress is too low, the thermal stress is reduced at an elevated temperature during the operation. In combination with the metal heater's stress and deflection, the total stress could become compressive and buckle the membrane. This stress value is defined as the minimum feature stress at E.T. (elevated temperature), which determines KP

reliability and performance capability. The E.T. is subject to change depending on the temperature a specific design KP reaches at a given applied power level. As described in Chapter 2, the Design S1B KPs were experimentally evaluated at an applied power of 0.3 W/stage. The electrical connection of the metal heater became open, likely due to the membrane buckling, when the power was increased to 0.375 W/stage. Therefore, 0.3 W/stage was identified as the safe power level. For a longer lifetime and higher operational reliability, the KPs can be operated at power levels lower than <0.3 W/stage. The average temperature of the active pumping area reached 490 K at 0.3 W, according to previous modeling work described in Chapter 2. In this section, this operating temperature of 490 K was then applied to metal traces of the Design S1B KP to analyze the stress level. The result showed that the stress of the ONONO membrane reached -40 MPa (compressive), which was identified as the lower boundary of minimum feature stress for reliable operation (Fig. 3.3). In contrast, at composite stress of 186 MPa, the minimum feature stress of Design S1A KP remained tensile and reached 23 MPa (Fig. 3.4). Table 3.2 contains the summary of stress boundaries in Designs S1A and S1B of the 4-stage KP.

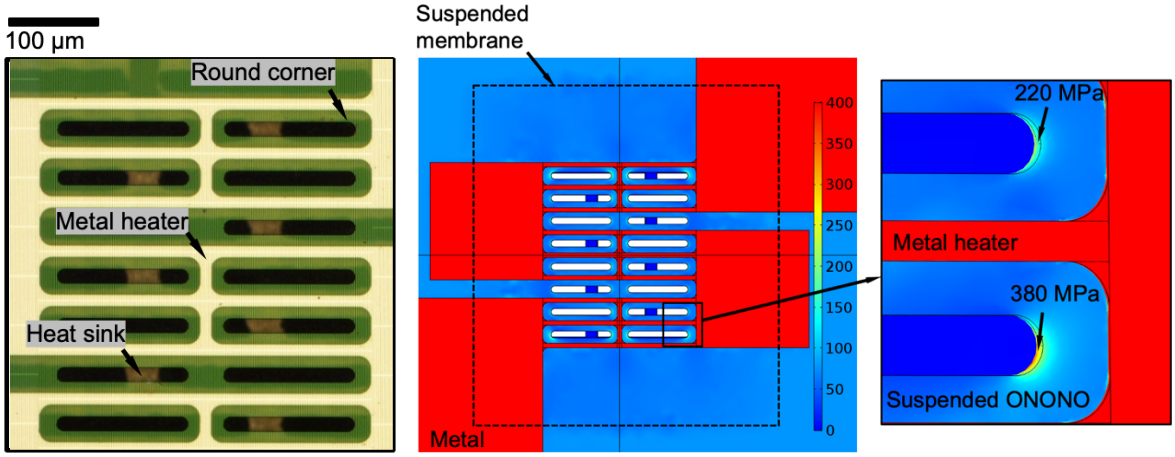

(a) (b)

Fig. 3.2: (a) Fabricated Design S1B KP with round ONONO perforation corners and 78 MPa composite stress that released successfully. (b) FEA of Design S1B KP at room temperature. The von Mises stress map shows a maximum of 380 MPa stress concentration on the perforation corners. Composite film stress 78 MPa.

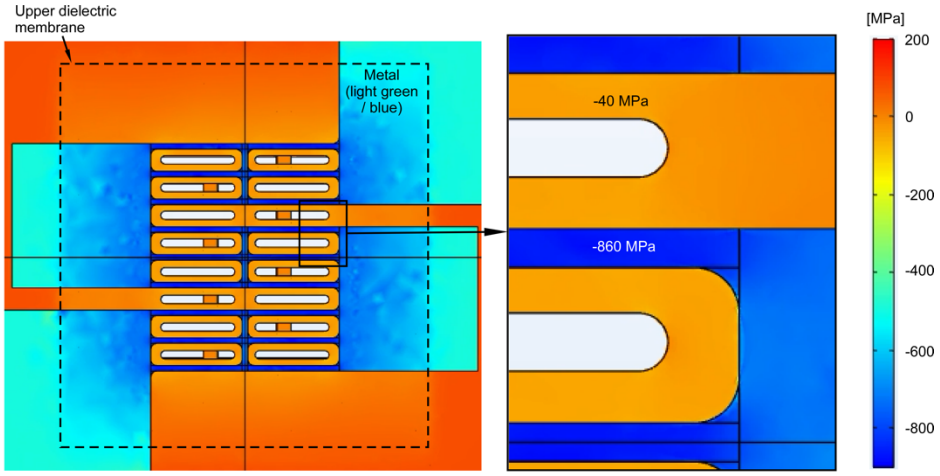

Fig. 3.3: FEA of Design S1B KP at an elevated temperature of 490 K. Stress map shows negative (compressive) stress of the upper dielectric membrane (up to -40 MPa) and metal heater (up to -860 MPa). Composite film stress 78 MPa.

Table 3.3: Composite, maximum, and minimum feature stresses of Design S1A and S1B KPs

Design	O/N/O/N/O thickness composition (μm)	Total thickness (μm)	Composite film stress at R.T. (MPa)	Max. feature stress at R.T. (MPa)	Min. feature stress at E.T. (MPa)
S1A	0.3/1.0/0.4/1.0/0.3	3.0	186	790	23
S1B	0.6/0.55/0.7/0.55/0.6	3.0	78	380	-40

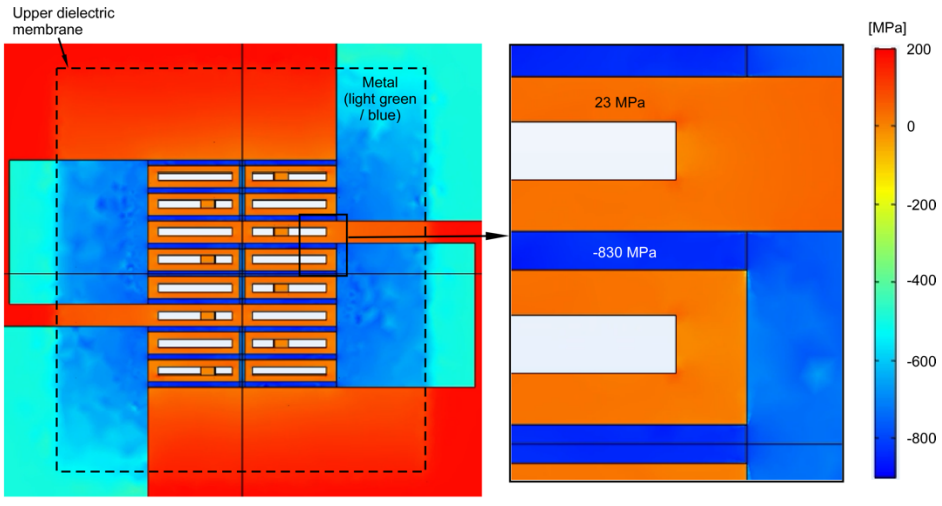

Fig. 3.4: FEA of Design S1A KP at elevated temperature (490 K at 0.3 W). Stress tensor (11 component) map shows negative (compressive) stress of the upper dielectric membrane (up to 23 MPa) and metal heater (up to -830 MPa). Composite film stress 186 MPa.

3.1.3. Mechanical Refinement of the Gen S2 design KP

The objective of a refined KP design is to have tuned stress levels that stay within the upper boundary, which is a maximum feature stress of 790 MP at room temperature, and the lower boundary, which is a minimum feature stress of -40 MPa at elevated temperature. In addition to its compressive stress, buckling of a membrane is attributed to the buckling load $P_{buckling}$ of the structure, which can be estimated as [Wan06, Zie98]:

$$P_{buckling} \sim \frac{EI}{L^2} \tag{3.1}$$

where E is the Young's modulus, I is the second moment of area, and L is the membrane length. For the microfabricated Knudsen pump, L represents the smaller side of the rectangular membrane. By reducing the membrane width, its buckling load can be increased to allow more reliable operation at elevated temperature.

The design changes for mechanical refinement are shown in Fig. 3.5 and Table 3.3. In Design S1B of the Gen S1 4-stage KP, the upper dielectric membrane was 0.8×0.9 mm^2 with an active pumping region of 0.4×0.5 mm^2. The Design S2A0 is the initial design of Gen S2 that explores different parameter changes for mechanical refinement. In Design S2A0, the membrane width is reduced by half, quadrupling its buckling load. In exchange, the membrane length is increased up to 1450 μm such that the overall active pumping region area is comparable to maintain the flow rate necessary for μGC applications. The active pumping region determines the number of parallel pumping channels, and thus the gas flow rate of the KP. Furthermore, the heat sink perforation width and pitch are reduced to 24 and 48 μm, respectively, for more effective cooling on the cold end of the pumping channels. Narrower heat sink perforation also reduces the length of unsupported pumping channel and thus improves robustness. Upper dielectric membrane perforation pitch is reduced to match the heat sink perforation pitch.

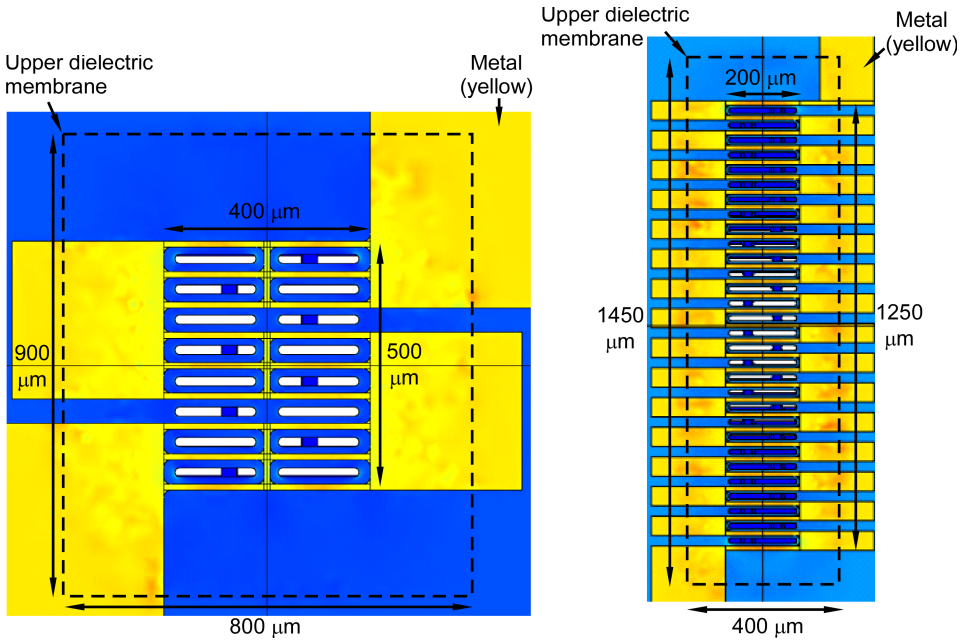

(a) (b)

Fig. 3.5: (a) Design S1B, and (b) Design S2A0 KPs.

Table 3.4: Parameter changes between Design S1B and Design S2A0.

Design	Membrane area (mm^2)	Active pumping region (mm^2)	Thermal isolation region width (μm)	Membrane perforation width / pitch (μm)	Heat sink perforation width / pitch (μm)
S1B	0.8×0.9	0.2 (0.4×0.5)	200	18 / 60	30 / 60
S2A0	0.4×1.45	0.25 (0.2×1.25)	100	18 / 48	24 / 48

The membrane width reduction is limited by the active pumping region and thermal isolation region. The thermal isolation region impacts the hot end temperature and power loss. The effect of membrane width and length adjustments on the maximum feature stress and temperature distribution are studied further in Group A designs, as shown in Fig. 3.6.

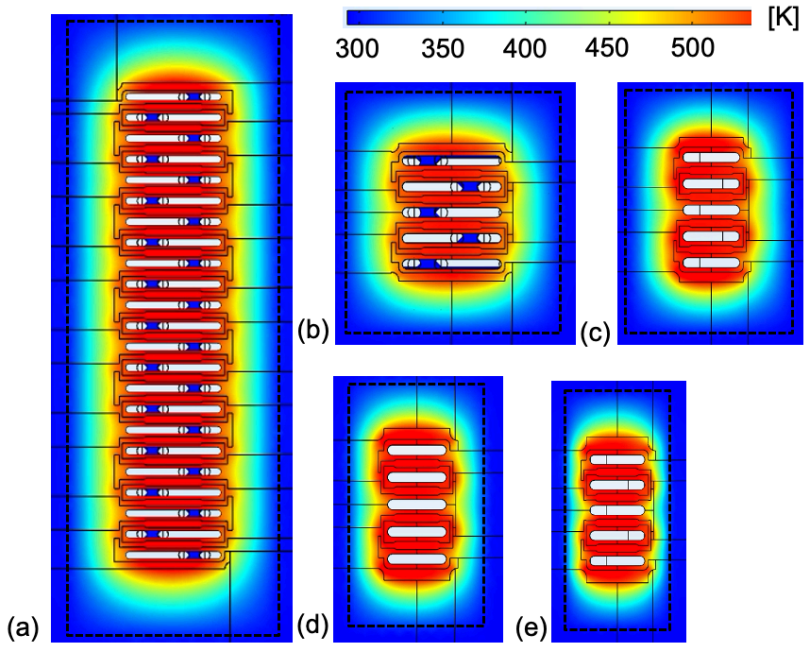

Fig. 3.6: Group A designs with different membrane size. The metal heater layout is refined for uniform temperature distribution across the active pumping region and thermal isolation region. (a) Design S2A1 with 0.4×1.24 mm^2, (b) Design S2A2 with 0.4×0.45 mm^2, (c) Design S2A3 with 0.3×0.45 mm^2, (d) Design S2A4 with 0.25×0.45 mm^2, and (e) Design S2A5 with 0.2×0.45 mm^2 membrane. Membranes are illustrated in dashed boxes.

Group A is a group of KP designs with straight ONONO perforations and varying membrane size. The corners were rounded with 9 µm radius of curvature, which is half of 18 µm perforation width for smooth, rounded corners. There is a tradeoff between reliability and performance depending on the perforation width. The FEA showed that a wider perforation with wider radius of curvature had lower maximum feature stress due to its longer perimeter and less stress concentration. However, wider perforation results in deeper pumping channels (in *y* direction). As described in Chapter 2, with heat generating only from the metal traces on top of ONONO, temperature of the center of the deep (in *y* direction) pumping channels would drop such that it could hinder the KP's performance. Therefore, in this group of designs, 18 µm wide perforation was chosen. With straight, 18 µm wide perforations, the membrane size and layout were analyzed. The designs shown in Fig. 3.6b and Fig. 3.7 were refined with 0.4×0.45 mm^2 membrane and

maximum feature stress of 275 MPa. The tension on the primary perforations generated ≈56 nm of deformation, as shown in Fig. 3.7b with 100× exaggerated displacement. Metal layout had no significant impact on the maximum feature stress. The distance between the metal and ONONO features were determined based on the fabrication tolerance. The simulation details and temperature uniformity are discussed in the following section. Further reducing the membrane size would result in insufficient number of pumping channels and thus flow rate.

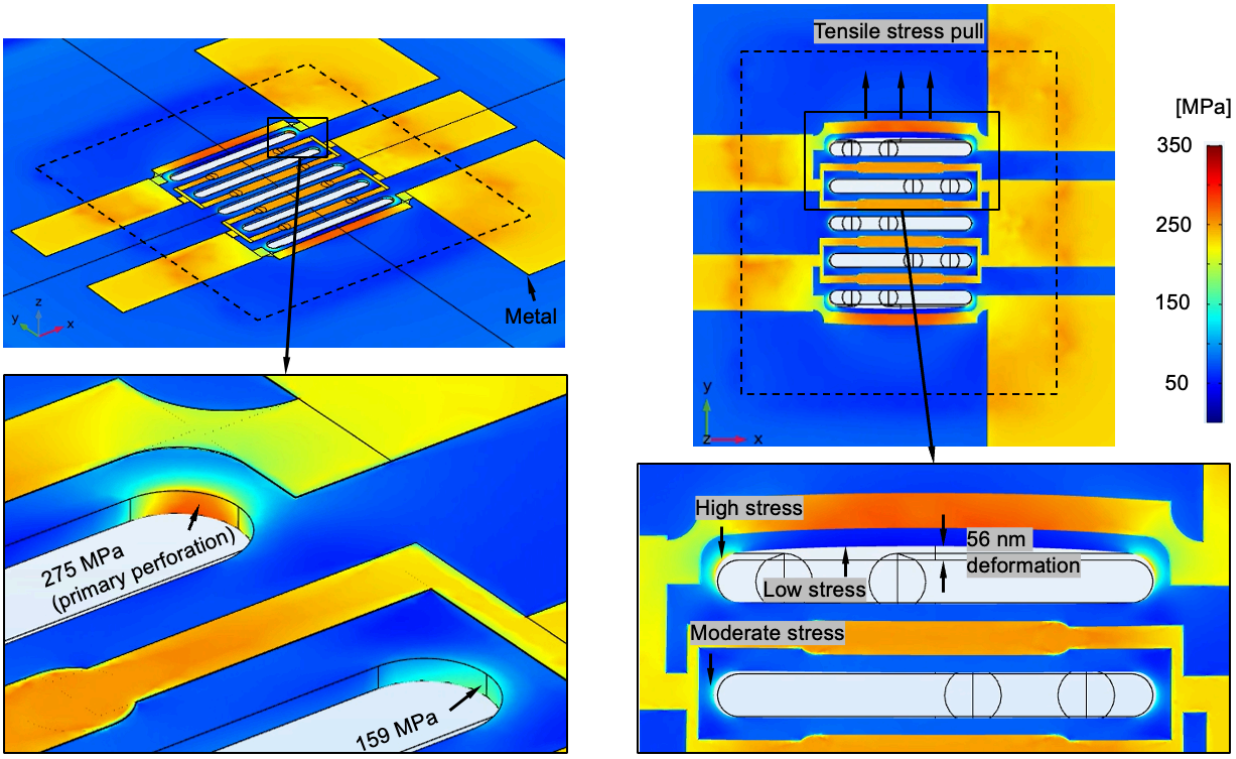

(a) (b)

Fig. 3.7: (a) Stress map of Design S2A2 KP with 18 µm wide, straight membrane perforations. The primary perforations have a maximum feature stress of 275 MPa. (b) Design S2A2 KP with 100× exaggerated displacement, showing 56 nm deformation in the primary perforation.

Table 3.5: Comparison of Group A potential designs with reduced upper dielectric membrane size. Composite ONONO film stress ≈80 MPa.

Design	S1B	S2A1	S2A2	S2A3	S2A4	S2A5
Membrane area (mm^2)	0.8×0.9	0.4×1.24	0.4×0.45	0.3×0.45	0.25×0.45	0.2×0.45
Active pumping region (mm^2)	0.4×0.5	0.2×0.94	0.2×0.25	0.1×0.25	0.1×0.25	0.1×0.25
Resistance (Ω)	100	664	230	161.7	155.5	148.4
Input power (W)	0.36	0.6	0.25	0.148	0.161	0.196
ΔT (K)	101	103	100	100	102	102
Max. feature stress at R.T. (MPa)	380	292	275	269	267	270

A significant reduction in maximum feature stress is observed between Design S1B and S2A1 when the membrane width was halved, although the membrane length was increased by ≈40%. With half the membrane width and 23% less maximum feature stress, Design S2A1 could provide high performance with improved reliability compared to the Gen S1. With 3× reduced membrane length and 9% reduced maximum feature stress compared to Design S2A1, Design S2A2 could provide improved process yield and reliability. Following Design S2A2, no significant change in maximum feature stress was observed, including when the width was reduced by up to 2× in S2A4.

FEA of Design S2A1, with composite stress of 140 MPa, showed the maximum and minimum feature stresses of 500 MPa and -10 MPa, respectively. The maximum feature stress of Design S2A1 is presumed acceptable, with safety margin of 290 MPa from the maximum feature stress of Design S1A. The minimum feature stress has improved substantially, from -40 MPa to -10 MPa, based on the increase in composite stress. Furthermore, Designs S2A1 and S2A2 were evaluated at 80 MPa composite stress for additional safety. Results showed lower minimum feature stress at elevated temperature due to the lower composite film stress. However, in combination with the 4× increased buckling load, the elevated temperature KP operation could potentially be safe. The tradeoff between the maximum and minimum feature stress depends on the composite film stress.

Table 3.6: Composite stress and feature stresses of Design S1 and Design S2A KPs.

Design	Upper dielectric membrane (mm^2)	Active pumping area (mm^2)	Composite film stress at R.T. (MPa)	Max. feature stress at R.T. (MPa)	Min. feature stress at E.T. (MPa)
S1A	0.8×0.9	0.4×0.5	186	790	23
S1B	0.8×0.9	0.4×0.5	78	380	-40
S2A1	0.4×1.24	0.2×0.94	140	500	-10
			80	292	-63
S2A2	0.4×0.45	0.2×0.25	140	475	-10
			80	275	-46

The Design S2A1 is chosen as a candidate (Gen S2A) for fabrication in Chapter 4 whereas the Design S2A2 is further analyzed for mechanical refinement. The maximum feature stress at R.T. can be reduced by refining the KP design, which can allow increase in the composite film stress and provide safety margin in the minimum feature stress. The FEA showed that, in addition to the composite film stress, the maximum feature stress depends on variables such as the location, shape, and width (*i.e.*, radius of curvature) of the perforations. Therefore, the Design S2A2 is modified into six groups of designs (B-G) with different suspended ONONO membrane perforations to analyze the impact on maximum feature stress. The results are summarized in Fig. 3.8 and Table 3.6.

Group B is a group of designs with C-shaped primary perforations within the active pumping region (Fig. 3.8b). Reduction in stress concentration was observed when the stress concentration region, *i.e.,* the perforation corner perimeter, is expanded in Design S1B compared to Design S1A. Therefore, in Group B designs, the corner radius of curvature was expanded from 9 μm up to 36 μm. The maximum feature stress reduced to 189 MPa as the perimeter of the stress concentrated corner increased 4×. The metal heater layout was modified accordingly to provide uniform heating across the active pumping region. The expansion of the corners was limited by the depth of pumping channels within the perforation corners because the middle of the pumping channels (in *y* direction) would experience temperature drop. The temperature distribution across the active

pumping region and primary perforation corners were analyzed as shown in Fig. 3.9. The average $T_{h.p.open}$ reached ≈320 K at the center of the widened primary perforation corners compared to the average $T_{h.p.open}$ of ≈467 K at the three perforations in the middle of the KP. The drastic temperature drop in $T_{h.p.open}$ at the center was caused by a combination of lack of heating from the sides. The cold regions inside the 72 μm wide corners were overlapped with the heat sink, which blocks potential backward gas flow (Fig. 3.9). Excluding the blocked regions at the center of the corners, ΔT across the primary perforation pumping channels was 73 K compared to 97 K across the middle perforation pumping channels, with an overall average ΔT of 84.9 K. Compared to the temperature variation of the Gen S1 KP, discussed in the following section, Group B design has significant improvement in both the temperature variation and maximum feature stress.

Group C consists of various designs with additional 18 μm wide, stress-relieving perforations in the thermal isolation region (Fig. 3.8c). Given that the highest stress concentration was observed in the outmost, primary perforations, additional perforations were added to shift the stress concentration away from the pumping perforations. The additional perforations were modeled at different bending angles and at different locations within the thermal isolation region. The types of additional perforations include straight (same as the pumping perforations), single-bent (V-shaped), and double-bent (W-shaped). The maximum feature stress shifted to the new outmost primary perforations, *i.e.*, the additional perforations, due to their locations being closer to the membrane edge. Owing to its reduced distance from the membrane edge (in y direction) and thus the tension, the maximum feature stress of the primary perforations reduced to 185 MPa. The tradeoff for the lower maximum feature stress was inadequate heating of the channels within the additional perforations created in the thermal isolation region. At high pressure head operations, these lower temperature channels in the thermal isolation region could leak the gas flow backward.

For this group of designs to be viable, the heat sink needs to be designed such that it blocks off the potential backward gas flow.

Group D is a group of designs with C-shaped additional perforations in the thermal isolation region (Fig. 3.8d). To combine the improvements observed in Group B and C designs, the stress-relieving perforations in the thermal isolation region of Group C were modified to C-shaped perforations of Group B with wide corners. The locations with respect to the membrane edge, directions (upward-facing ∪ or downward-facing ∩), and widths of the perforations were varied to achieve a low maximum feature stress. Owing to its proximity to the membrane edge and widened corners, the maximum feature stress of the corners reached as low as 165 MPa, which was lower than Group B or C designs. However, similar to Group C, the inadequately heated additional perforations could leak the gas flow backward.

Based on the improvements observed in maximum feature stress using widened circular corners, KP designs with wider circular perforations were studied in Group E (Fig. 3.8e). Perforations with up to 18 μm radius were analyzed by modifying the overall layout. The lowest maximum feature stress observed was 158 MPa, which was the lowest among the seven groups of designs studied. However, the performance of this KP deteriorated because of the loss in ΔT. Compared to ΔT of 97 K in Group A design, Group E design KP had ΔT of 77 K. This performance tradeoff and circular perforation based KPs could be of interest for further investigation.

Group C and D modeling results suggest that perforations closer to the membrane edge have lower maximum feature stress likely due to the reduced tension on the perforations. In fact, reducing the membrane length (in y direction) of Group A and B designs reduced the maximum feature stress down to <200 MPa. However, reducing the thermal isolation region width causes power loss and inadequate heating of the pumping channels in primary perforations. In Group F

designs, the suspended membrane corners were beveled to create the effect of reduced tension on the perforations while preserving the thermal isolation region width. With 400 µm wide membrane, the bevel angle was varied from 15º to 75º. The design shown in Figure 3.8f has a bevel angle of 45º with 150 µm on both sides of the beveled triangle, which leaves 100 µm on top and bottom sides of the membrane and 150 µm on right and left sides. The lowest maximum feature stress recorded was 267 MPa, compared to 275 MPa of Group A design, suggesting that beveling the membrane corners does not impact tension on the features significantly.

In Group G designs, the 18 µm wide ONONO perforations were bent in V-shape to observe the impact on the maximum feature stress (Fig. 3.8g). In Group C designs, bent additional perforations had lower stress accumulation compared to the straight perforations likely due to the reduced distance and pulling from the membrane edge. In Group G, the perforations were bent from 5º to 30º angle while maintaining the perforation length (in *x* direction) at 175 µm. The metal heater layout was modified accordingly. The lowest maximum feature stress recorded was 300 MPa, suggesting that bent perforations at the center of the membrane does not reduce the maximum feature stress.

Table 3.7: Modeling results summary of Design S2 groups of KPs.

Design		Pumping ONONO perforation			Stress-relieving ONONO perforation				Max. feature stress at R.T. (MPa)
		# of perfo-rations (µm)	Center width (µm)	Corner radius of curv. (µm)	# of perfo-rations (µm)	Center width (µm)	Corner radius of curv. (µm)	Location	
S1A		16	18	90° sharp	N/A				790
S1B		16	18	9					380
S2A1		23	18	9					292
Design S2 groups	B	3	18	9	2	18	36	A.P.R.	189
	C	5	18	9	2	18	9	T.I.R.	185
	D	5	18	9	2	9	18	T.I.R.	165
	E	20	36	18	N/A				158
	F	5	18	9					267
	G	5	18	9					300

T.I.R. = Thermal Isolation Region
A.P.R. = Active Pumping Region

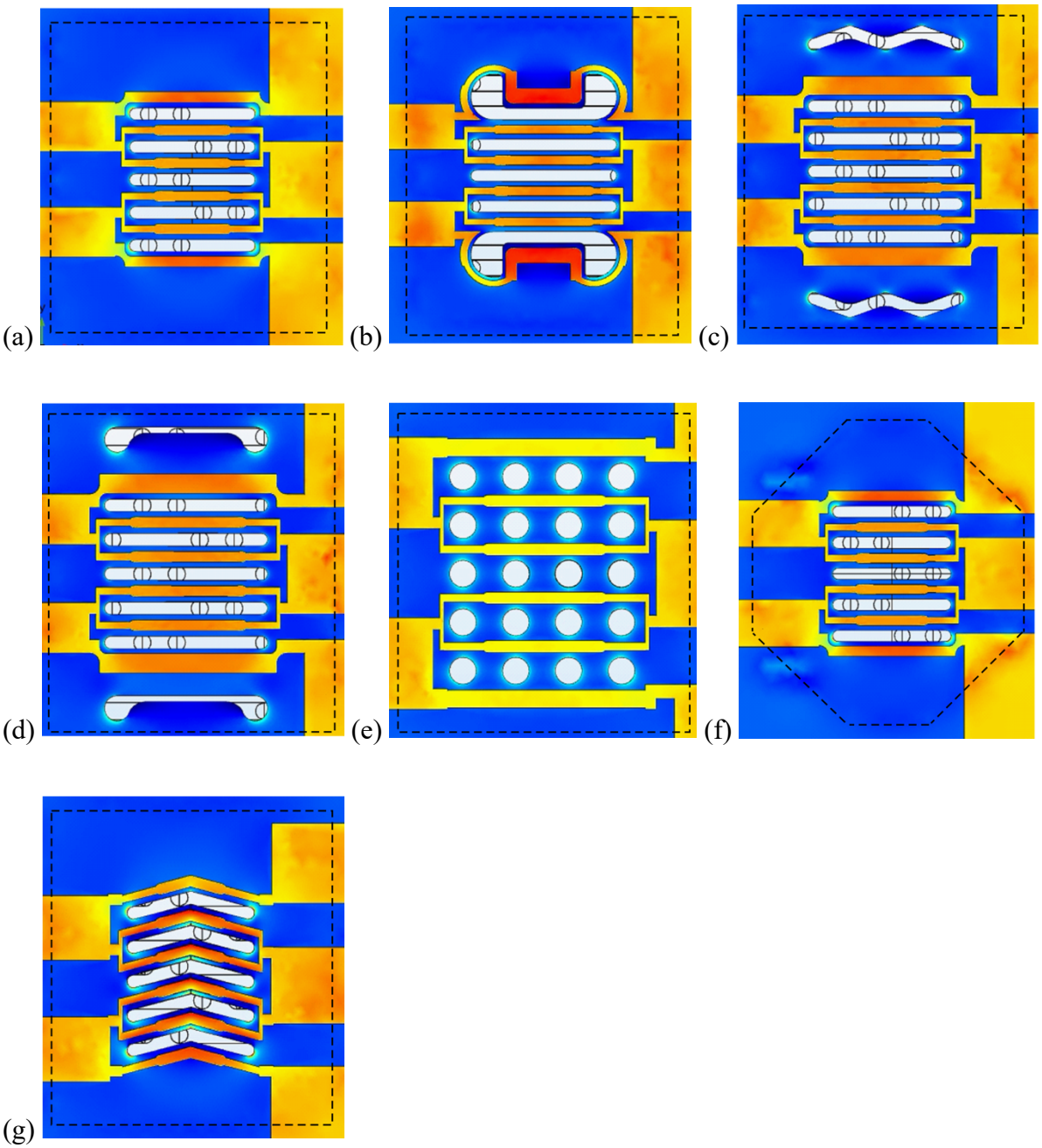

Fig. 3.8: (a) Design S2A2 with 18 µm wide, straight perforations, (b) Group B design with C-shaped primary perforations in the active pumping region, (c) Group C design with additional primary perforations in the thermal isolation region, (d) Group D design with C-shaped additional primary perforations in the thermal isolation region, (e) Group E design with circular perforations with 36 µm diameter, (f) Group F design with beveled membrane corners, and (g) Group G with bent perforations.

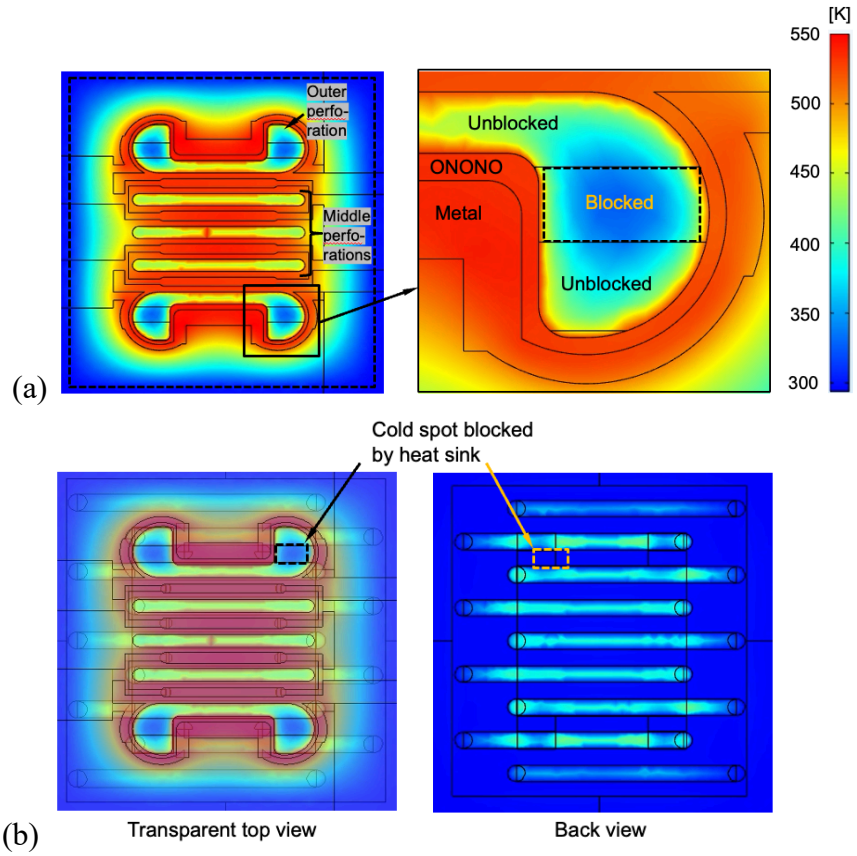

Fig. 3.9: Temperature distribution in Group B design. (a) Non-transparent top view, and (b) transparent top view and back view. The cold spot at the center of the C-shaped primary perforation is blocked by the heat sink from the backside to avoid a potential backward gas flow.

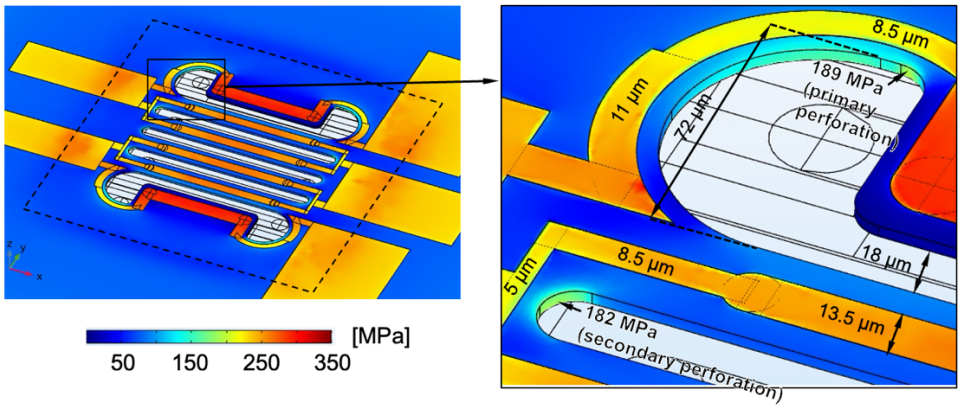

Fig. 3.10: Stress map of the Group B design with C-shaped primary perforations with a radius of curvature of 36 µm.

In summary, various KP membrane designs were analyzed with different perforations and dimensions, categorized in seven groups. The most significant stress reduction was due to the wider the perforation corners with increased perimeter length. In Group B, D, and E designs with widened corners, the maximum feature stress was reduced to 165-189 MPa. Proximity to the membrane edge reduced tension on the perforations and thus the maximum feature stress. Group C design had maximum feature stress of 185 MPa. In combination with the widened corners, Group D design had maximum feature stress of 165 MPa. However, the additional perforations within the thermal isolation region near membrane edge have lower $T_{h.p}$, which could leak backward gas flow. Therefore, in addition to the Gen S2A, Group B design was chosen for fabrication as the Gen S2B KP and further analyzed for temperature uniformity (Fig. 3.9).

3.2. Thermal Refinement for More Uniform Heating

3.2.1. Electrically and Thermally Coupled Model

The performance of the KP depends on the temperature difference ΔT along the pumping channels. Therefore, thermal refinement of the redesigned models is necessary to achieve high performance. To model the temperature distribution across the KP as close to reality as possible, the *Solid Mechanics* models were electrically and thermally coupled such that the input power can be electrically applied to the metal heater terminals with input voltage and induce electric current through the resistive heater. The metal properties were calculated based on the measurements of the Gen S1 4-stage KP, described in Chapter 2, and applied to the refined models (Table 3.7). Figure 3.11 shows the temperature distribution across the temperature-based and electrically coupled KP models. The temperature-based model (Fig. 3.11a) consists of two physics; *Solid Mechanics* and *Heat Transfer in Solids.* As described in previous section, the elevated temperature

of 490 K, acquired from the equivalent model with an applied power of 0.3 W, was applied to the high-resistance metal traces to evaluate the active pumping region's temperature. The electrically coupled model (Fig. 3.11b) consists of three physics; *Solid Mechanics, Heat Transfer in Solids,* and *Electric Currents*. The addition of *Electric Currents* allows the application of electric voltage at the metal heater terminals. Coupled with the *Heat Transfer in Solids,* it generates more realistic heating of the active pumping region via Joule heating.

In Fig. 3.11b, a total power of 0.308 W was applied via an input voltage of 5.85 V and induced current of 52.6 mA. The Joule heating of the KP reached a maximum 535 K, localized at the center of the active pumping region. This modeling result revealed an inadequate, nonuniform heating of the pumping channels, which would result in nonuniform performance of the channels. In particular, the pressure head generated by the high temperature channels ($T_{h.p.} \approx 535$ K) at the center exceeds the pressure head generated by the lower temperature channels ($T_{h.p.} \approx 390$ K) near the thermal isolation region. At high pressure head operations, if flow resistance of the load is higher than flow resistance of the lower temperature pumping channels, those lower temperature pumping channels could leak the gas pumped by the higher temperature pumping channels backward.

Table 3.8: Relevant parameters of equivalent metal heater.

Reference resistivity	2.39×10^{-7} Ω·m
Temperature coef. of resistivity	3.7×10^{-3} K^{-1}
Coef. of thermal expansion	8.02×10^{-6} K^{-1}
Thickness	125 nm

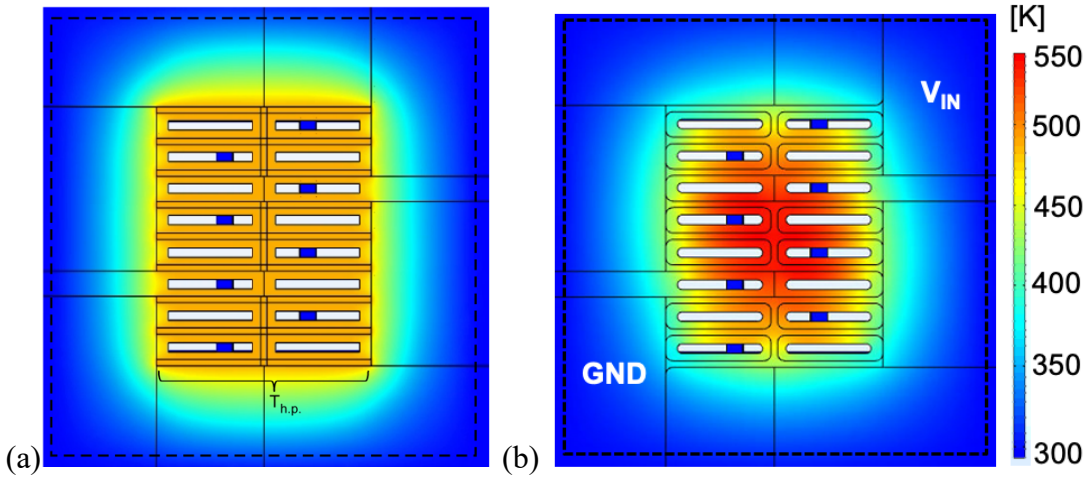

Fig. 3.11: (a) Temperature-based model of Design S1A KP with $T_{h.p.}$ of 490 K applied to the metal traces. (b) Electrically and thermally coupled model of Design S1B KP with Joule heating induced by an input voltage.

3.2.2. Metal Heater Layout Improvement for More Uniform Temperature Distribution

Upon learning the nonuniform, localized heating of the active pumping region (Fig. 3.11a) with the electrically coupled model, the temperature distributions of Gen S2A and S2B KP models were analyzed to improve the temperature uniformity of the active pumping region. As illustrated in Fig 3.6a and 3.9a, the metal heater layouts were designed such that they provide uniform heating to the pumping channels. The width of each metal trace was adjusted to provide uniform heat along the trace. For example, the width of the metal trace near the thermal isolation region, which requires more heating due to the lateral heat loss, is 5 µm whereas the trace at the center of the suspended active pumping region is 13.5 µm (Fig. 3.10). As a result, the lateral variation in the hot-side temperature $T_{h.p}$ reduced from 145 K in the Gen S1B 4-stage KP to 55 K in the Gen S2A and S2B KPs, which utilizes the pumping channels more effectively.

3.2.3. Electrical Layout of 5-Stage KPs

The Gen S2A and S2B designs were implemented into 5-stage KPs as shown in Fig. 3.12. The pumping stages and through-holes are packed densely while maintaining the thermal isolation

between the stages. The overall chip design is identical with 5.4×7.8 mm^2 footprint, five pumping stages, five sets of through-holes for gas flow routing, two alignment marks for bonding with the glass dies, and 1.7×2 mm^2 contact pads. The pumping stages are connected in series fluidically such that the blocking pressure scales stage-to-stage while maintaining the flow rate. A single pumping stage consists of one Gen S2A KP with 0.4×1.25 mm^2 membrane area or two Gen S2B KPs with 0.4×0.45 mm^2 membrane area, 0.29 mm apart. The chip size, layout, and the number of pumping stages were determined to accommodate the fabrication limitation.

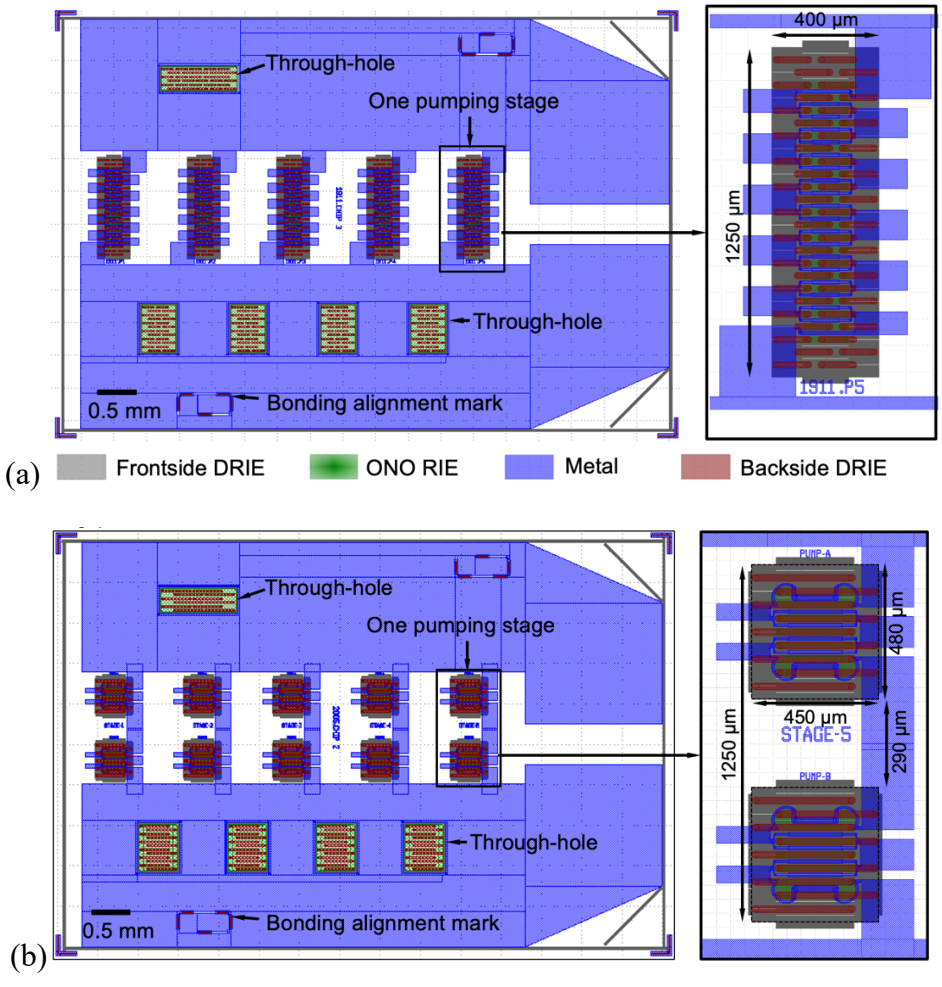

Fig. 3.12: (a) Gen S2A – 5-stage KP layout. (b) Gen S2B – 5-stage KP layout.

The chip-level metal layout of the 5-stage KP was refined to reduce parasitic resistance, which causes low efficiency and power maldistribution between stages. The multi-stage KPs were designed in parallel electrically such that the remaining pumping stages are functional even if some of the pumping stages fail. However, the parallel arrangement causes power maldistribution between the stages due to the parasitic electrical resistance of the stage-to-stage connection area. Furthermore, the effective electrical resistance of the parallel pumps is reduced compared to electrical resistance of an individual pump, which can result in low efficiency. In the 4-stage KP described in Chapter 2, the efficiency, defined as the electrical resistance of the pumping stages per total electrical resistance, was 76%. The parasitic electrical resistance also caused a maximum of 64% difference in power distribution among the pumping stages. The power maldistribution translates to underperformance of the KP. The total applied power is limited by the overpowered pumping stage. Meanwhile the underpowered pumping stage underperforms due to the lack of power it can receive. In this 5-stage KP design, the efficiency and maximum applied power difference between stages were reduced to 94.4% and 9.9%, respectively.

Based on the FEA results, the performance of the 5-stage Gen S2A and S2B KPs were calculated as shown in Table 3.8. At a maximum $T_{h,p}$ of 550 K, which was established as the maximum temperature based on the Gen S1 KP work, ΔT of Gen S2A and S2B KPs reached 103 and 87 K at W_p of 0.6 and 0.82 W/stage, respectively. The ΔT of Gen S2B KP was lower due to the large radius of curvature at the stress-relieving ONONO perforations (Fig. 3.9). Therefore, ΔP_{eq} was ≈16% lower for the Gen S2B KP, proportional to its ΔT value. In addition to the lower ΔT, the Gen S2B KP have fewer number of parallel pumping channels compared to the Gen S2A KP, which resulted in ≈30% lower Q_{max}. The Gen S2B KPs are expected to provide higher

fabrication yield and more reliability because of their smaller membrane size and maximum feature stress at R.T.

Table 3.9: Performance of the 5-stage and 30-stage Gen S2A and S2B KPs

Gen	# of pumping stages	# of pumps per stage	W_p (W)	ΔT (K)	ΔP_{eq} (kPa)	Q_{max} (sccm)	Membrane area (mm^2)	Max. feature stress at R.T. (MPa)
S1B	4	1	1.2 (0.3/stage)	84	3.3 (0.83/stage)	0.75 (0.75/stage)	0.8×0.9	380
S2A	5	1	3.0 (0.6/stage)	103	3.85 (0.77/stage)	1.5 (1.5/stage)	0.4×1.25	292
	30	1	18.0 (0.6/stage)		23.1 (0.77/stage)			
	1	30			0.77	45		
S2B	5	1	4.1 (0.82/stage)	87	3.25 (0.65/stage)	1.06 (1.06/stage)	0.4×0.45	189
	30	2	24.6 (0.82/stage)		19.5 (0.65/stage)			
	1	60			0.65	31.8		

3.3. Scalable Multi-Stage Knudsen Pump Design

The GCA AS200 AutoStep exposure system at the Lurie Nanofabrication facility cleanroom is capable of exposing 1-µm features at an area intersected by a 18×18 mm^2 square and a ⌀19 mm circle. The overall die size is limited by an area intersected by a 20×20 mm^2 square and a ⌀21 mm circle. Therefore, the KP design in this work is confined to a die with a footprint of 17.3×20.3 mm^2 where the 1.2-µm wide pumping channels are confined to the 1-µm exposure region, as shown in Fig. 3.13.

The die consists of six 5-stage KPs (Chip 1-6), a flow meter (Chip 7), a 1-stage test KP (Chip 8), and a thermistor (Chip 9) as listed in Table 3.9. The SOI die layout is designed such that the 5-stage KPs can be scaled into 10-, 15-, 20-, or 30-stage KP. For example, if diced together, Chips 1&2, Chips 3&4, or Chips 5&6 can form 10-stage KPs. Without dicing, the die can function as a 30-stage KP with a monolithic flow meter near the gas inlet port and a thermistor for temperature feedback. The fluidic routing through the grooves in the frontside and backside glass dies can be

scaled with the SOI die. Figure 3.13 shows a series fluidic connection of the 30-stage KP. The grooves in the glass die can be modified into one large groove, in addition to the gas inlet and outlet ports, such that the pumping stages are in parallel fluidic connection to achieve a high flow rate.

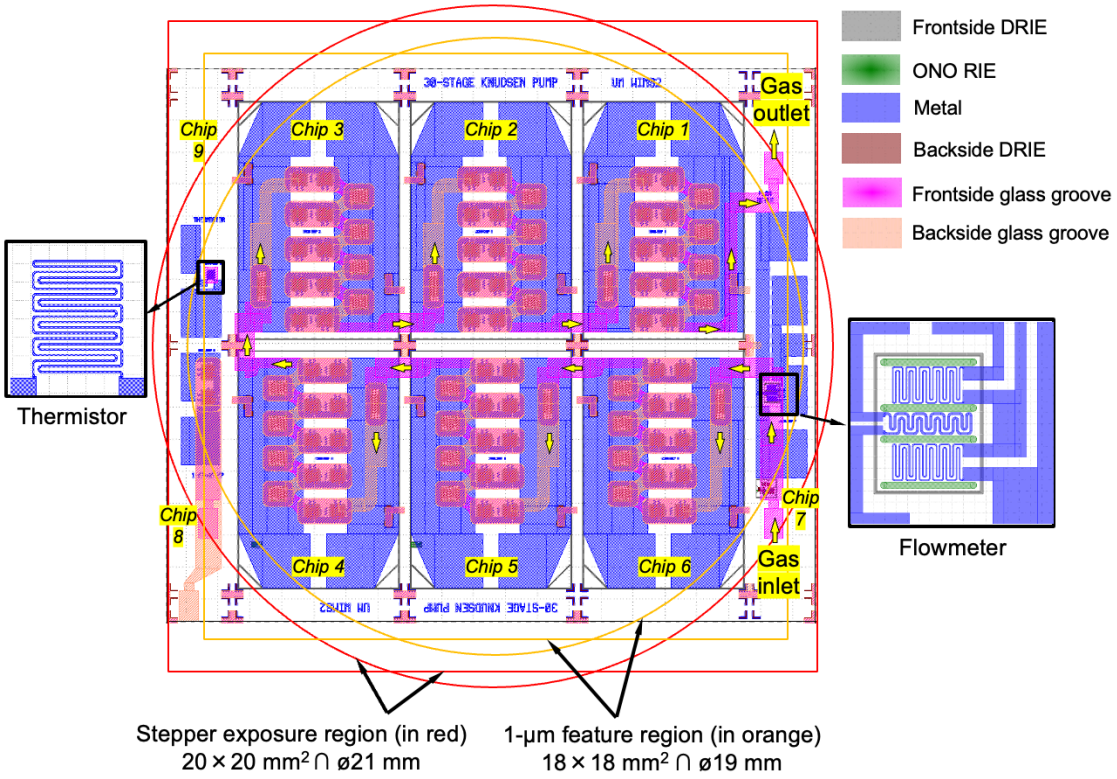

Fig. 3.13: Layout of the Gen S2B – 30-stage KP with monolithic flow meter and thermistor.

Table 3.10: Content of the die-level layout

Chip #	Dimension (mm²)	Functionality
1-6	5.4×7.8	5-stage KP
7	2.05×15.6	Flow meter
8	2.05×7.8	1-stage test KP
9	2.05×7.8	Thermistor
Die	17.3×20.3	30-stage KP

The blocking pressure and maximum flow rate of the scaled KPs are listed in Table 3.8. In series connection, the blocking pressure of the 30-stage Gen S2A and S2B KPs can scale up to ≈20 kPa. In parallel connection, the pumping stages that consist of 30 or 60 parallel pumps can achieve a maximum flow rate of 45 and 32 sccm for S2A and S2B, respectively. However, as the average pressure P_{avg} along the pumping channel drops with each pumping stage, the KP's performance is expected to drop due to the increased mean free path [Sha99]. Such scaling could provide the target performance for specific applications without wasting power or overshooting in either metric, *e.g.,* applying up to 18 W power to achieve the maximum flow rate of 1.5 sccm when the 30-stage KP is in series configuration.

3.4. Conclusion

In summary, this chapter investigates various KP design for mechanical and thermal refinement through FEA modeling. The models are improved with more accurate feature dimensions and material properties to reflect reality more closely. The KP designs are mechanically refined by reducing the maximum feature stress at room temperature and increasing the minimum feature stress at elevated temperature to avoid cracking and buckling of the membrane, respectively. To further increase the mechanical reliability, the membrane widths of the refined KPs are reduced 2×, which theoretically increases the buckling load 4×, compared to the 4-stage KP described in Chapter 2. The metal heater layout is refined to provide more uniform heating within the active pumping region and more even power distribution amongst the multiple pumping stages.

The Gen S2A is a KP with reduced membrane width (0.4×1.24 mm^2) and lower maximum feature stress compared to the Gen S1 4-stage KP in Chapter 2. The 5-stage Gen S2A KP is

calculated to provide a blocking pressure of 3.85 kPa and a maximum flow rate of 1.5 sccm at an applied power of 3 W. In addition to the membrane width, the membrane length (0.4×0.45 mm^2) of Gen S2B KP is reduced for higher process yield. Two small-membrane KPs are implemented as a pumping stage in the 5-stage Gen S2B KP, which is calculated to provide a blocking pressure of 3.3 kPa and a maximum flow rate of 1.06 sccm at an applied power of 4.1 W. The 5-stage KP designs can be scaled up to 30-stage KP, which can theoretically provide a blocking pressure of ≈20 kPa and a maximum flow rate of ≈1 sccm at an applied power of 20 W.

Chapter 4:

Gen S2: Blocking Pressure Enhancement in Suspended Monolithic 5-Stage Knudsen Pump

4.1. Introduction

This chapter describes a method of enhancing the blocking pressure of suspended through-wafer SOI KPs. Previously reported through-wafer KP generates high flow rates by incorporating numerous micromachined pumping channels through the device silicon layer, micromachined heat sinking fins in the handle layer, and thin film metal heaters on the upper surface (Fig. 4.1a) [An14, An15]. The SOI through-wafer KP provides higher and more predictable flow rates than other KPs that employ porous media to provide the pumping channels [Gup08, Mut17, Nak16, Pha10].

Cascading multiple pumping stages can scale up the blocking pressure, but this approach also requires proportional increase in the power consumption [An13], which may not be acceptable for some applications. In contrast, improving the blocking pressure per pumping stage requires improving the pumping channel geometry. As derived from the mass flow rate equation, the blocking pressure, ΔP_{eq}, is proportional to the temperature difference across the length of the pumping channel, ΔT, the thermal creep flow coefficient, q_T, and the inverse of the viscous flow coefficient, q_P (Fig. 4.1a) [Sha99]. The q_T and q_P are dependent on the hydraulic diameter of the channel and have been tabulated [Sha99]. Reducing the pumping channel width, *a,* reduces the hydraulic diameter of the channel and effectively increases q_T and decreases q_P. For a given type of channel sidewall, larger channel length *l* increases the thermal isolation between the hot and

cold ends, hence provides larger ΔT at a given applied power. Therefore, one way to improve the blocking pressure per pumping stage is to use long and narrow pumping channels.

The impact of pumping channel geometry and thermal conductance on ΔP_{eq} is evident in previously reported SOI through-wafer KPs. For example, an early version KP that used pumping channel sidewalls made from 0.1 μm thick silicon oxide-nitride-oxide achieved ΔP_{eq} of 0.27 kPa [An14], whereas a later version reduced the thermal conductance by using 10 nm thick Al2O3 sidewalls and achieved ΔP_{eq} of 0.4 kPa [An15]. Compared to these single-stage KPs with 2 μm wide pumping channels, the Gen S1 KP with four pumping stages and 1.2 μm wide pumping channels improved ΔP_{eq} by an order of magnitude to 3.3 kPa.

This chapter reports the enhancement of blocking pressure of SOI through-wafer KP by increasing the l. Further increases are obtained by cascading multiple stages.

4.2. Design and Modeling

In this work the substrate SOI has 25/1/400 μm thick device/buried oxide/handle layers. As determined by the device layer thickness, the value of l is 25 μm (Fig. 4.1a). The handle layer thickness is selected as a compromise between the ease of micromachining the heat sink underneath the pumping channels and providing mechanical robustness for the overall device. The pumping channels are a=1.2 μm wide in x direction with b=18 μm wide openings in y direction, resulting in an effective hydraulic diameter of ≈1.2 μm. The pumping channel sidewalls are made of 10 nm thick Al_2O_3, which provides low thermal conductance and adequate mechanical robustness. On the top surface of the wafer, a composite dielectric membrane made of 3 μm thick silicon oxide and nitride supports a 25/100 nm thick Cr/Pt metal heater. The thicknesses are selected for mechanical robustness and an appropriate electrical resistance.

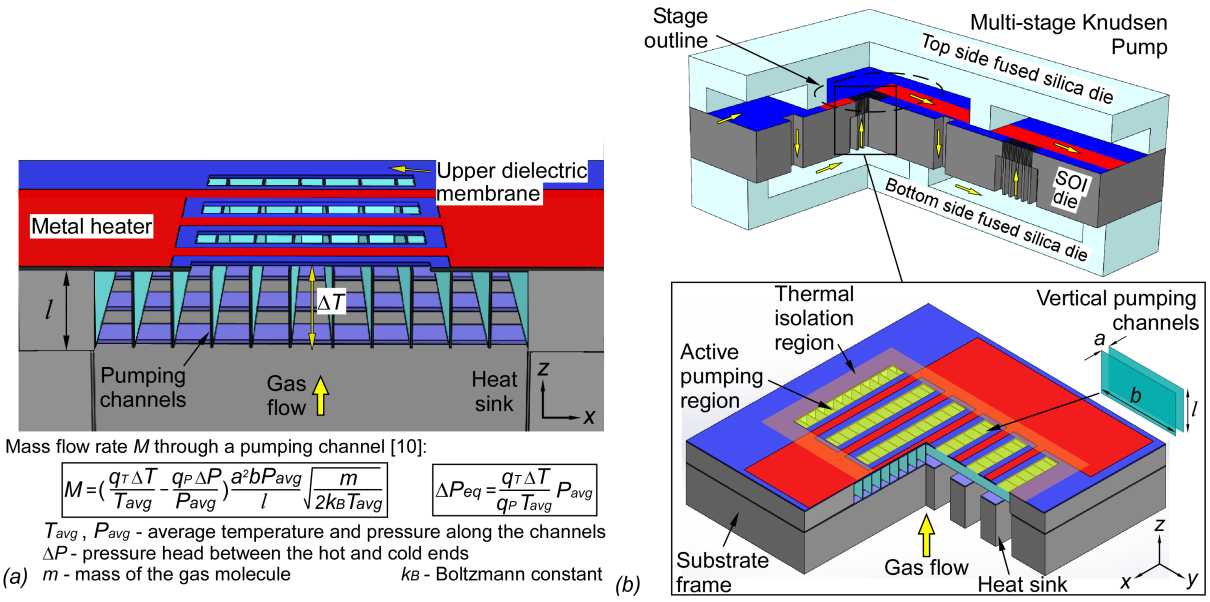

Fig. 4.1: (a) Cross-sectional view of a pumping channel with length l and temperature difference ΔT, which drives the gas flow vertically. Performance of the KP is proportional to ΔT. (b) Conceptual illustration of the multi-stage KP and the features within each pumping stage.

The Gen S2A and Gen S2B designs, analyzed in Chapter 3, are implemented in this chapter. Both KPs are comprised of 5 identical pumping stages that are cascaded in series. The stage-to-stage fluidic connection is provided by the lateral channels grooved into fused silica dies that are located above and below the SOI wafer, and by through-holes in the SOI die (Fig. 4.1b).

As described in Chapter 3, finite element analysis (FEA) is used to investigate the mechanical robustness and temperature distribution across the region of the pumping channels (Fig. 4.2a). For ease of computation, the pumping channels are modeled as composite material with thermal conductivity that is effectively equivalent to the micromachined structure. Other patterned structures, which include the heat sink, upper dielectric membrane, and heater, are modeled with the exact geometries and dimensions. To reflect the actual KP operation, the model uses electrical and thermal coupling to simulate the effects of Joule heating and the resulting change in the distribution of electrical resistance. At an applied power of 0.1 W/stage, the average temperature at the hot ends of the pumping channels (*i.e.*, in the perforated areas of the upper dielectric

membrane) reaches 370 K, whereas that at the cold ends (*i.e.*, in the perforated areas of the heat sink) is elevated to 334 K (Fig. 4.2b). This produces an average ΔT of 36 K, which is ≈30% higher than that of the Gen S1 KP at the same power level, where the channel length was 12 μm.

The simulation is further used to investigate the impact of l on the KP performance (Fig. 4.2c). The ΔT values obtained by FEA are used to calculate the resulting ΔP_{eq} and maximum flow rate (Q_{max}). At 0.1 W power, a pumping stage in this work provides a calculated ΔP_{eq} of 0.25 kPa and Q_{max} of 0.15 sccm. While further increasing l increases ΔP_{eq}, Q_{max} deteriorates due to the increase in the internal flow resistance of pumping channels, which is undesirable for μGCs.

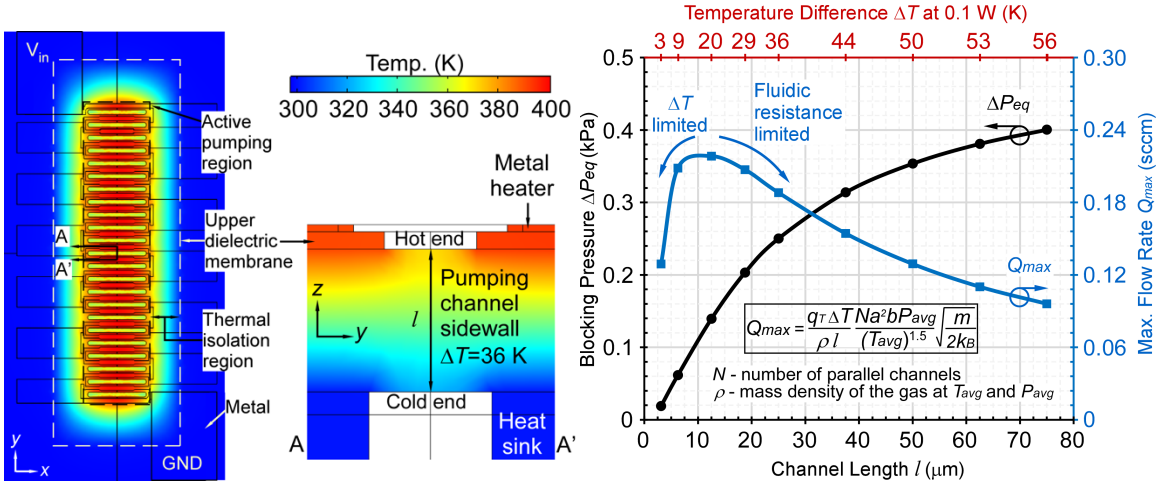

(a) (b) (c)

Fig. 4.2: FEA simulation results of Gen S2A KP with 0.1 W power/stage. (a) Lateral temperature distribution across a pumping stage. (b) Cross-sectional view of temperature distribution along an equivalent pumping channel sidewall. (c) Relation between the per-stage performance and channel length l.

4.3. Fabrication of Suspended Knudsen Pump

The fabrication of the Gen S2 KPs used five lithography masks. The first mask was used to pattern arrays of rectangular trenches through the device layer using the deep reactive ion etching (DRIE). The pumping channel sidewalls were formed by conformal atomic layer deposition

(ALD) of Al_2O_3 onto the surfaces of the trenches; the trenches were then refilled with sacrificial polysilicon deposited using low-pressure chemical vapor deposition (LPCVD) (Fig. 4.3a). The DRIE recipe was tailored to provide a positive taper angle such that the trenches could be refilled adequately.

The second mask was used to pattern perforations in the upper dielectric membrane that was first deposited by plasma-enhanced chemical vapor deposition (PECVD). The composite membrane consisted of 0.6/0.55/0.7/0.55/0.6 μm thick silicon oxide/nitride/oxide/nitride/oxide (ONONO) with a tensile stress of ≈80 MPa. The third mask was used to pattern the sputtered resistive metal heater by a lift-off process (Fig. 4.3b).

The fourth mask was used to pattern the micromachined handle layer to form heat sinks for each stage as well as through-holes for cascading the flow between stages; the micromachining of the handle layer also used DRIE. Following the DRIE step, the side of the micromachined walls structures were coated with another layer of ALD Al_2O_3 for protection against the subsequent XeF_2 release (Fig. 4.3c). The XeF_2 vapor etch of the sacrificial silicon was used to release the pumping channel sidewalls (Fig. 4.3d).

The fifth mask was used to create the lateral gas flow channels and tube insertion ports on the fused silica dies by sandblasting (via IKONICS Corp., Duluth, MI, USA). The fused silica dies were bonded to the SOI die using epoxy.

The fabricated Gen S2A KP was imaged with scanning electron microscopy (SEM). The SOI die with the five pumps and through-holes are shown in Fig. 4.4a. The top and cross-sectional views of the pumping channels, upper dielectric membrane, and metal heater are shown in Fig. 4.4b and 4.4c, respectively. The assembled 5-stage KP had a form factor of $5.4\times7.8\times2$ mm^3 (Fig. 4.4d).

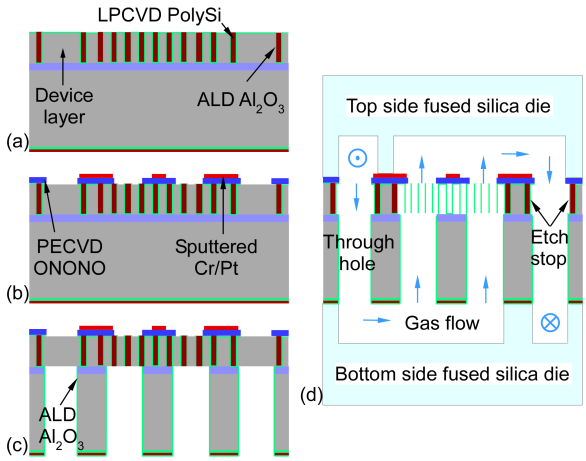

Fig. 4.3: Fabrication process flow. (a) Front side DRIE of the device silicon, ALD of Al_2O_3 channel sidewalls, and LPCVD of sacrificial polysilicon. (b) PECVD of ONONO upper dielectric membrane and Cr/Pt metallization. (c) Back side DRIE of handle silicon. (d) XeF_2 release and assembly with fused silica dies.

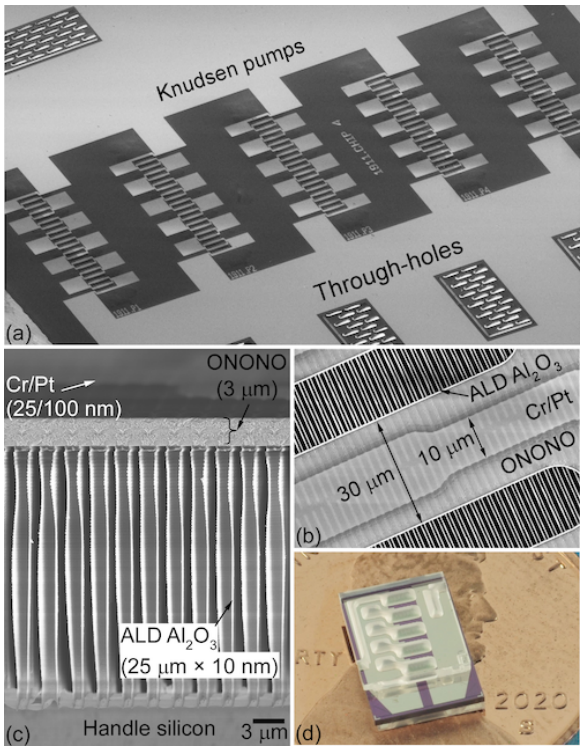

Fig. 4.4: SEM images of (a) Gen S2 5-stage KP SOI die, (b) top view of pumping channels and Cr/Pt metal heater, (c) cross-sectional view of the suspended membrane and pumping channels, and (d) photograph of the assembled Gen S2 5-stage KP.

4.4. Experimental Results

The fabricated Gen S2A and S2B KPs were evaluated at applied DC power levels of 0.1-0.5 W total (0.02-0.1 W/stage). The pressure head and flow rate were measured by a commercial differential pressure sensor (MPX5010DP, Freescale Semiconductor Inc., Austin, TX, USA) and flow meter (Model #MW-20SCCM-D, Alicat Scientific, Inc., Tuscon, AZ, USA), respectively.

The Gen S2A KP achieved Q_{max} of ≈0.36 sccm and ΔP_{eq} of ≈2 kPa at 0.5 W total applied power, *i.e.,* 0.1 W/stage, which was simulated to provide a ΔT of 36 K. The Gen S2A KP achieved a blocking pressure per unit power of 4 kPa/W (Fig. 4.5). The Gen S2B KP achieved Q_{max} of ≈0.26 sccm and ΔP_{eq} of ≈1.45 kPa at 0.5 W total applied power, *i.e.,* 0.1 W/stage or 0.05 W/membrane, which was simulated to provide a ΔT of 23 K. The experimentally obtained slopes of flow rate vs. pressure heads were within 12% of the theoretical estimate. The measured Q_{max} and ΔP_{eq} increased proportionally with applied power. The Gen S2A KP measurement results had proportional constants of ≈0.72 sccm/W and ≈4 kPa/W, and coefficients of determination of 0.999 and 0.998, respectively. The Gen S2B KP measurement results had proportional constants of ≈0.52 sccm/W and ≈2.9 kPa/W, and coefficients of determination of 0.999 and 0.999, respectively.

4.5. Discussion and Conclusion

The experimental results are benchmarked against other high-flow KPs (Q_{max} >0.1 sccm) based on ΔP_{eq} per applied power. Note that the KPs with Q_{max} <0.1 sccm, *e.g.,* [An13], were excluded from this benchmark because their flow rates were impractical for high-flow applications such as μGCs. The performance achieved by the Gen S2A KP, 4 kPa/W, is 45% higher than prior record of high-flow KPs (Fig. 4.6).

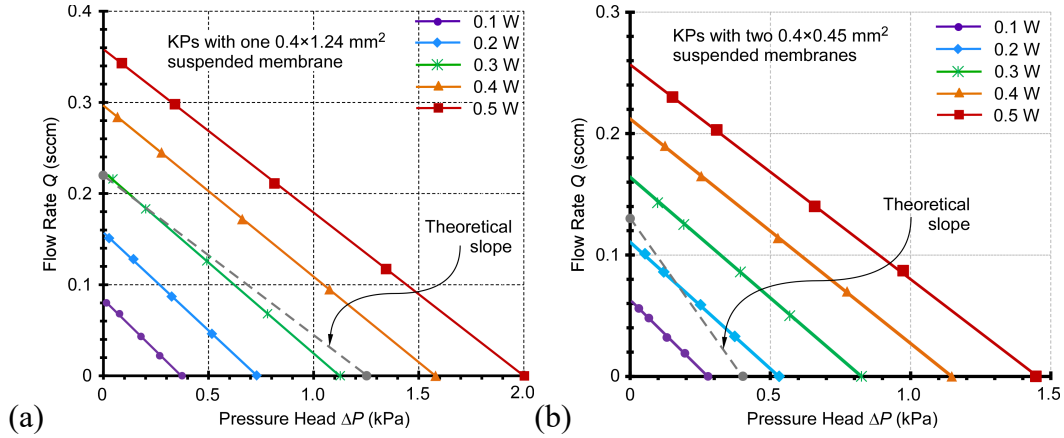

Fig. 4.5: Experimental results of the Gen S2 KPs (a) Gen S2A KP with one 0.4×1.24 mm^2 suspended membrane per stage, (b) Gen S2B KP with two 0.4×0.45 mm^2 membranes per stage. Experimentally obtained slopes are similar with theoretical expectation based on Sharipov's equation [Sha99].

The fabrication of the high-aspect-ratio pumping channels in SOI through-wafer is challenging. Footing and bowing effects of the DRIE are known to generate keyholes in the subsequent LPCVD refill of the trenches [Zhu05]. Consequently, the keyholes can create micro-voids in the upper dielectric membrane [An14, Zhu05]. Such defects cause poor mechanical robustness and high stress concentration regions that tend to crack the membrane upon release or when heated during operation, which limits the power that can be applied to the KP. The footing and bowing effects can be reduced by increasing the passivation layer thickness whereas the keyholes can be mitigated by V-shaped trenches with wider opening [Zhu05].

In summary, this work presented experimental and modeling evidence to show that the blocking pressure for monolithic SOI through-wafer KPs can be enhanced. The enhancement was achieved by using 25 µm long, 1.2 µm wide pumping channels with 10 nm thick Al_2O_3 sidewalls, and by cascading five pumping stages in series within a monolithic structure. The blocking pressure per applied power was 45% higher than prior record of comparable KPs. Such blocking pressure enhancement in KPs could provide suitable performance for high pressure head applications such as µGCs with long separation columns.

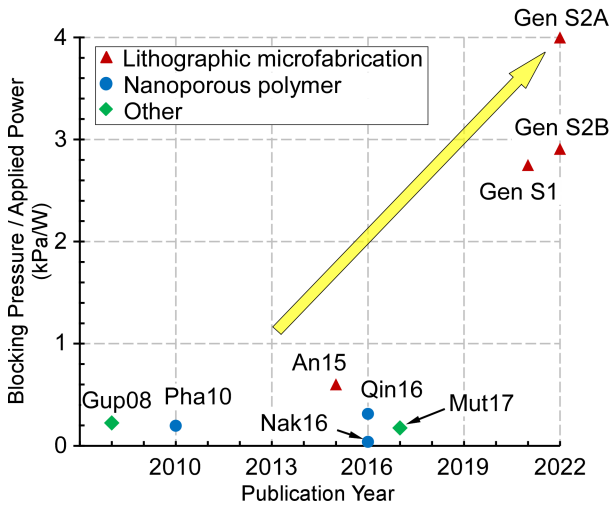

Fig. 4.6: Benchmarking of high-flow (Q_{max}>0.1 sccm) KPs' blocking pressure per applied power. The Gen S2A 5-stage KP in this work has 45% higher blocking pressure per applied power than prior record.

Chapter 5:

Gen U1: Unsuspended Mechanically Robust Knudsen Pumps for Monolithic Gas Analysis System

5.1. Introduction

As described in Chapter 1, the prior work on lithographically microfabricated KPs implemented suspended membranes to create the temperature difference along the pumping channels to generate gas flow [An13, An14, An15, Gup12, McN05, Qin15]. In addition, the high-flow KPs have employed 10 nm thick dielectric pumping channel sidewalls to densely array a large number of pumping channels [An15]. With similar suspended membrane and pumping channel combination, the Gen S1 and Gen S2 KPs presented in Chapters 2 and 4, respectively, provided high performance.

The suspended membranes, utilized in prior work, generally have a tendency to buckle under compressive stress, crack under high tensile stress, and hence require a delicate stress balancing [An13, An15, Ben19, Elb97, Guc85, Guc92, Wag96]. Furthermore, the through-wafer gas flow perforations in the suspended membrane of the KP increase the localized tensile stress of the membrane [Ben19, Mei67, Wan16]. Therefore, the composite film stress of the suspended membrane is typically tuned at a mild tensile level of 40-80 MPa by adjusting the thicknesses of the compressive silicon oxide and tensile silicon nitride layers [An13, An15]. When heated during operation, the thermal stress of the membrane is partially or fully relieved depending on the operation temperature. Combined with the thermal expansion of the metal heater, which can act as a load, the the suspended membrane can buckle due to compression or crack due to poor

mechanical robustness associated with the structural defects [Che20, Mei67, Wan16]. Consequently, the applied power to the KP and hence its performance can be limited by such potential failures at elevated temperatures, as observed in Chapter 4.

In addition to the stress balancing, the composite film quality of the suspended membrane can be susceptible to the deposition processes [An14, Che20, Her82, Luc87, Man93, McI87, Pet00, Xie15]. The commonly used plasma-enhanced chemical vapor deposition (PECVD) process enables process compatibility and a lower temperature deposition at a faster rate compared to a low-pressure chemical vapor deposition (LPCVD) process [Her82, Luc87]. However, the fast deposition could produce structural defects such as micro-voids on a previously roughened surface (explained below), which limits the surface mobility of the reacting species. Unable to reach the low energy states, the deposited materials form micro-voids nearby the surface features [Che20, McI87]. The micro-voids are the source of high stress concentration, low mass density, and poor mechanical robustness of the suspended membrane, which could compromise the structural integrity of the KP [Che20, Man93, McI87, Xie15]. In contrast, the more conformal LPCVD at a higher temperature can produce higher quality composite film with less micro-void [Pet00]. However, the conformality of the LPCVD can deposit the materials into the features of the roughened surface from the preceding steps and cause an overhanging membrane upon release, as observed in prior KPs [An14].

Such structural defects of the suspended membrane are caused by the roughened substrate surface from the preceding fabrication steps to refill the trenches created for the vertical pumping channels. The LPCVD refill of a trench is known to generate a keyhole, *i.e.,* a vertical void in the middle the trench due to an inadequate refill from the sides [Qia10, Xie15, Zhu05]. Such keyholes are more apparent in higher aspect ratio trench refills because the deep reactive ion etching (DRIE)

process used for creating the trenches has inherent bowing and footing effects where the plasma unintentionally etches laterally [Arn91, Hwa97, Noz95, Qia10, Zhu05]. Such effects are caused by the nonuniform localized surface charging near the top and bottom of the trench. The longer DRIE of deeper trenches result in wider bowing and footing due to more charging and ion collisions at the top of the trench, and longer over-etch at the bottom, respectively [Arn91, Hwa97, Ish99, Noz95, Tan18]. The efforts to mitigate these challenges and produce a keyhole-free trench refilling involve complicated masking and multiple custom DRIE steps [Ish99, Qia10, Zhu05].

This chapter describes the Gen U1 monolithic KP with superior mechanical robustness and facile microfabrication. This work bypasses the fabrication and operation challenges associated with the suspended membrane and ultra-thin pumping channel sidewalls, which were utilized in Gen S1 and S2 KPs. The pumping channels are fabricated through the upper oxide layer and device silicon layer of a silicon-on-insulator (SOI) wafer. The temperature gradient is created using a silicon oxide film with low thermal conductivity. Multiple pumping channels are arranged in parallel to scale the flow rate. Such unsuspended KP architecture with facile microfabrication offers high manufacturability and reliability.

5.2. Structural and Process Design

As described in Chapter 1, the KP facilitates thermal transpiration in a narrow channel with hot and cold ends, which can be comprised of three fundamental units: the narrow channel, a heater, and a heat sink. The Gen U1 unsuspended through-wafer KP is designed on an SOI substrate with a 12 μm thick device silicon layer, a 0.38 μm thick buried oxide layer, and a 525 μm thick handle layer. The device silicon layer is covered by a 2 μm thick upper oxide layer. The pumping channels have a length l of 14 μm, penetrating through the upper oxide and the device silicon

layers (Fig. 5.1a). Each pumping channel has a rectangular opening with a shorter side width (*i.e.*, channel width *a*) of 1.2 μm and a longer side width (*b*) of 200 μm. The channel width of 1.2 μm is selected to provide a well-balanced performance of pressure head and flow rate for the μGC application. The vertical aspect ratio of the pumping channel (≈12) is highly manufacturable with the DRIE process [Fu09, Wu10]. On top of each pumping channel are two parallel metal traces located along the two longer sides that serve as a Joule heater (Fig. 5.1b). The handle layer serves as the heat sink while incorporating a 30×230 μm^2 perforation below each pumping channel to allow through-wafer vertical gas flow. The perforation width of 30 μm is selected to maintain sufficient heat sinking while contributing negligible flow resistance to the KP. In addition, the through-wafer process with such a vertical aspect ratio is highly manufacturable using DRIE, as achieved in Gen S1, S2, and other work [An15, Tan18].

With no suspended membrane, this KP design can be fabricated with a simple, reliable process. Previously utilized complex process steps of the membrane fabrication such as the trench refill, polish, and sacrificial etch are eliminated from the process flow [An13, An15, Bya21, Bya22]. Consequently, the structural defects such as LPCVD keyholes, PECVD micro-voids, and overhanging membrane are prevented [An14, Bya22, Man93, McI87, Qia10, Xie15, Zhu05].

During operation, the heater is powered whereas the handle layer is cooled, generating a temperature difference that drives the gas molecules between the top/hot and bottom/cold ends of the pumping channels (Fig. 5.1c). Because of the small thermal conductivity of the oxide, the majority of the temperature difference is effectively applied across the upper oxide layer. The thickness of the upper oxide layer is chosen to provide sufficient temperature difference along the pumping channel without employing a suspended membrane, while maintaining manufacturability [Nak95, Pi16, Pli65].

There are three unsuspended KP designs in this work: 4-, 6-, and 45-channel KPs with footprints of 3×3.75 mm^2, 4.5×3.75 mm^2, and 7.5×15 mm^2. Each KP design contains a corresponding number of identical pumping channels, fluidically connected in parallel to scale the flow rate. The pumping channels within each KP are spaced apart from each other by ≈1.5 mm. Such a relatively sparse arrangement reduces the power per unit area and hence facilitates heat sinking. The three KP designs are implemented in two chip versions. For both versions of chips, the SOI substrate is sandwiched between two fused silica dies, which incorporate 40 µm deep lateral channels for gas flow routing and 500 µm deep gas inlet and outlet ports. For ease of manual handling and bonding with the fused silica dies, Version A is comprised of two 4-channel

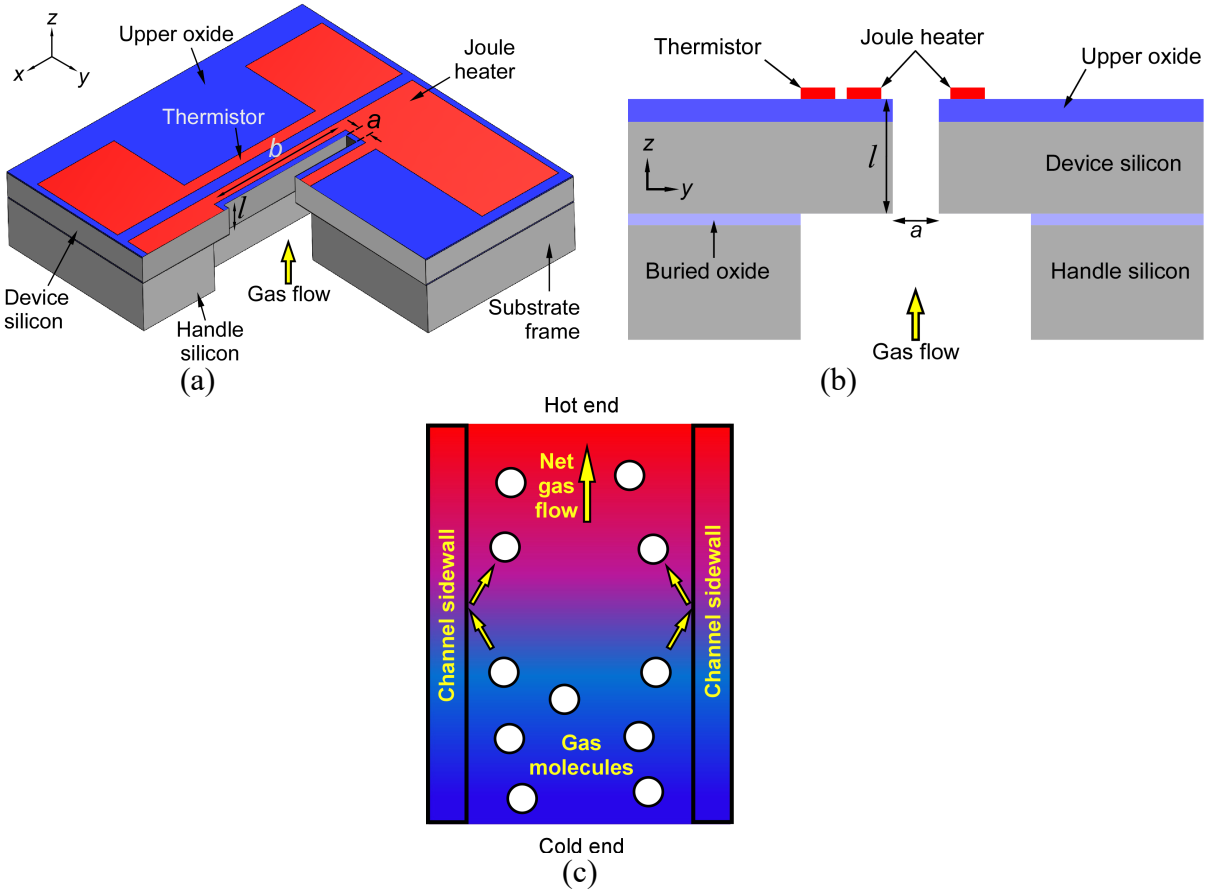

Fig. 5.1: (a) Conceptual illustration of a pumping channel. (a) 3D drawing, (b) a cross-sectional view, and (c) thermally driven gas flow through the pumping channel.

KPs and two 6-channel KPs, with a total footprint of 7.5×7.5 mm^2. Version B is the 45-channel KP with a footprint of 7.5×15 mm^2.

A number of thermistors are integrated to provide temperature measurements and feedback control. Each KP incorporates a thermistor that is located 5 μm away from a metal heater trace and intended to measure the heater temperature. Because the heat during operation is highly localized around the heater, the temperature at the cold ends of the pumping channels is similar to the bulk silicon temperature far away from the pumping channels (as illustrated in Section 5.3). Therefore, the temperature at the cold ends of the pumping channels is measured by a thermistor at least 1 mm away from the active metal heaters. The heaters and thermistors incorporate two metal layers. A thinner Metal1 layer (30/100 nm Ti/Pt) forms the lead pads, the localized heating and temperature sensing traces, and their connection areas to the lead pads. A thicker Metal2 layer (30/750 nm Ti/Ni) is added to the lead pads to facilitate soldering for the experimental evaluation, and added to the connection areas to reduce the parasitic resistance of the Metal1. The metal thicknesses are selected for fabrication considerations such as residual stress and adhesion to the substrate.

5.3. Modeling

The structural robustness and temperature distribution of the KP designs are analyzed through electrically and thermally coupled solid mechanics models, using finite element analysis (FEA) in COMSOL Multiphysics®. The Version A and Version B chips are modeled with the designed parameters described in Section 5.2. Specifically, for the Version A chip that incorporates multiple KPs, each KP is individually heated. In the models, the chips are seated on a printed circuit board (PCB) with a metal heat sink on the bottom side, mimicking the actual usage and experimental

conditions. The material properties and thicknesses assumed in the models are listed in Table 5.1. The electrically and thermally coupled models generate Joule heating by a voltage input applied to the heater. The temperature coefficients of resistivity (TCR) of the metal layers were incorporated into the model to reflect the electrical resistances more accurately during heating.

Figure 5.2a shows the simulated cross-sectional temperature distribution of the pumping channel in a typical 4-channel KP. An effectively applied power (W_p) of 0.5 W/channel (2 W total) generates an average temperature at the hot ends of the pumping channels ($T_{h.p}$) of 180ºC, an average temperature at the cold ends of pumping channels temperature ($T_{c.p}$) of 88ºC, and an average temperature difference ΔT (=$T_{h.p}$ - $T_{c.p}$) of 92ºC. Owing to its low thermal conductivity of 1.4 W/mK, the upper oxide layer localizes the heat spread near the pumping channel openings (Fig. 5.2b). Therefore, the bulk silicon temperature measurement by a thermistor located at least 1 mm away from the active metal heater is used to represent $T_{c.p}$ at the bottom of the thermally conductive (130 W/mK) device silicon. When the 4-channel and 6-channel KPs are operated at 0.5 W/channel, the top fused silica surface of the Version A chip heats up to a maximum of 55ºC and 75ºC, respectively (Fig. 5.2c-d). In contrast, the top fused silica surface of the Version B chip reaches a maximum of 150ºC at 0.5 W/channel or 22.5 W total W_p (Fig. 5.2e).

Table 5.1: Material properties and thicknesses assumed in the FEA

Structure	Material composition	Thickness (μm)	Thermal conductivity (W/mK)	Resistivity (Ω·m)	TCR (K^{-1})
Handle layer	Si	525	130	-	-
Buried oxide	SiO_2	0.38	1.4	-	-
Device layer	Si	12	130	-	-
Upper oxide	SiO_2	2	1.4	-	-
Metal1	Ti/Pt	0.03/0.1	76	2.39×10^{-7}	1.3×10^{-3}
Metal2	Ti/Ni	0.03/0.75	87	8.35×10^{-8}	5.9×10^{-3}
Fused silica die	Fused silica	750	1.4	-	-
PCB	Cu/FR4/Cu	35/1500/35	401/0.3/401	-	-
Metal heat sink	Al	5000	237	-	-

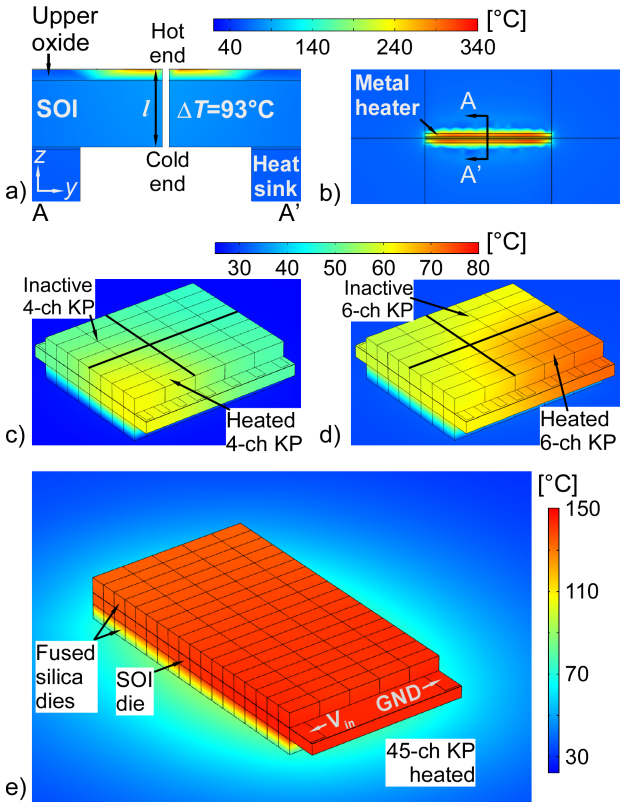

Fig. 5.2: FEA results at W_p of 0.5 W/channel. (a) Cross-sectional view of a single pumping channel of the 4-channel KP, (b) top view of a single pumping channel, (c) Version A chip with 4-channel KP heated, (d) Version A chip with 6-channel KP heated, (e) Version B chip with 45-channel KP heated.

By sweeping the input heater voltage, the W_p is swept through 0-0.5 W/channel to investigate the temperature distribution and its impact on the pumping performance. The average ΔT values of all three KPs are within 8% of each other at a given power level per channel (Table 5.2 and Fig. 5.3a). This difference is likely caused by the variation in total W_p and chip footprint. However, T_{avg}, defined as the average of $T_{h,p}$ and $T_{c,p}$, has significant difference among the three KPs (Fig. 5.3b). The T_{avg} can represent the overall heating of the chip and the effectiveness of heat sinking. Figure 2e shows that the PCB temperature underneath the 45-channel KP is elevated up to ≈85ºC. At W_p of 0.5 W/channel, T_{avg} reaches ≈385ºC for the 45-channel KP and ≈145ºC for the 4- and 6-channel KPs (Fig. 5.3b), impacting the pumping performance as described below (Fig. 5.3c-d).

Table 5.2: Simulation results of average temperatures at W_p of 0.5 W/channel

Temperature	4-ch. KP	6-ch. KP	45-ch. KP
$T_{h,p}$ (°C)	180	195	430
$T_{c,p}$ (°C)	88	101	340
T_{avg} (°C)	134	148	385
ΔT (°C)	92	94	90

Based on Sharipov's equation [Sha99], the blocking pressure ΔP_{eq} can be calculated by equating M to zero in Eq (2.1):

$$\Delta P_{eq} = \frac{q_T}{q_P}\frac{\Delta T}{T_{avg}} P_{avg} \tag{5.1}$$

where q_T and q_P are the thermal creep and viscous flow coefficients, respectively, which are dependent on T_{avg} and have been reported in literature [Sha99]. The flow rate of a KP reaches its maximum (Q_{max}) when ΔP is equal to zero in Eq (2.1):

$$Q_{max} = \frac{q_T \Delta T}{(T_{avg})^{1.5}} \frac{Na^2 b P_{avg}}{\rho l}\left(\frac{m}{2k_B}\right)^{0.5} \tag{5.2}$$

where N is the number of parallel pumping channels and ρ is the mass density of the gas at T_{avg} and P_{avg}. It is worth noting the impact of T_{avg} on ΔP_{eq} and Q_{max}. Based on the tabulated q_T and q_P values [Sha99], q_T increases with T_{avg} (Fig. 5.3e) whereas q_P decreases with T_{avg} (Fig. 5.3f). For ΔP_{eq}, the q_T and q_P largely cancel the impact of T_{avg}, causing ΔP_{eq} to be minimally dependent on T_{avg}. In contrast, the Q_{max} has a higher dependency on T_{avg}. Therefore, the calculated performance of all three KPs show a nonlinear relation to W_p (Fig. 5.3c-d). This effect is especially prominent in the Q_{max} of 45-channel KP, which has a high T_{avg} due to the high total W_p. Such high T_{avg} of the 45-channel KP results in 33% lower Q_{max}/channel compared to the 4- and 6-channel KPs.

5.4. Fabrication of Unsuspended Knudsen Pump

The unsuspended KPs were fabricated on an SOI wafer using a six-mask process. The upper oxide was deposited by PECVD on the blank SOI wafer, which facilitates a high quality film deposition [Bat86] compared to a roughened substrate, as described in Section 5.1. The residual stress was measured at ≈50 MPa compressive. Metal1 and Metal2 were patterned by an image-reversal lithography using the first and second masks, deposited by a thermal evaporator, and lifted

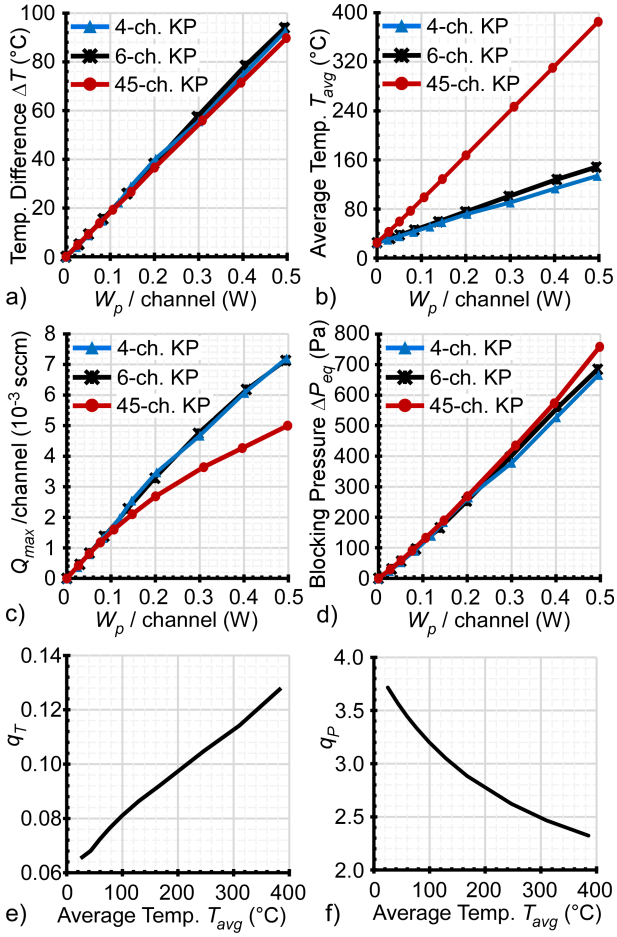

Fig. 5.3: Analytical modeling results. (a) The temperature difference ΔT along the pumping channels, (b) the average temperature T_{avg} along the pumping channel, (c) the maximum flow rate per channel (Q_{max}/channel), and (d) blocking pressure ΔP_{eq} of 4-, 6-, and 45-channel KPs at W_p of 0.1-0.5 W/channel. The decreasing and increasing relation between (e) thermal creep coefficient q_T and (f) viscous flow coefficient q_P with T_{avg}.

off (Fig. 5.4a-b). The 1.2×200 μm^2 pumping channels were defined by the third mask and etched through the upper oxide and device silicon layers using an inductively-coupled DRIE processes (Fig. 5.4c). In addition to the well-balanced pumping performance, the 1.2 μm opening width of the pumping channels enabled a high yield to etch through the 2 μm thick upper oxide and 12 μm thick device silicon layers.

The heat sink with 30×230 μm^2 openings were defined by the fourth mask and etched through the SOI handle layer using a DRIE recipe tailored for achieving a high aspect ratio [Tan18]. The 30 μm opening width enabled a high DRIE yield. Subsequently, the exposed buried oxide was dry etched, attaining through-wafer perforations that are fluidically connected to the pumping channels (Fig. 5.4d). The fifth and sixth masks were used to pattern the lateral channels for gas flow routing, and gas inlet and outlet ports, respectively, on the fused silica dies by sandblasting (serviced from IKONICS Corp., Duluth, MI, USA).

The bonding of SOI and fused silica dies was provided by a low-viscosity epoxy (Epotek-377, Epoxy Technology Inc., MA, USA). Fused silica capillary tubes (with an inner diameter of 250 μm) were attached to the gas inlet and outlet ports using a high-viscosity epoxy (Stycast2850FT, Henkel, Germany) (Fig. 5.4e). Figure 5 shows the SEM and microscopic images of the fabricated KP. The cross-sectional SEM images show the pumping channel through the upper oxide and device silicon layers, and the handle layer perforation (Fig. 5a-b). The microscopic top view shows the pumping channel, thermistor, and the two metal layers (Fig. 5c). The assembled Version A and Version B chips are photographed in Fig. 6.

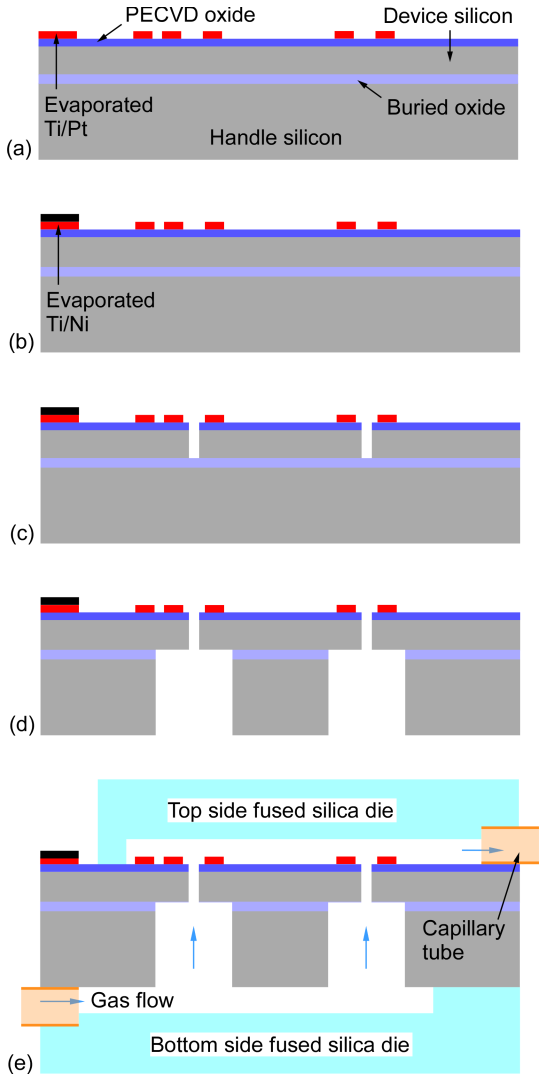

Fig. 5.4: Process flow. (a) PECVD of upper oxide layer and Metal1 patterning with Mask 1. (b) Metal2 patterning with Mask 2. (c) Top side DRIE for pumping channels with Mask 3. (d) Bottom side DRIE for heat sink perforations with Mask 4. (e) Assembly of the SOI die with fused silica dies, sandblasted with Masks 5 and 6, and capillary tubes.

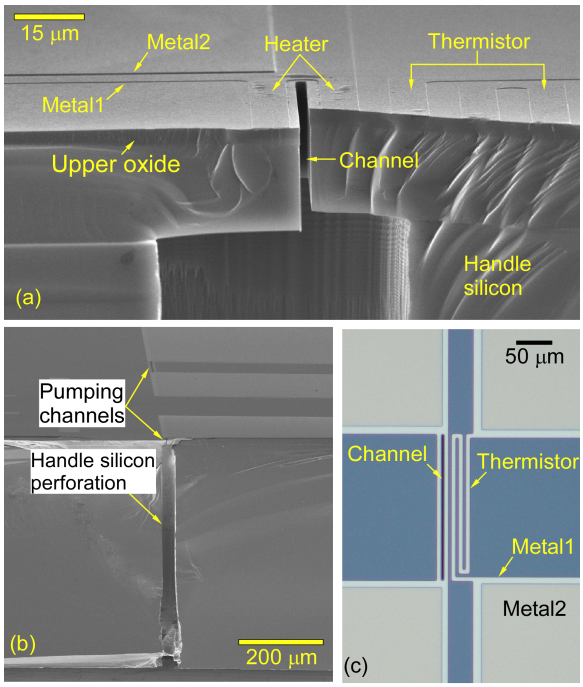

Fig. 5.5: Gen U1 unsuspended KP features. (a) SEM image of the pumping channel and heat sink perforation for through-wafer gas flow. (b) SEM image of the pumping channel cross-section. (c) Microscopic image of the pumping channel and heater thermistor.

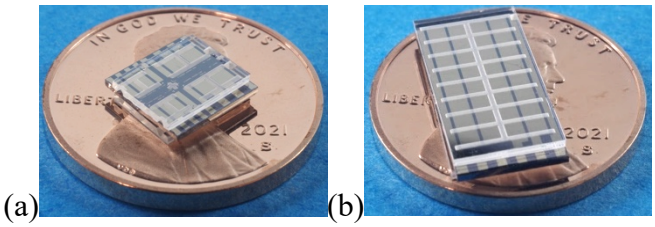

Fig. 5.6: Photographs of (a) Version A chip with two 4-channel and two 6-channel KPs, and (b) Version B chip with the 45-channel KP.

5.5. Experimental Results

The Gen U1 unsuspended KPs were evaluated using the experimental setup illustrated in Fig. 5.7. The assembled device under test (DUT) was mounted on a custom PCB. The lead pads of the chips were connected to the PCB through 90º header pins using a high-temperature solder paste (SMD291AX10T4, Chip Quik Inc., Ontario, Canada). The bottom side of the PCB was attached

to a metal block that served as a heat sink. Thermal pads and conductive paste were used to ensure good thermal contact between the DUT, the PCB, and the heat sink. The gas inlet tube was open to ambient, whereas the outlet tube was connected to a differential pressure sensor (MPX5010DP, Freescale Semiconductor Inc., Austin, TX, USA) that measured the applied pressure head between the KP outlet and the ambient. The flow rate was measured by a flow meter with negligible flow resistance (Model #MW-20SCCM-D, Alicat Scientific, Inc., Tuscon, AZ, USA) connected in series with the KP. The experiments were conducted at five different loading conditions – no external load (flow meter only), three intermediate pressure heads, and fully blocked. Capillary tubes with various inner diameters and lengths were connected to the outlet of the flow meter to provide the intermediate pressure heads.

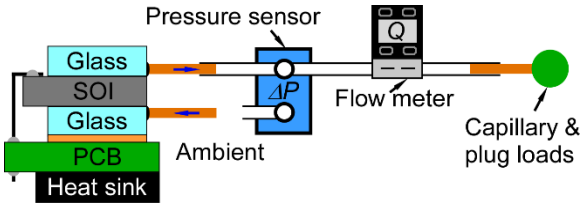

Fig. 5.7: Experimental measurement setup drawing.

The 4- and 6-channel KPs on the Version A chip were tested individually at W_p of 0.1-0.5 W/channel, *i.e.,* total W_p of 0.4-2 W and 0.6-3 W, respectively (Fig. 8a-b). The 45-channel KP was tested at W_p of 0.04-0.2 W/channel, *i.e.,* total W_p of 1.8-9 W (Fig. 8c). The total W_p was limited at 9 W for the 45-channel KP to avoid overheating of the DUT, which reached 280ºC according to the measurement of thermistor that represented the heater temperature.

At W_p of 0.2 W/channel, the 4-channel KP provided a Q_{max} of 0.015 sccm and a ΔP_{eq} of 164 Pa (0.8 W total), the 6-channel KP provided a Q_{max} of 0.020 sccm and a ΔP_{eq} of 160 Pa (1.2 W total), and the 45-channel KP provided a Q_{max} of 0.036 sccm and a ΔP_{eq} of 170 Pa (9 W total). The

Q_{max}/channel of 45-channel KP was 0.8×10^{-3} sccm and ≈77% lower than those of 4- and 6-channel KPs, which were 3.7×10^{-3} sccm and 3.3×10^{-3} sccm, respectively (Fig. 8e). This is discussed in Section 6. A critical relevant parameter is the bulk silicon temperature in each design, which was measured at 63ºC, 83ºC, and 184ºC in the 4-, 6-, and 45-channel KPs, respectively. The Q_{max} of 4- and 6-channel KPs were 43% and 10% higher than the calculation results whereas the ΔP_{eq} were 7% and 17% lower, respectively.

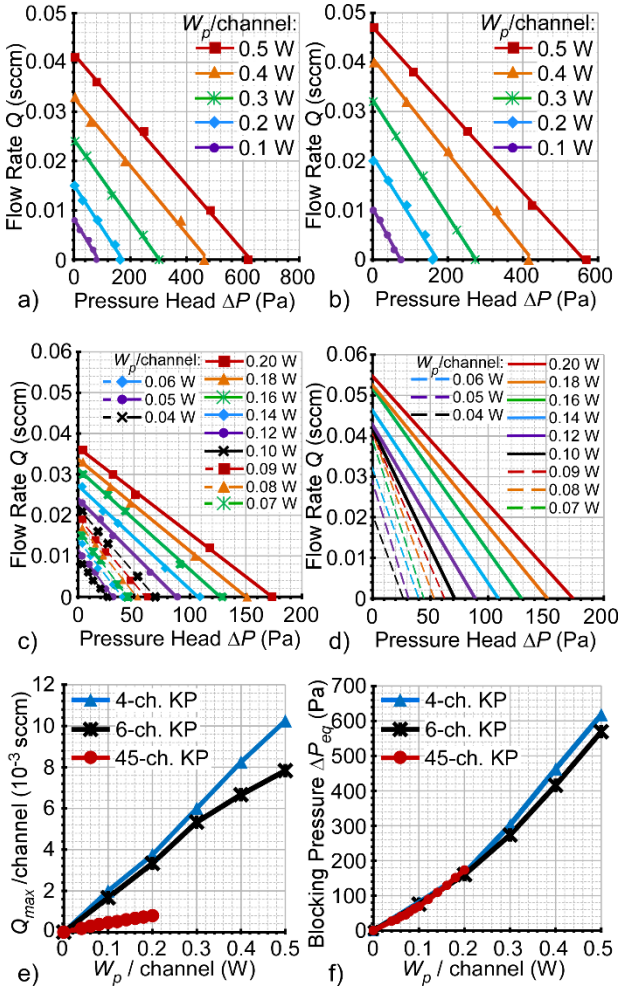

Fig. 5.8: Experimental results of (a) 4-channel KP at W_p of 0.1-0.5 W/channel, (b) 6-channel KP at W_p of 0.1-0.5 W/channel, (c) 45-channel KP at W_p of 0.04-0.20 W/channel. (d) The projected performance of the 45-channel KP without the internal flow resistance of the lateral channels. Experimentally measured trends of (e) the maximum flow rate per channel, and (f) the blocking pressure of 4-, 6-, and 45-channel KPs with respect to W_p.

The 4- and 6-channel KPs were monolithically implemented in an on-chip gas analysis system with gas chromatography elements such as a preconcentrator, capacitive detector, and separation column. At W_p of ≈0.4 W/channel, the 6-channel KPs provided a flow rate of ≈0.01 sccm for sampling and ≈0.01 sccm for separation. Such performance has demonstrated a successful sampling and separation of multiple volatile organic compounds in an upcoming publication*.

5.6. Discussion and Conclusion

The performance of the 4-channel KP in this work is benchmarked against other KPs in literature based on the Q_{max} per channel opening area and ΔP_{eq} per pumping stage (Fig. 5.9). The Q_{max} per channel opening area in this work (42.7 sccm/mm^2) exceeds that of Gen S1, Gen S2, and other through-wafer KPs [An15, An14] with large number of (10^3-10^4) densely arrayed pumping channels with large opening area. This is attributed to the higher ΔT allowed by the robust pumping channel structure with low structural defects in this work, compared to nanoporous media or ultra-thin dielectric pumping channel sidewalls. The blocking pressure achieved in this work is similar to the per-stage blocking pressure of the Gen S1 and Gen S2 suspended KPs with high flow rates. The combination of the blocking pressure per stage and maximum flow rate per channel area of the unsuspended Gen U1 KP exceeds that of the suspended KPs and other KPs in literature.

**The design and experimental work have been conducted by Mr. Xiangyu Zhao*

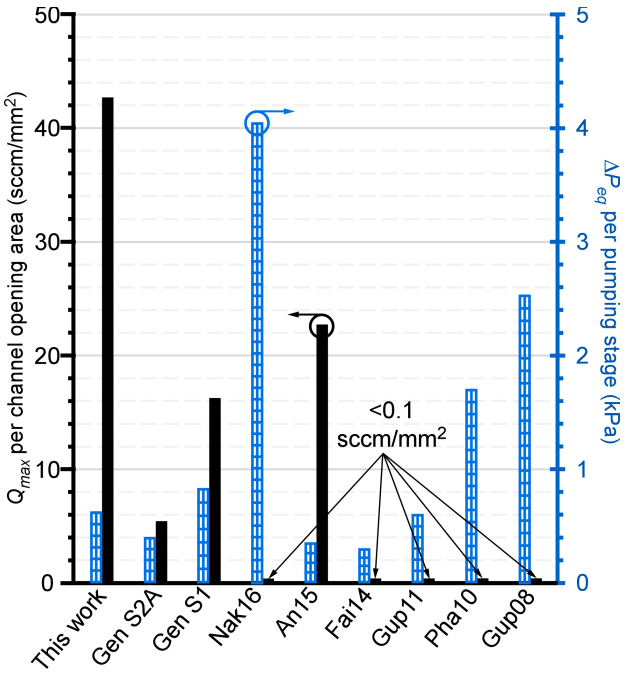

Fig. 5.9: Benchmarking of the KPs based on the blocking pressure per pumping stage (in blue) and maximum flow rate per channel opening area (in black). The maximum flow rate per channel opening area achieved by the 4-channel KP in this work is ≈2× higher than prior record.

The experimentally measured Q_{max} of the 45-channel KP was 70% lower than the calculation result. Given the large number of pumping channels and corresponding chip area, the 45-channel KP has long lateral channels in the fused silica dies, which can lower the experimentally measured Q_{max}. The flow resistance (R_h) of the lateral channels and heat sink was calculated by the following equation [Pri16]:

$$R_h = \frac{12\mu L}{wh^3(1-0.63h/w)} \tag{5.3}$$

where μ is the dynamic viscosity of air; L, w, and h are length width, and height ($w \geq h$) of the channel. In contrast, the flow resistance of the pumping channels was calculated from Eq (2.1) at zero ΔT. The calculation results showed that the internal flow resistance of the lateral channels in the 45-channel KP was 2.4× greater than that of its pumping channels (Table 5.3). The effective flow resistance of the pumping channels in the 45-channel KP was estimated by subtracting the

flow resistance of the lateral channels from the experimentally measured flow resistance of the KP, the latter of which is equal to the measured ΔP_{eq} per Q_{max}. Based on the measured ΔP_{eq} and the estimated effective flow resistance of the pumping channels, the projected performance of the 45-channel KP without any flow restriction from the lateral channels is shown in Fig. 5.8d.

As described theoretically and measured experimentally, due to the higher T_{avg}, the flow rate per channel of the 45-channel KP was significantly lower than that of 4- and 6-channel KPs. Similar trend was observed in prior work [An15]. Based on the temperature measurement provided by the thermistor located 5 μm away from the active metal heater, the 6-channel KP's heater reached $T_{h.p}$ of 101ºC at W_p of 0.2 W/channel. Given its bulk silicon temperature measurement or $T_{c.p}$ of 83ºC, the T_{avg} along the pumping channels was measured at 92ºC. Similarly, the 45-channel KP had a measured $T_{h.p}$ of 279ºC, $T_{c.p}$ of 184ºC, and T_{avg} of 232ºC at W_p of 0.2 W/channel. Based on the measured T_{avg}, the corresponding q_T values (Fig. 5.3e), and Eq. (5.2), Q_{max} of the 45-channel KP was estimated to be 67% lower than that of the 6-channel KP. This estimation is closer to the experimentally measured discrepancy of 76% than the theoretically calculated discrepancy of 30%. With appropriate correction factors, thermistors can provide estimation and feedback control to the performance.

To avoid the excessive substrate heating and performance deterioration in KPs with numerous pumping channels and high applied power, the bottom side of the PCB can be cooled more effectively with supplementary cooling elements such as heat pipes instead of only the metal block used in this chapter [Fag12]. Such cooling can provide lower T_{avg}, which provides lower q_T, higher q_P, and thus higher flow rate (Fig. 5.3).

The discrepancies between modeling and experimental results may be caused by the material properties assumed in the modeling. In particular, the thermal conductivity of PECVD silicon

Table 5.3: Calculated flow resistance of the units in each KP (kPa/sccm)

KP	Pumping channels	Heat sink	Lateral channel
4-ch.	15.63	0.1	0.64
6-ch.	10.42	0.07	0.93
45-ch.	1.39	0.01	3.27

oxide (assumed 1.4 W/mK in this work) is subject to change with respect to the deposition conditions [Mir98]. Higher thermal conductivity of the upper dielectric oxide could deteriorate the temperature difference along the pumping channel, hence the performance significantly. For example, according to the FEA of the 4-channel KP at W_p of 0.5 W/channel, ΔT would be 11ºC if a 2 µm thick PECVD silicon nitride with a thermal conductivity of 20 W/mK was used as the upper dielectric instead of the silicon oxide, which provided ΔT of 92ºC. The FEA results also showed that 85ºC of the total ΔT of 92ºC is along the 2 µm thick oxide layer (Fig. 5.2a), which suggests that the contribution of the device layer to the pumping is minimal. In addition, the internal flow resistance of the 12 µm thick device silicon layer is 6× higher than that of the 2 µm thick upper oxide layer due to its length. While the SOI substrate, in particular the buried oxide layer, is necessary for the etch stop during the top and bottom side DRIE steps, the device silicon layer thickness can be reduced for fabrication ease and the upper oxide layer thickness can be increased for higher ΔT. Such structures with thinner device silicon and thicker upper oxide need to be evaluated against structural deformation and mechanical robustness due to residual stress at both ambient and operating temperatures, similar to the work in Chapter 3.

In summary, this chapter reports on a mechanically robust KP with facile fabrication. With no suspended membrane or ultra-thin features, the reported KPs offer high manufacturability and reliability. The 4-channel KP in this work achieved a measured maximum flow rate of 0.047 sccm and blocking pressure of 620 Pa at an applied power of 2 W. Such performance is suitable for providing chemical vapor sampling and separation for certain µGCs. A monolithic

implementation of the 4- and 6-channel KPs in a lab-on-a-chip gas analysis system is achieved in this work and will be reported in an upcoming publication. Future work includes thermal management and performance scaling.

Chapter 6:

Conclusions and Future work

6.1. Conclusions

This thesis explores two types of lithographically microfabricated SOI through-wafer KPs. The first type is a suspended membrane based KP. Owing to the thermal isolation provided by the suspended membrane and 10 nm thick pumping channel sidewalls, the Gen S1 and Gen S2 KPs provide superior performance than the unsuspended KP or porous media based KPs. The Gen S1 KP is the first implementation of monolithic multi-stage through-wafer KP. Such design approach enables performance scaling without external frames or tubing to provide fluidic connection. With four monolithic series of pumping stages comprised of 1.2 μm wide, 12 μm long parallel pumping channels, the Gen S1 KP provides a blocking pressure of 3.3 kPa and a maximum flow rate of 0.75 sccm at an applied power of 1.2 W. The blocking pressure per applied power of this KP is 4.5× higher than other high-flow KPs with the maximum flow rate exceeding 0.1 sccm. Figure 6.1 shows the operating point, a flow rate of 0.48 sccm flow rate at a pressure head of 1.14 kPa, provided by the Gen S1 4-stage KP in a μGC system with ≈2.5 kPa/sccm fluidic resistance. Such performance is suitable for providing the separation gas flow for certain μGCs.

To further increase the blocking pressure, the Gen S2 KPs employed 25 μm long pumping channels, which are ≈2× longer than those of the Gen S1 KP. Such pumping channel length is the longest in through-wafer KPs to date. The number of series pumping stages increased up to five,

with an ability to scale up to 30 pumping stages depending on the dicing and assembly of the fabricated 17.3×20.3 mm^2 die. The mechanical robustness and thermal distribution of the suspended membrane are analyzed and improved for higher process yield and reliability. The Gen S2A 5-stage KP with 0.4×1.25 mm^2 suspended membranes provides a blocking pressure of 2.0 kPa and a maximum flow rate of 0.36 sccm at an applied power of 0.5 W. The Gen S2B 5-stage KP with 0.4×0.45 mm^2 suspended membranes provides a blocking pressure of 1.45 kPa and a maximum flow rate of 0.26 sccm at an applied power of 0.5 W. At a given power level, the Gen S2A KP exceeds the blocking pressure of the Gen S1 KP by 45% and the maximum flow rate by 15%. Such blocking pressure per applied power is the highest record among KPs with flow rate exceeding 0.1 sccm.

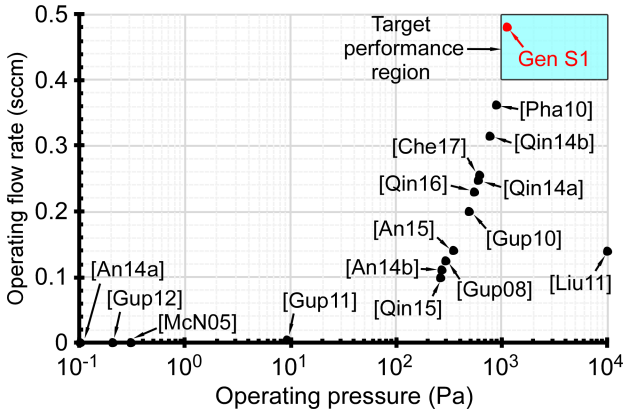

Fig. 6.1: Calculated operating point of the Gen S1 4-stage KP in a μGC system with ≈2.5 kPa/sccm fluidic resistance.

The fabrication of KPs with suspended membrane and ultra-thin pumping channels can be challenging due to the complicated processing steps described in Chapter 1. Furthermore, the stress related fractures and buckling of the membrane can be concerning for suspended KPs. To avoid these challenges and improve the fabrication yield and operation reliability, the suspended membrane was eliminated in the Gen U1 KPs, providing superior mechanical robustness and

reliability. If the epoxy overflows into the pumping channels during the manual assembly step, the unsuspended KP chip can be solvent-cleaned and reassembled. The 4-channel KP of the Gen U1 provides a blocking pressure of 0.6 kPa and a maximum flow rate of 0.04 sccm at an applied power of 2 W. Such blocking pressure per pumping stage, given that the Gen U1 KPs are single-stage, is comparable with that of the Gen S1 and Gen S2 KPs. The maximum flow rate per channel opening area A_{open} is higher than previous generations largely due to the robust pumping channel sidewalls (Table 6.1). Temperature feedback is attained through monolithic thermistors, which could provide a closed-loop operation.

In addition to the mechanical robustness and facile fabrication, the advantages of the Gen U1 KPs also include monolithic integrability. The Gen U1 KPs were monolithically integrated in a fully lab-on-a-chip gas analysis system and provided the suitable gas flows for sampling and separation of volatile organic compounds. Such fully lab-on-a-chip system is the first of its kind and will be reported in an upcoming publication.

A monolithic implementation of high-flow multi-stage and multi-channel KPs is realized in this thesis. The high performance enabled by such implementation can be useful in various applications, especially to achieve commercialization. The monolithic gas analysis system with integrated KPs presented in this thesis is a step towards low-cost, portable commercial μGC that can be implemented in applications such as pharmaceutical, environmental monitoring, and homeland security.

Table 6.1: Benchmarking the performance of the Gen S1, S2, and U1 KPs.

Gen.	Type	Channel length (μm)	ΔT (K)	# of series stages	# of parallel channels	W_p (W)	ΔP (kPa)	Q_{max} (sccm)	Q_{max}/A_{open} (sccm/mm^2)
S1	Suspended	12	84	4	~10^3	1.2	3.30	0.75	13.4
				1	~10^3	0.3	0.83	0.75	
S2A	Suspended	25	36	5	~10^3	0.5	2.00	0.36	5.4
				1	~10^3	0.1	0.50	0.36	
S2B				5	~10^3	0.5	1.45	0.26	3.8
				1	~10^3	0.1	0.29	0.26	
U1	Unsuspended	14	92	1	4	2.0	0.62	0.04	42.7
			94	1	6	3.0	0.57	0.05	32.6
			38	1	45	9.0	0.17	0.04	3.3

6.2. Future Work

6.2.1. Gen S KPs

Various implementations of the suspended KP have been demonstrated to provide high blocking pressure [An13, Gup12, McN05, Qin15] or high flow rate [An14, An15]. The Gen S1 and Gen S2 KPs of this thesis achieved both relatively high flow rate and blocking pressure [Bya21, Bya22]. With tailored pumping channel dimensions and stage arrangement, the suspended KPs could potentially achieve even higher performance. For high pressure generation applications, the pumping channel width needs to increase to maintain the high flow rate as the mean free path of the gas increases. Figure 6.2 shows an estimate of vacuum generation at high flow (Q_{max}>0.4 sccm). The pumping channel width increases from 1 μm up to 100 μm, maintaining a 10× margin with the mean free path. The atmospheric pressure of 101.3 kPa could be pumped down to ≈10 kPa with 120 stages of suspended KPs similar to the Gen S2 KP. With 120 additional pumping stages with 10-100 μm wide pumping channels, an on-chip vacuum can be achieved at high flow. The maximum flow rate of each KP exceeds 0.4 sccm. Such performance can benefit applications such as comprehensive μGCs that require higher blocking pressure or GC-mass spectrometry systems as a roughing pump.

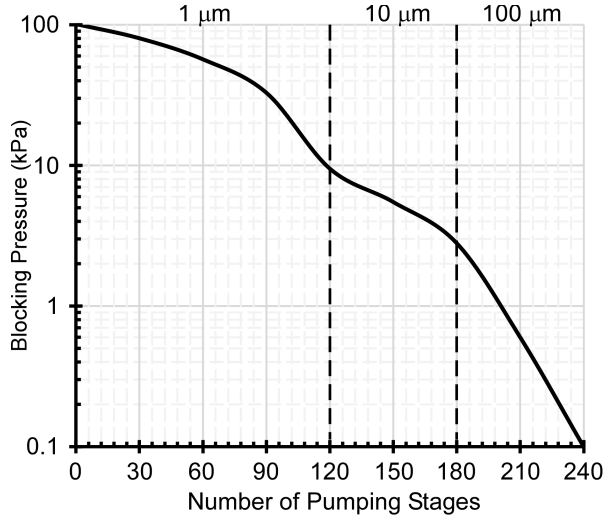

Fig. 6.2: Blocking pressure estimate of a 240-stage suspended KP with 1-100 μm wide pumping channels. Maximum flow rate exceeds 0.4 sccm for each pumping stage.

The fabrication process used in the suspended KP work allows monolithic co-fabrication of flow rate sensors, in addition to the temperature sensors demonstrated in the unsuspended KP work. The flow rate sensors can enable feedback control to provide constant or programed flow rate in varying ambient conditions for applications such as μGC.

6.2.2. Gen U KPs

The performance of the mechanically robust KPs can be improved by altering the pumping channel geometry as necessary for the application and increasing the number of series or parallel channels. For example, wider and deeper pumping channels would provide higher flow rate. Narrower pumping channels would provide higher blocking pressure, although these may be limited by the fabrication process described in Chapter 1. Serially cascaded multiple pumping stages with the use of through-holes and lateral channels have been shown to scale the blocking pressure in the Gen S1 and Gen S2 KPs. The Gen U1 KPs can be cascaded similarly for a higher blocking pressure.

Thermal management should be considered for scaling the number of pumping channels and stages, as observed in the Gen U1 45-channel KP. Some improvement in thermal isolation between the heated region and substrate may be possible with the use of trenches surrounding the heated region, created by the top side DRIE. However, such structure can have lower mechanical robustness and requires FEA evaluation.

The temperature difference along the unsuspended pumping channels was largely in the 2 μm oxide layer, the thickness of which was chosen for its manufacturability. With an implementation of thermally stable non-standard materials with low thermal conductivity, the temperature difference can be further improved for higher performance [Hu00, Ver03, Zha04]. For example, low-*k* dielectric materials such as organic polymers, porous and doped silica, which have been developed for semiconductor manufacturing applications to extend the Moore's law [Tho06], may be used to fabricate the pumping channels.

With improved thermal isolation, cooling (Chapter 5), and other thermal management techniques to reduce and absorb the heat dissipated to the substrate, the pumping channels of the unsuspended KP structure can be more densely arrayed to increase the pumping area and thus the flow rate. The distance between the parallel channels in Fig. 6.3 is determined by the bottom side DRIE pitch, which is 60 μm for the Gen U1 KPs. Compared to the 1.5 mm gap between the parallel pumping channels in the Gen U1 KPs, this design (Fig. 6.3) can reduce the gap to 60 μm and increase the number of parallel pumping channels per area by 25×. Such KP designs with doubly-clamped beam structures need to be evaluated via FEA for mechanical robustness at ambient and operating temperatures.

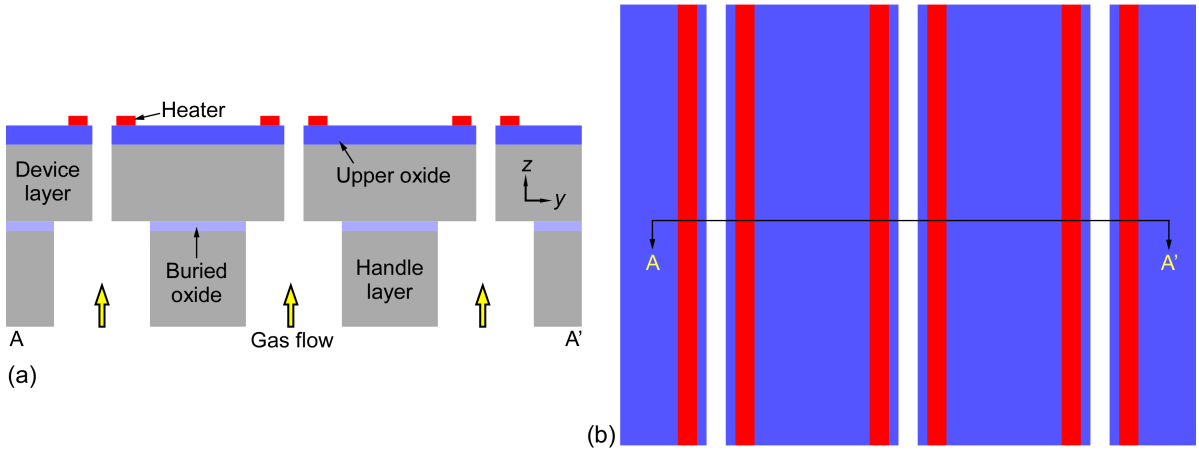

Fig. 6.3: (a) Cross-sectional view, and (b) top view of the KP with unsuspended structure and more densely arranged pumping channels.

The KPs in this thesis can be evaluated with lifetime tests to assess the reliability. Prior KPs with suspended membranes achieved high reliability and long lifetime (>1 year) with up to 30% flow rate decrease from initial value [An13, An15]. The Gen S1 and S2 KPs are anticipated to provide similar level of reliability and performance drift given the utilization of similar suspended membranes and ultra-thin pumping channel sidewalls, whereas the Gen U1 KPs are anticipated to provide higher reliability and less performance drift.

The monolithic KP implementation in the lab-on-a-chip gas analysis system achieved as part of this work could provide low-cost chemical sampling and detection for various applications such as environmental monitoring, homeland security, and forensic analysis [DeW19, DeW20]. For high throughput manufacturing, a glass frit bonding method could be used to attach the SOI and fused silica dies instead of an epoxy for commercial use [Kne05].

References

[An13] S. An, N. K. Gupta, Y. B. Gianchandani, "A Si-micromachined 162-stage two-part Knudsen pump for on-chip vacuum," *Journal of Microelectromechanical Systems*, vol. 23, no. 2, pp. 406-416, 2013.

[An14] S. An, Y. Qin, Y. B. Gianchandani, "A monolithic Knudsen pump with 20 sccm flow rate using through-wafer ONO channels," *IEEE International Conference on Micro Electro Mechanical Systems (MEMS)*, San Francisco, CA, pp. 112-115, 2014.

[An15] S. An, Y. Qin, Y. B. Gianchandani, "A monolithic high-flow Knudsen pump using vertical Al2O3 channels in SOI," *Journal of Microelectromechanical Systems*, vol. 24, no. 5, pp. 1606-1615, 2015.

[Arn91] J. C. Arnold, H. H. Sawin, "Charging of pattern features during plasma etching," *Journal of Applied Physics,* vol. 70, no. 10, pp. 5314-5317, 1991.

[Ast07] A. A. Astle, H. S. Kim, L. P. Bernal, K. Najafi, P. D. Washabaugh, "Theoretical and experimental performance of a high frequency gas micropump," *Sensors and Actuators A: Physical*, vol. 134, no. 1, pp. 245-256, 2007.

[Au11] A. K. Au, H. Lai, B. R. Utela, A. Folch, "Microvalves and micropumps for BioMEMS," *Micromachines*, vol. 2, no. 2, pp. 179-220, 2011.

[Bla20] R. C. Blase, M. J. Libardoni, G. P. Miller, K. E. Miller, C. M. Phillips-Lander, J. H. Waite, C. R. Glein, H. Zhu, A. Ghosh, A. Venkatasubramanian, X. Fan, K. Kurabayashi, "Experimental Coupling of a MEMS Gas Chromatograph and a Mass Spectrometer for Organic Analysis in Space Environments," *ACS Earth and Space Chemistry,* vol. 4, no. 10, pp. 1718-1729, 2020.

[Ben19] A. Benken, "A High-Yield Microfabrication Process for Sapphire Substrate Pressure Sensors with Low Parasitic Capacitances and 200 C Tolerance," Ph.D. dissertation, Dept. Elect. Eng., University of Michigan, Ann Arbor, MI, USA, 2019.

[Bej03] A. Bejan, D. K. Allan, eds. *Heat transfer handbook*. Vol. 1. John Wiley & Sons, 2003.

[Bes12] A. Besharatian, K. Kumar, R. L. Peterson, L. P. Bernal, and K. Najafi, "A scalable, modular, multi-stage, peristaltic, electrostatic gas micro-pump," *IEEE International Conference on Micro Electro Mechanical Systems (MEMS)*, Paris, France, 2012, pp. 1001-1004.

[Blu21] L. M. Blumberg, "Chapter 2 - Theory of gas chromatography," in *Gas chromatography (Second Edition)*, eds. C. F. Poole, Elsevier, pp. 19-97, 2021.

[Bya17] T. Byambadorj, E. Dashtimoghadam, M. Malakoutian, B. Davaji, L. Tayebi, J.E. Richie, C.H. Lee, "On-chip detection of gel transition temperature using a novel micro-thermomechanical method," *PloS one*, vol. 12, no. 8, e0183492, 2017.

[Bya21] T. Byambadorj, Q. Cheng, Y. Qin, Y. B. Gianchandani, "A monolithic Si-micromachined four-stage Knudsen pump for μGC applications," *Journal of Micromechanics and Microengineering*, vol. 31, no. 3, p. 034001, 2021.

[Bya22] T. Byambadorj, Y. Qin, Y. B. Gianchandani, "Blocking Pressure Enhancement in SOI Through-Wafer Monolithic Knudsen Pumps," *IEEE International Conference on Micro Electro Mechanical Systems (MEMS),* Tokyo, Japan, *Accepted*, 2022.

[Car72] G. C. Carle, R. W. Donaldson, S. C. Terry, K. D. Wise, "Microminiature gas chromatograph," In *NASA Tech Briefs*; Ames Research Center: Moffett Field, CA, USA, 1972.

[Che17] Q. Cheng, Y. Qin, Y. B. Gianchandani, "A bidirectional Knudsen pump with superior thermal management for micro-gas chromatography applications," *IEEE International Conference on Micro Electro Mechanical Systems (MEMS)*, Las Vegas, NV, pp. 167-170, 2017.

[Che19] Q. Cheng, "Miniaturized Knudsen Pumps for Micro Gas Chromatography and Other Applications," Ph.D. dissertation, Dept. Mech. Eng., University of Michigan, Ann Arbor, MI, USA, 2019.

[Che20] K. S. Chen, Y. G. Tsai, T. H. Yang, "Stress Analysis and Characterization of PECVD Oxide/Nitride Multi-Layered Films After Thermal Cycling," *IEEE Transactions on Device and Materials Reliability*, vol. 21, no. 1, pp. 17-25, 2020.

[DeW19] K. DeWitt, "Development of technology for low-power gas sensing: IARPA's MAEGLIN program," *Chemical, Biological, Radiological, Nuclear, and Explosives (CBRNE) Sensing XX*, vol. 11010, p. 110100T, 2019.

[DeW20] K. DeWitt, "Advancements in compact gas collection and analysis from IARPA's MAEGLIN program," *Chemical, Biological, Radiological, Nuclear, and Explosives (CBRNE) Sensing XXI*, vol. 11416, p. 114160L, 2020.

[Elb97] L. Elbrecht, U. Storm, R. Catanescu, J. Binder, "Comparison of stress measurement techniques in surface micromachining," *Journal of Micromechanics and Microengineering*, vol. 7, no. 3, p. 151, 1997.

[Fag12] A. Faghri, "Review and advances in heat pipe science and technology," *Journal of heat transfer,* vol. 134, no. 12, pp. 123001-123018, 2012.

[Fai14] A. Faiz, S. McNamara, A. D. Bell, G. Sumanasekera, "Nanoporous Bi2Te3 thermoelectric based Knudsen gas pump," *Journal of Micromechanics and Microengineering*, vol. 24, no. 3, p. 035002, 2014.

[Fu09] Y. Q. Fu, A. Colli, A. Fasoli, J. K. Luo, A. J. Flewitt, A. C. Ferrari, W. I. Milne, "Deep reactive ion etching as a tool for nanostructure fabrication," *Journal of Vacuum Science & Technology B: Microelectronics and Nanometer Structures Processing, Measurement, and Phenomena*, vol. 27, no. 3, pp. 1520-1526, 2009.

[Fuk90] S. Fukui, R. Kaneko, "A database for interpolation of Poiseuille flow rates for high Knudsen number lubrication problems," *Journal of Tribology*, vol. 112, no. 83, pp. 78-83, 1990.

[Gar15] A. Garg, M. Akbar, E. Vejerano, S. Narayanan, L. Nazhandali, L. C. Marr, M. Agah, "Zebra GC: A mini gas chromatography system for trace-level determination of hazardous air pollutants," *Sensors and Actuators B: Chemical*, vol. 212, pp. 145-154, 2015.

[Guc85] H. Guckel, T. Randazzo, D.W. Burns, "A simple technique for the determination of mechanical strain in thin films with applications to polysilicon," *Journal of Applied Physics,* vol. 57, no. 5, pp. 1671-1675, 1985.

[Guc92] H. Guckel, D.W. Burns, C. Rutigliano, E. Lovell, B. Choi, "Diagnostic microstructures for the measurement of intrinsic strain in thin films," *Journal of Micromechanics and Microengineering,* vol. 2, no. 2, p. 86, 1992.

[Gup08] N. K. Gupta, Y. B. Gianchandani, "Thermal Transpiration in Zeolites: A Mechanism for Motionless Gas Pumps," *Applied Physics Letters*, vol. 93, no. 19, pp. 193511-1–193511-3, 2008.

[Gup11a] N. K. Gupta, Y. B. Gianchandani, "Porous ceramics for multistage Knudsen micropumps—Modeling approach and experimental evaluation," *Journal of Micromechanics and Microengineering*, vol. 21, no. 9, pp. 1–14, 2011.

[Gup11b] N. K. Gupta, Y. B. Gianchandani, "Thermal transpiration in mixed cellulose ester membranes: enabling miniature, motionless gas pumps," *Microporous Mesoporous Mater.*, vol. 142, no. 2–3, pp. 535–541, 2011.

[Gup12] N. K. Gupta, S. An, Y. B. Gianchandani, "A Si-micromachined 48-stage Knudsen pump for on-chip vacuum," *Journal of Micromechanics and Microengineering*, vol. 22, no. 10, pp. 1–8, 2012.

[Hu00] C. Hu, M. Morgen, P. S. Ho, A. Jain, W. N. Gill, J. L. Plawsky, P. C. Wayner Jr, "Thermal conductivity study of porous low-k dielectric materials," *Applied Physics Letters*, vol. 77, no. 1, pp. 145-147, 2000.

[Hwa97] G.S. Hwang, K.P. Giapis, "On the origin of the notching effect during etching in uniform high density plasmas," *Journal of Vacuum Science & Technology B: Microelectronics*

and Nanometer Structures Processing, Measurement, and Phenomena, vol. 15, no. 1, pp. 70-87, 1997.

[Her82] S.D. Hersee, J.P. Duchemin, "Low-pressure chemical vapor deposition," *Annual Review of Materials Science,* vol. 12, no. 1, pp. 65-80, 1982.

[Ino19] N. Inomata, K. Kamakura, N. V. Toan, T. Ono, "Fabrication of on-chip vacuum pump using a silicon nanostructure by metal-assisted chemical etching," *IEEJ Transactions on Electrical and Electronic Engineering*, vol. 14, no. 6, pp. 954-958, 2019.

[Ish99] K. Ishihara, C.F. Yung, A.A. Ayón, M.A. Schmidt, "Inertial sensor technology using DRIE and wafer bonding with connecting capability," *Journal of Microelectromechanical Systems*, vol. 8, no. 4, pp. 403-408, 1999.

[Kim07a] H. Kim, W. H. Steinecker, S. Reidy, G. R. Lambertus, A. A. Astle, K. Najafi, E. T. Zellers, L. P. Bernal, P. D. Washabaugh, K. D. Wise, "A micropump-driven high-speed MEMS gas chromatography system," *IEEE International Conference on Solid-State Sensors, Actuators and Microsystems (Transducers)*, Lyon, France, pp. 1505-1508, 2007.

[Kim07b] H. Kim, A. A. Astle, K. Najafi, L. P. Bernal, P. D. Washabaugh, "A fully integrated high-efficiency peristaltic 18-stage gas micropump with active microvalves," *IEEE International Conference on Micro Electro Mechanical Systems (MEMS)*, Hyogo, Japan, pp. 127-130, 2007.

[Kim11] S. K. Kim, H. Chang, E. T. Zellers, "Microfabricated gas chromatograph for the selective determination of trichloroethylene vapor at sub-parts-per-billion concentrations in complex mixtures, " *Analytical Chemistry*, vol. 83, no.18, pp. 7198–7206, 2011.

[Kne05] R. Knechtel, "Glass frit bonding: an universal technology for wafer level encapsulation and packaging," *Microsystem Technologies*, vol. 12, no. 1-2, pp. 63-68, 2005.

[Knu09] M. Knudsen, "Eine revision der gleichgewichtsbedingung der gase. Thermische molekularströmung," *Annalen der Physik*, vol. 336, no. 1, pp. 205-229, 1909.

[Knu10] M. Knudsen, "Thermischer molekulardruck der gase in röhren," *Annalen der Physik*, vol. 338, no. 16, pp. 1435-1448, 1910.

[Knu35] M. Knudsen, J. R. Partington, "The kinetic theory of Gases. Some Modern Aspects," *The Journal of Physical Chemistry*, vol. 39, no. 2, pp. 307-307, 1935.

[Las04] D. J. Laser, J. G. Santiago, "A review of micropumps," *Journal of micromechanics and microengineering*, vol. 14, no. 6, pp. 35-64, 2004.

[Liu11] J. Liu, N. K. Gupta, K. D. Wise, Y. B. Gianchandani, X. Fan, "Demonstration of motionless Knudsen pump based micro-gas chromatography featuring micro-fabricated columns and on-column detectors," *Lab on a Chip*, vol. 11, no. 20, pp. 3487-3492, 2011.

[Lia21] W. Liao, X. Zhao, H.T. Lu, T. Byambadorj, Y. Qin, Y.B. Gianchandani, "Progressive Cellular Architecture in Microscale Gas Chromatography for Broad Chemical Analyses," *Sensors*, vol. 21, no. 9, p. 3089, 2021.

[Luc87] G. Lucovsky, D.V. Tsu, "Plasma enhanced chemical vapor deposition: Differences between direct and remote plasma excitation," *Journal of Vacuum Science & Technology A: Vacuum, Surfaces, and Films,* vol. 5, no. 4, pp. 2231-2238, 1987.

[Man93] C. Manfredotti, F. Fizzotti, M. Boero, P. Pastorino, E. Vittone, V. Rigato, "Investigation on microvoids in PECVD a-Si:H," *MRS Online Proceedings Library*, p. 297, 1993.

[McI87] E.J. McInerney, S.C. Avanzino, "A planarized SiO2 interlayer dielectric with bias-CVD," *IEEE transactions on electron devices,* vol. 34, no. 3, pp. 615-620, 1987.

[McN05] S. McNamara, Y. B. Gianchandani, "On-chip vacuum generated by a micromachined Knudsen pump," *Journal of Micromechanics and Microengineering*, vol. 14, no. 4, pp. 741-746, 2005.

[McN19] H. M. McNair, J. M. Miller, N. H. Snow, "Basic gas chromatography," *John Wiley & Sons, 2019*.

[Mei67] P. Meijers, "Doubly-Periodic Stress Distributions in Perforated Plates," Ph.D. dissertation, Delft University of Technology, Delft, Netherlands, 1967.

[Mir98] S.R. Mirmira, L.S. Fletcher, "Review of the thermal conductivity of thin films," *Journal of Thermophysics and Heat Transfer*, vol. 12, no. 2, pp. 121-131, 1998.

[Nak95] K. Nakamura, T. Takahashi, T. Hikichi, I. Takata, "An observation of breakdown characteristics on thick silicon oxide," *Proceedings of International Symposium on Power Semiconductor Devices and IC's: ISPSD'95*, pp. 374-379, 1995.

[Nak16] S. Nakaye, H. Sugimoto, "Demonstration of a gas separator composed of Knudsen pumps," *Vacuum*, vol. 125, pp. 154-164, 2016.

[Ngu02] N. T. Nguyen, H. Xiaoyang, T. K. Chuan, "MEMS-micropumps: a review," *Journal of fluids Engineering*, vol. 124, no. 2, pp. 384-392, 2002.

[Noz95] T. Nozawa, T. Kinoshita, T. Nishizuka, A. Narai, T. Inoue, A. Nakaue, "The electron charging effects of plasma on notch profile defects," *Japanese Journal of Applied Physics*, vol. 34, no. 4S, p. 2107, 1995.

[Pet00] P. Petrik, T. Lohner, M. Fried, L.P. Biró, N.Q. Khanh, J. Gyulai, W. Lehnert, C. Schneider, H. Ryssel, "Ellipsometric study of polycrystalline silicon films prepared by low-pressure chemical vapor deposition," *Journal of Applied Physics,* vol. 87, no. 4, pp. 1734-1742, 2000.

[Pha10] K. Pharas, S. McNamara, "Knudsen pump driven by a thermoelectric material," *Journal of Micromechanics and Microengineering*, vol. 20, no. 12, pp. 125032-1–125032-7, 2010.

[Pi16] C.H. Pi, K.T. Turner, "Design, analysis, and characterization of stress-engineered 3D microstructures comprised of PECVD silicon oxide and nitride," *Journal of Micromechanics and Microengineering,* vol. 26, no. 6, p. 065010, 2016.

[Pli65] W.A. Pliskin, H.S. Lehman, "Structural evaluation of silicon oxide films," *Journal of the Electrochemical Society,* vol. 112, no. 10, p. 1013, 1965.

[Pri16] P. J. Pritchard, W. M. John, C. L. John, *Fox and McDonald's Introduction to Fluid Mechanics, 9th Version*, John Wiley & Sons, 2016.

[Qia10] L. Qian, J. Wang, Z. Yang, G. Yan, "Fabrication of ultra-deep high-aspect-ratio isolation trench without void and its application," *IEEE International Conference on Nano/Micro Engineered and Molecular Systems (NEMS)*, Xiamen, China, pp. 654-657, 2010.

[Qin14a] Y. Qin, Y. B. Gianchandani, "iGC1: An integrated fluidic system for as chromatography including Knudsen pump, preconcentrator, column, and detector microfabricated by a three-mask process," *Journal of Microelectromechanical Systems*, vol. 23, no. 4, pp. 980-990, 2014.

[Qin14b] Y. Qin, Y. B. Gianchandani, "iGC2: an architecture for micro gas chromatographs utilizing integrated bi-directional pumps and multi-stage preconcentrators," *Journal of Micromechanics and Microengineering*, vol. 24, no. 6, pp. 065011-1–065011-10, 2014.

[Qin15] Y. Qin, S. An, Y. B. Gianchandani, "Arrayed architectures for multi-stage Si-micromachined high-flow Knudsen pumps," *Journal of Micromechanics and Microengineering*, vol. 25, no. 11, pp. 115026, 2015.

[Qin16] Y. Qin, Y. B. Gianchandani, "A fully electronic microfabricated gas chromatograph with complementary capacitive detectors for indoor pollutants," *Microsystems & Nanoengineering*, vol. 2, pp. 15049, 2016.

[Rey79] O. Reynolds, "On certain dimensional properties of matter in the gaseous state," *Philos. Trans. Roy. Soc. London*, vol. 170, no. 1879, pp. 727–845, 1879.

[Sai12] M.J. Sailor, "Porous silicon in practice: preparation, characterization and applications," *John Wiley & Sons*, 2012.

[San02] F. J. Santos, M. T. Galceran, "The application of gas chromatography to environmental analysis," *Trends Anal. Chem.*, vol. 21, no. 9–10, pp. 672–685, 2002.

[Sha99] F. Sharipov, "Non-isothermal gas flow through rectangular microchannels," *Journal of Micromechanics and Microengineering*, vol. 9, no. 4, pp. 394-401, 1999.

[Shi14] C. Shin, J. Park, J. Jung, S. Bong, S. Kim, Y.J. Lee, Junsin Yi. "Control of micro void fraction and optical band gap in intrinsic amorphous silicon thin films (VHF-PECVD) for thin film solar cell application," *Materials Research Bulletin*, vol. 60, pp. 895-899, 2014.

[Ste93] E. Stemme, G. Stemme, "A valveless diffuser/nozzle-based fluid pump," *Sensors and Actuators A: physical*, vol. 39, no. 2, pp. 159-167, 1993.

[Tan16] Y. Tang, K. Najafi, "High aspect-ratio low-noise multi-axis accelerometers made from thick silicon," *Proceedings of IEEE 3rd International Symposium on Inertial Sensors and Systems*, Laguna Beach, CA, USA, Feb. 2016, pp. 121-124.

[Tan17] Y. Tang, A. Sandoughsaz, K. Najafi, "Ultra high aspect-ratio and thick deep silicon etching (UDRIE)," *Proceedings of IEEE 30th International Conference of Micro Electro Mechanical Systems (MEMS)*, Las Vegas, NV, USA, Jan. 2017, pp. 700-703.

[Tan18] Y. Tang, A. Sandoughsaz, K. J. Owen, K. Najafi, "Ultra deep reactive ion etching of high aspect-ratio and thick silicon using a ramped-parameter process," *Journal of Microelectromechanical Systems*, vol. 27, no. 4, pp. 686-697, 2018

[Ter79] S.C. Terry, J.H. Jerman, J.B. Angell, "A gas chromatographic air analyzer fabricated on a silicon wafer," *IEEE Trans. Electron Devices,* vol. 26, no. 12, pp. 1880–1886, 1979.

[Tho06] S. E. Thompson, S. Parthasarathy, "Moore's law: the future of Si microelectronics," *Materials today,* vol. 9, no. 6, pp. 20-25, 2006.

[Toa18] N. V. Toan, N. Inomata, N. H. Trung, T. Ono, "Knudsen pump produced via silicon deep RIE, thermal oxidation, and anodic bonding processes for on-chip vacuum pumping," *Journal of Micromechanics and Microengineering,* vol. 28, no. 5, p. 055001, 2018.

[Ver03] J. Veres, S. D. Ogier, S. W. Leeming, D. C. Cupertino, S. M. Khaffaf, "Low-k insulators as the choice of dielectrics in organic field-effect transistors," *Advanced Functional Materials*, vol. *13, no.* 3, pp. 199-204, 2003.

[Wag96] B. Wagner, H.J. Quenzer, S. Hoerschelmann, T. Lisec, M. Juerss, "Bistable microvalve with pneumatically coupled membranes," *Proceedings of Ninth International Workshop on Micro Electromechanical Systems*, pp. 384-388. IEEE, 1996.

[Wan06] C. M. Wang, Y. Y. Zhang, S. S. Ramesh, S. Kitipornchai, "Buckling analysis of micro-and nano-rods/tubes based on nonlocal Timoshenko beam theory," *Journal of Physics D: Applied Physics*, vol. 39, no. 17, pp. 3904, 2006

[Wan16] Q. Wang, W. Hong, L. Dong, "Graphene “microdrums” on a freestanding perforated thin membrane for high sensitivity MEMS pressure sensors," *Nanoscale,* vol. 8, no. 14, pp. 7663-7671, 2016.

[Wil02] C. G. Wilson, Y. B. Gianchandani, "Spectral detection of metal contaminants in water using an on-chip microglow discharge," *IEEE Transactions on Electron Devices*, vol. 49, no. 12, pp. 2317-2322, 2002.

[Woi05] P. Woias, "Micropumps—past, progress and future prospects," *Sensors and Actuators B: Chemical*, vol. 105. no. 1, pp. 28-38, 2005.

[Wu10] B. Wu, A. Kumar, and S. Pamarthy, "High aspect ratio silicon etch: A review," *Journal of Applied Physics*, vol. 108, no. 5, p. 051101, Nov. 2010.

[Xie15] J. Xie, "Fabrication challenges and test structures for high-aspect-ratio SOI MEMS devices with refilled electrical isolation trenches," *Microsystem Technologies,* vol. 21, no. 8, pp. 1719-1727, 2015.

[Xu05] T. B. Xu, S. Ji, "Development, characterization, and theoretical evaluation of electroactive polymer-based micropump diaphragm," *Sensors and Actuators A: Physical*, vol. 121, no. 1, pp. 267-274, 2005.

[Yee13] S. Y. Yee, R. L. Peterson, L. P. Bernal, K. Najafi, "Highly reliable electrostatic actuator using filleted electrode made with photoresist solvent reflow," *IEEE International Conference on Solid-State Sensors, Actuators and Microsystems (Transducers)*, Barcelona, Spain, pp. 1617–1620, 2013.

[You03] M. Young, Y.L. Han, E. P. Muntz, G. Shiflett, A. Ketsdever, A. Green, "Thermal transpiration in microsphere membranes," *American Institute of Physics Conference Proceedings*, vol. 663, no. 1, pp. 743-751, 2003.

[Zel04] E.T. Zellers, W.H. Steinecker, G.R. Lambertus, M. Agah, C.-J. Lu, H.K.L. Chan, J.A. Potkay, M.C. Oborny, J.M. Nichols, A. Astle, H.S. Kim, M.P. Rowe, J. Kim, L.W. da Silva, J. Zheng, J.J. Whiting, R.D. Sacks, S.W. Pang, M. Kaviany, P.L. Bergstrom, A.J. Matzger, Ç. Kurdak, L.P. Bernal, K. Najafi, and K.D. Wise, "A Versatile MEMS Gas Chromatograph for Determination of Environmental Vapor Mixture," *Technical Digest, Solid State Sensor, Actuator and Microsystems Workshop (Hilton Head 2004)*, pp. 61-66, 2004.

[Zha04] X. Zhang, H. Lu, A.M. Soutar, X. Zeng, "Thick UV-patternable hybrid sol-gel films prepared by spin coating," *Journal of Materials Chemistry*, vol. 14, no. 3, pp. 357-361, 2004.

[Zho16] M. Zhou, J. Lee, H. Zhu, R. Nidetz, K. Kurabayashi, X. Fan, "A fully automated portable gas chromatography system for sensitive and rapid quantification of volatile organic compounds in water," *RSC Advances*, vol. 6, no. 55, pp. 49416-49424, 2016.

[Zhu05] Y. Zhu, G. Yan, J. Fan, J. Zhou, X. Liu, Z. Li, Y. Wang, "Fabrication of keyhole-free ultra-deep high-aspect-ratio isolation trench and its applications," *Journal of Micromechanics and Microengineering*, vol. 15, no. 3, p. 636, 2005.

[Zie98] V. Ziebart, O. Paul, U. Munch, J. Schwizer, H. Baltes, "Mechanical properties of thin films from the load deflection of long clamped plates," *Journal of Microelectromechanical Systems*, vol. 7, no. 3, pp. 320-328, 1998